

Analysis and modelling of respiratory metabolism in *Neisseria meningitidis*

Andrew Schofield

Submitted for the degree of Doctor of Philosophy

The University of York

Department of Biology

April 2012

Abstract

N. meningitidis is capable of respiration in both aerobic and microaerobic environments by reduction of oxygen and nitrite respectively. The respiratory chain and genetic regulation of this system are already well understood, but there are complex interactions between components which make predicting which respiratory path will be used difficult. To predict the respiratory behaviour of *N. meningitidis* I have built a mathematical model using a novel combination of experiments and Bayesian fitting.

Contents

1	Introduction	10
1.1	Biology of <i>Neisseria meningitidis</i>	10
1.2	Pathogenicity of <i>N. meningitidis</i>	11
1.3	Growth of <i>N. meningitidis</i>	13
1.4	Organisation of the Respiratory Chain of <i>N. meningitidis</i>	13
1.5	Respiratory Enzymes in <i>N. meningitidis</i>	18
1.5.1	Cytochrome <i>cbb</i> ₃ oxidase	18
1.5.2	NorB Nitric Oxide Reductase	21
1.5.3	AniA Nitrite Reductase	21
1.6	Respiratory Electron Transporters in <i>N. meningitidis</i>	22
1.6.1	NADH Dehydrogenase	22
1.6.2	Cytochrome <i>bc</i> ₁ Complex	23
1.6.3	Cytochromes <i>c</i> ₄ , <i>c</i> _x and <i>c</i> ₅	25
1.6.4	Quinone Pool	25
1.7	Respiration Regulatory Proteins in <i>N. meningitidis</i>	26
1.7.1	NsrR - Nitrite Sensing Repressor Protein	26
1.7.2	FNR - Fumarate and Nitrate Reductase Regulator	27
1.7.3	NarQ/NarP - Nitrite Response Sensor/Regulator	27
1.8	Organisation of Respiratory Chains in Other Bacteria	28
1.8.1	The Respiratory Chain of <i>Paracoccus denitrificans</i>	28
1.8.2	The Respiratory Chain of <i>Escherichia coli</i>	29
1.9	Systems Biology	31
1.10	Modelling	34
1.10.1	Modelling Respiratory Systems	34
1.10.2	Modelling Tools	36
1.11	Aims	36
2	Materials and Methods	38
2.1	<i>Neisseria meningitidis</i> Strains Used in This Work	38
2.2	Culturing <i>Neisseria meningitidis</i>	39
2.2.1	Growth of <i>Neisseria meningitidis</i>	39
2.2.2	Preparation of Antibiotic Selective Media	39
2.2.3	Preparation of Frozen Bacterial Stocks	39
2.2.4	Streaking Plates for OD to CFU Ratio Calculation	40
2.3	Measuring Oxygen Concentration	40
2.3.1	Calibration of Oxygen Electrode	40
2.4	Measuring Nitric Oxide Concentration	41
2.4.1	Calibration of Nitric Oxide Electrode	42

2.5	Measuring Nitrite Concentration (Griess Assay)	43
2.6	Nitric Oxide Production	43
3	Model - Construction and Parameters	46
3.1	Construction	46
3.1.1	Normalising the Data	47
3.1.2	Converting Biological Reactions into Differential Equations	47
3.1.2.1	Respiratory Substrates	47
3.1.2.2	Electron Transporters	51
3.1.2.3	Terminal Reductases	53
3.1.3	Assumptions and their Justifications	55
3.2	Parameters and their Prior Distributions	56
3.3	Solving Ordinary Differential Equations	61
3.4	Implementation of the Model in Software	62
3.5	Parameter Estimation	62
4	Parameter Estimation Methodologies	64
4.1	Simulated Annealing	65
4.2	Approximate Bayesian Computation by Sequential Monte Carlo . .	69
4.3	Metropolis Hastings Monte Carlo	73
4.4	Implementation	74
4.5	Integrative Scheme	76
5	Oxygen Reduction in <i>N. meningitidis</i>	78
5.1	Aerobic Reduction of Oxygen	78
5.1.1	Introduction	78
5.1.2	Experimental Results	79
5.1.2.1	Generation of Prior Probability Distributions	81
5.1.2.2	Initial Parameter Estimation Results	85
5.1.2.3	Secondary Prior Probability Distributions	91
5.1.2.4	Secondary Parameter Estimation Results	92
5.1.2.5	Analysis of Convergence	99
5.1.2.6	Analysis of Correlation	99
5.1.3	Discussion	103
6	Nitric Oxide Reduction in <i>N. meningitidis</i>	105
6.1	Aerobic Nitric Oxide Reduction	105
6.1.1	Introduction	105
6.1.2	Experimental Results	107
6.1.2.1	Prior Probability Distributions	110
6.1.2.2	Parameter Estimation Results	110
6.1.2.3	Analysis of Convergence	113
6.1.2.4	Analysis of Correlation	113
6.1.3	Discussion	113
6.2	Microaerobic Nitric Oxide Reduction	113
6.2.1	Introduction	113
6.2.2	Results	113
6.2.3	Discussion	113
6.3	Aerobic Nitric Oxide Reduction in <i>nsrR</i> ⁻ mutant	113

6.3.1	Introduction	113
6.3.2	Results	113
6.3.3	Discussion	113
7	Nitrite Reduction in <i>N. meningitidis</i>	114
7.1	Microerobic Nitrite Reduction	114
7.1.1	Introduction	114
7.1.2	Results	114
7.1.3	Discussion	114
7.2	Microaerobic Nitrite Reduction in <i>norB</i> ⁻ mutant	114
7.2.1	Introduction	114
7.2.2	Results	114
7.2.3	Discussion	114
7.3	Aerobic Nitrite Reduction in <i>nsrR</i> ⁻ mutant	114
7.3.1	Introduction	114
7.3.2	Results	116
7.3.3	Discussion	116
7.4	Aerobic Nitrite Reduction in <i>nsrR</i> ⁻ - <i>norB</i> ⁻ mutant	116
7.4.1	Introduction	116
7.4.2	Results	116
7.4.3	Discussion	116
8	AniA and NorB Expression in <i>N. meningitidis</i>	117
8.1	Aerobic and Microaerobic Expression	117
8.1.1	Introduction	117
8.1.2	Results	117
8.1.3	Discussion	117
9	The Completed Model	118
9.1	Amalgamation of cytochromes	118
A	Appendix	119
A.1	Adaptive step sizes and numerical instability	119
A.2	Affinity of <i>cbb</i> ₃ for Oxygen	119
List of Abbreviations		122
References		123

List of Figures

1.1	Complete denitrification.	14
1.2	Layout of the components of the respiratory system in <i>Neisseria meningitidis</i> .	16
1.3	Regulation of respiratory components in <i>Neisseria meningitidis</i> .	18
1.4	The <i>cbb₃</i> oxidase.	19
1.5	3D Structure of <i>cbb₃</i> oxidase.	20
1.6	The modified Q-cycle used by the bacterial <i>bc₁</i> complex.	24
1.7	Structure of the ubiquinone molecule.	26
1.8	Branched electron transport chains of <i>N. meningitidis</i> .	29
1.9	Branched electron transport chains of <i>Paracoccus</i> species.	30
1.10	Branched electron transport chains of <i>E. coli</i> .	31
1.11	Systems biology cycle.	33
1.12	System complexity.	33
2.1	Exploded view of the oxygen electrode	41
2.2	Oxygen electrode chamber with nitric oxide probe inserted	42
2.3	NO making apparatus.	44
3.1	Oxygen Diffusion Rates	60
4.1	Pseudo-code showing how the simplest annealing algorithm works.	66
4.2	Example simulated annealing temperature schedule	67
4.3	Schematic diagram showing the technique used to generate a spread of parameters using a synthetic chromosome.	68
4.4	Simulation results of the Lotka-Volterra validation run.	75
4.5	MHMC results of the Lotka-Volterra validation run.	75
5.1	Oxygen reducing electron transport chain of <i>N. meningitidis</i>	79
5.2	Highly repeatable oxygen reduction	80
5.3	Aerating oxygen reducing cultures with significant delay	81
5.4	Oxygen Reduction in <i>Neisseria meningitidis</i> .	82
5.5	Prior probability distributions for oxygen reduction	84
5.6	Oxygen Reduction in <i>Neisseria meningitidis</i> .	86
5.7	Simulation BOF improves as parameter estimation progresses	87
5.8	Individual parameter trajectories for multiple runs on the same experimental dataset	89
5.9	Posterior probability distributions for oxygen reduction	90
5.10	Prior probability distributions for oxygen reduction	93
5.11	Oversampled Posterior Distributions	95

5.12 Posterior probability distributions for oxygen reduction	96
5.13 Oxygen Reduction in <i>Neisseria meningitidis</i>	98
6.1 Nitric oxide reducing electron transport chain of <i>N. meningitidis</i> . .	106
6.2 Nitric Oxide Reduction in <i>Neisseria meningitidis</i>	108
6.3 Nitric Oxide Reduction in <i>Neisseria meningitidis</i>	108
6.4 Nitric Oxide Reduction in <i>Neisseria meningitidis</i>	109
6.5 Prior probability distributions for aerobic nitric oxide reduction . .	111
6.6 Nitric Oxide Reduction in <i>Neisseria meningitidis</i>	112
7.1 Nitrite reducing electron transport chain of <i>N. meningitidis</i>	115
7.2 Nitrite Reduction in <i>Neisseria meningitidis</i>	116
A.1 Lineweaver-Burk Plot for Oxygen Reduction in <i>Neisseria meningitidis</i> .	119

List of Tables

1.1	The reductions catalysed by the respiratory enzymes in <i>N. meningitidis</i>	15
2.1	Bacterial strains and sources	38
2.2	Final antibiotic concentrations	39
2.3	Sodium Nitrite concentrations used to calibrate ISO-NOP Nitric Oxide sensor.	43
2.4	Chemicals needed for preparation of Nitric Oxide solution.	45
3.1	Model parameters	57
5.1	First Prior Probability Table	83
5.2	Second Prior Probability Table	92
5.3	Posterior Probability Statistics	97
5.4	Gelman-Rubin Convergence Statistic	100
5.5	Regression Analysis of Oxygen Reduction Parameters	101
5.6	Regression Analysis of Oxygen Reduction Parameters	102
A.1	Model Variables	120
A.2	Model Parameters	121

Acknowledgements

Chapter 1

Introduction

1.1 Biology of *Neisseria meningitidis*

Neisseria meningitidis is a Gram-negative, bean-shaped diplococcal bacterium¹, surrounded by a lipid membrane containing outer membrane proteins and lipopolysaccharides¹. When pathogenic, the bacteria also has a polysaccharide capsule attached to the membrane¹. It is non-spore forming, non-motile but pilated, and lives as an obligate human pathogen (humans being its only host)². *N. meningitidis* inhabits the mucosal membranes primarily in the respiratory tract, and it is estimated that up to 20-25% of the population have this bacteria in their nasopharynx while being asymptomatic²⁻⁴.

The *Neisseria* genus contains a number of non-pathogenic species which are part of the normal human flora including *N. subflava*, *N. flavescens*, *N. lactamica* and *N. sicca*⁵. Two species of *Neisseria* are the causative agents of human diseases, *N. meningitidis*, which causes bacterial meningitis and *N. gonorrhoea* which causes gonorrhoea. Being β -proteobacteria², the *Neisseria* genus is also related to a number of other pathogenic bacteria including *Bordetella*, *Burkholderia* and *Spirillum*. This taxa also includes ammonia-oxidising bacteria such as *Nitrosomonas*⁶.

N. meningitidis is classified into 13 different serogroups based on the differences in lipopolysaccharides, capsules, outer membrane proteins and adhesion molecules^{1,2,7}. 3 of these 13 serogroups are the main cause of meningococcal

meningitis, with serogroups B and C being the most prevalent¹. Vaccines for serogroup C are available, but serogroup B currently has no effective vaccine, as it mimics human antigens² and it is a poor immunogen⁸. In addition to being the causative agent for meningococcal meningitis, *N. meningitidis* also causes septicaemia and the combination has a mortality rate of 10% even with therapy^{1,2}.

N. meningitidis is dependent on a source of iron, and must source this from its environment⁹. It does this by directly capturing iron from the host via human transferrins^{9–11} and lactoferrin⁹. This capture is brought about by membrane surface receptors that can bind the transferrins which then go on to internalise the iron into the bacterium for growth¹².

1.2 Pathogenicity of *N. meningitidis*

Meningitis is caused by *N. meningitidis* entering the bloodstream and travelling to the meninges, a set of membranes that envelope the central nervous system, where the bacteria goes on to cause inflammation. Once it has entered the bloodstream, *N. meningitidis* is capable of switching its capsule by phase-variation to avoid host-immune detection^{13,14}. After colonisation by the bacterium, in order to enter the bloodstream, it must first adhere to the mucosal tissue. This is facilitated by adhesion molecules on the outer membrane and by pili, with the latter being the primary source of adhesion^{1,7}. Once the bacteria are adhered to the mucosal cells, additional contacts are made with the outer membrane proteins. Interestingly, the presence of the polysaccharide capsule, which is required for survival in the bloodstream, interferes with these additional contacts². *N. meningitidis* invades the bloodstream by being endocytosed by the mucosal epithelial cells, a process which is triggered by the pili and outer membrane proteins on the bacteria.

N. meningitidis is able to survive in the bloodstream (typically an antimicrobial environment) mainly by virtue of its polysaccharide capsule as this is able to protect the bacteria against various immune responses by the host including

complement-mediated bacteriolysis and phagocytosis by neutrophils¹. Despite these protective features, specific antibodies *do* provide full protection against the bacteria, but the time taken for these antibodies to be produced means that the host has a period of at least 1 week in which it must rely on innate immune response¹. Evidence suggests that systemic infection by *N. meningitidis* can only occur in hosts which are immunocompromised in some way, specifically if they do not have the serum bactericidal antibodies against capsular or non-capsular antigens, or they are missing certain complement components⁴. A number of factors can increase the likelihood of contracting bacterial meningitis including smoking and travelling to epidemic regions². In developed countries, the highest rates of invasive meningococcal meningitis are seen in infants and children less than 4 years-old, adolescents, military recruits and groups where crowding and new exposures occur such as college students living in dormitories, however the disease is capable of affecting all age groups².

There is evidence to suggest that much of the damage done to the host during a meningococcal infection is actually caused by the host in an attempt to rid itself of the bacteria¹⁵. A systemic infection causes a massive inflammatory response and the resulting quantities of cytokines produced eventually lead to organ dysfunction and the proteases produced by neutrophil activation also lead to endothelial injury¹⁵.

Once *N. meningitidis* has entered the bloodstream, it goes on to invade the cerebro-spinal fluid (CSF), which serves as an excellent culture medium for the bacteria⁴. The host response to this infection is inflammation of the meninges, the membranes surrounding the central nervous system. This leads to a build-up of serous fluid in the brain causing cerebral swelling. Once the bacteria have entered the CSF, antimicrobial treatment is required otherwise the effects are almost invariably fatal⁴.

Initially a meningococcal infection presents as a slight fever and chills, which may improve after 4-6 hours. Haemorrhagic skin lesions may appear between

8 and 18 hours, however roughly 20% of sufferers never present with lesions. These skin lesions are possibly the most well known symptom of bacterial meningitis as they are characterised by a non-blanching (does not turn white under mild pressure) rash. The clearest evidence for meningococcal infection is a fever, stiff neck, aversion to bright light, vomiting, skin lesions and headaches. Unfortunately not all these symptoms may be present in all cases⁴.

When meningococcal septicaemia occurs, renal function may be impaired as a direct consequence of cardiac impairment. Septicaemia causes “capillary leak” which reduces cardiac output and increases the effort required to breathe normally. Reduced cardiac output can also affect the gastrointestinal tract leading to reduced function. Once treated these symptoms will usually subside as cardiac output improves¹⁵.

In most cases the treatment for meningococcal meningitis is with antibiotics, where the primary aim is to achieve a rapid bactericidal effect in the CSF¹. This treatment is suggested prior to positive identification of cultures of the bacteria obtained from the CSF as any delay is potentially life-threatening if the bacteria have indeed invaded the CSF⁴.

1.3 Growth of *N. meningitidis*

Bacteria require carbon and energy sources in order to grow, and these are often sourced from sugars present in the environment. *N. meningitidis* can only use the sugars glucose and maltose as carbon sources^{16,17}, however they can use peptides as carbon sources. The bacteria are usually grown on Müller-Hinton broth and Columbia agar which are peptide-based formulations.

1.4 Organisation of the Respiratory Chain of *N. meningitidis*

N. meningitidis is classified as an aerobe and as such has an oxidase pathway for reducing oxygen (O_2), but given that the environment in the nasopharynx is poor in oxygen, the bacteria must also be capable of respiring in a microaerobic



Figure 1.1: **Complete denitrification.** The process of reducing nitrite to nitrogen gas. In *N. meningitidis* the first and final steps highlighted in blue do not occur.

environment. This is evidenced by the fact that bacterial isolates from the na-sopharynx routinely contain both strict aerobes and strict anaerobes¹⁸. Genomic analysis of 2 strains of *N. meningitidis* shows that there are 3 terminal oxidases; 1 of each for reducing oxygen, nitrite (NO_2^-) and nitric oxide (NO)¹⁹. This analysis may be expanded as there are now many more genomes published. Experiments showed that under oxygen limiting conditions, *N. meningitidis* was capable of growth when nitrite was present in the media (Müller-Hinton Broth), and that nitrate (NO_3^-), the probable source for nitrite, had no effect on growth¹⁹. Additionally the bacteria require carbon dioxide, as shown by Tuttle and Scherp²⁰ and have 2 enzymes which catalyse the reduction of CO_2^4 .

In vivo, nitrite is obtained as a product of digesting nitrate in food. There are a number of facultative nitrate-reducing bacteria present in the mouth and pharynx responsible for this¹⁸ which additionally have a proposed benefit of protecting the host against periodontal and cariogenic bacteria²¹. Nitrite is also created by oxidation of nitric oxide, which is produced as a host signalling molecule and as a toxin as part of the host immune response^{18,21}.

The respiratory pathway for reducing nitrite in *N. meningitidis* involves two steps; nitrite is reduced to nitric oxide, which is then further reduced to nitrous oxide. This represents incomplete reduction, as a further reduction step is possible (shown in Figure 1.1), reducing nitrous oxide to dinitrogen gas^{18,22}.

Reduction of oxygen is favourable over nitrite reduction due to the redox potential differences. The redox potential of $\text{O}_2/\text{H}_2\text{O}$ is +820 mV, NO_2^-/NO is +348 mV, thus O_2 has a higher tendency to acquire electrons resulting in a electrochemically favourable reaction²³. The electron flow towards the oxidase is also preferred physiologically as it liberates more energy by virtue of the translocation of more protons than the reduction of nitrite. The translocated protons

Reduction	Enzyme
$\text{NO}_2^- \rightarrow \text{NO}$	AniA
$\text{NO} \rightarrow \text{N}_2\text{O}$	NorB
$\text{O}_2 \rightarrow \text{H}_2\text{O}$	<i>cbb</i> ₃

Table 1.1: The reductions catalysed by the respiratory enzymes in *N. meningitidis*

are ultimately used in the synthesis of ATP molecules for energy. This results in reduction of oxygen in preference to nitrite when both are present (in most cases).

Reduction of oxygen in *N. meningitidis* is carried out by the oxygen reductase cytochrome *cbb*₃ oxidase, a membrane-bound heme-copper oxidase²⁴. *cbb*₃ is capable of binding oxygen and nitric oxide, which means that during nitrite reduction (denitrification), the oxidase can be competitively inhibited (chemically) by the intermediate product of denitrification. *cbb*₃ can be permanently damaged at high concentrations of NO and O₂, as they can both bind at the *cbb*₃ active site and react together to form peroxy nitrite^{25–27}.

Nitrite is reduced by the nitrite reductase AniA, which is a copper containing reductase. This reduction does not involve translocation of protons, and thus does not produce any usable energy. Nitrite is reduced to nitric oxide which can then be further reduced by a nitric oxide reductase NorB. Since *N. meningitidis* is capable of reducing nitric oxide, a host toxin, directly, this may help it defend itself against part of the host immune response^{18,28} as has been shown in tissue culture by Anjum et al.²⁷.

The reduction processes carried out by these enzymes are shown in the table in Table 1.1.

The major source for electrons in both respiratory pathways is NADH, although electrons can also be obtained from pyruvate and lactate amongst others. These reduced substrates lead to reduction of ubiquinone to ubiquinol in the ubiquinone pool that exists within the bacteria. Ubiquinol is oxidised either by the cytochrome *bc*₁ complex or directly by the NorB enzyme whilst reducing NO to N₂O. Cytochrome *bc*₁ is oxidised by a number of intermediate cytochromes



Figure 1.2: Layout of the components of the respiratory system in *Neisseria meningitidis*. Oxygen reducing components are shown in green, nitrogen reducing components in red. Components transporting electrons are coloured light blue, and their transport is indicated by dashed arrows. Respiratory substrates are shown in dark blue, with corresponding arrows linking them to their reducing enzymes. Components which produce membrane potential are also indicated.

which act to transport electrons to the terminal oxidases; AniA and *cbb₃*. The *c₅* cytochrome transports electrons from the *bc₁* complex to AniA, and two cytochromes, *c_{2/x}* and *c₄*, transport electrons to *cbb₃*. It is not understood why *cbb₃* has 2 alternate cytochromes, and there is evidence to suggest that it can also be supplied, in a limited capacity, by the *c₅* cytochrome as well²⁹. The electron transport chain (ETC) is shown graphically in Figure 1.2.

In addition to the difference in favourability between the two respiratory pathways, there is also a great deal of regulation, both at the enzymatic and transcriptional level. Chemical inhibition also plays a part in regulation as briefly mentioned previously. Expression of AniA is regulated by two processes, the reduction of oxygen and the presence of nitrite. The presence of oxygen down-regulates the expression of an activator of AniA expression. This activator is FNR (fumarate and nitrate reduction regulator), and the presence of oxygen effectively means that AniA expression is repressed by the reduced expression of FNR. In *N.*

meningitidis, FNR appears to work slightly differently than in facultative anaerobes such as *E. coli*, in that FNR is still expressed at quite high concentrations of oxygen, and is itself down-regulated by a separate co-factor³⁰.

The presence of nitrite triggers the two component NarP/NarQ system which activates expression of AniA in response to increasing levels of nitrite¹⁸. The activity of AniA is also controlled by the competition for electrons by the other reductase enzymes in the respiratory chain. Both NorB and *cbb3* have a higher affinity for electrons than AniA, and as a result the presence of these enzymes (when active) has an inhibitory effect on AniA. The regulation of AniA is further complicated by the production of nitric oxide, and the presence of a protein, NsrR.

Nitric oxide has a direct inhibitory effect on the expression of AniA, as does the NsrR protein. Nitric oxide also inhibits the NsrR protein, leading to a de-repression of AniA²⁸. In the absence of nitric oxide, AniA is almost fully repressed by active NsrR. As NO concentrations increase, NsrR is inactivated allowing full activation of AniA. Once NO reaches a sufficiently high level it will begin to inhibit AniA^{18,30}.

NorB is less tightly regulated by respiratory components, as it is only acted upon by NsrR, however it is regulated by FNR and NrsR outside the respiratory chain³¹. This regulation by NsrR works in a similar way to how NsrR acts upon AniA. When there is no nitric oxide present, the NsrR acts to inhibit NorB since there is no substrate for it to reduce. In the presence of nitric oxide, NsrR is inhibited, leading to the activation of NorB which is now able to reduce NO to N₂O. In this case nitric oxide is acting as a de-repressor of NorB.

This complicated set of regulatory relationships between the different components of the respiratory pathways is shown in Figure 1.3.

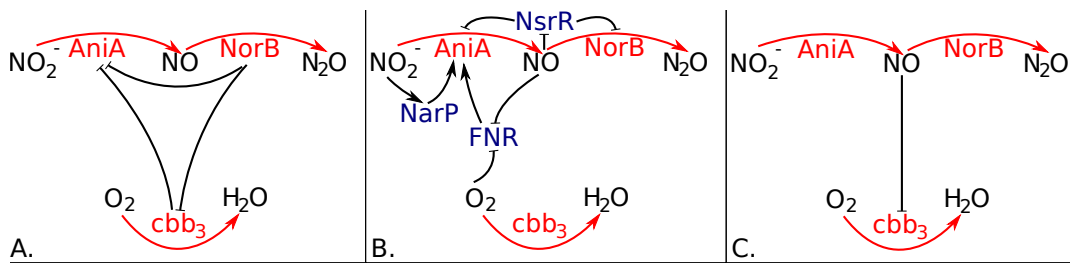


Figure 1.3: **Regulation of respiratory components in *Neisseria meningitidis*.** Enzymes and enzymatic reactions are shown in red. A. describes the regulation caused by competition for electrons between the respiratory enzymes. B. shows the genetic regulation, which also involves a number of additional components in dark blue. C. shows chemical inhibition of the respiratory components.

1.5 Respiratory Enzymes in *N. meningitidis*

1.5.1 Cytochrome cbb_3 oxidase

Cytochrome cbb_3 oxidase is a Haem Copper Oxidase (HCO) enzyme found commonly in proteobacteria. They have been characterised in at least *Pseudomonas denitrificans*, *Rhodobacter sphaeroides*, *Rhodobacter capsulatus* and *Bradyrhizobium japonicum*³². HCOs catalyse the reduction of Oxygen molecules to water whilst translocating protons across the inner membrane, from the cytoplasm to the periplasm, producing an electrochemical gradient.

HCOs can be separated into two categories by their electron donor type. Cytochrome c oxidases accept electrons from c -type cytochromes, and quinol oxidases accept electrons from ubiquinol. The major difference between these two categories is a missing Cu_A site in quinol oxidases³³. HCOs can be further broken down to 3 type, the aa_3 -type cytochrome c oxidase, the bo_3 -type quinol oxidase and the cbb_3 -type cytochrome c oxidase³⁴. Alternatively 5 different HCO subclasses may be classified, the aa_3 , caa_3 and cbb_3 -type cytochrome c oxidases, and the bo_3 and aa_3 -type quinol oxidases³⁵. All of these different types of cytochrome c oxidases are found in bacteria, whereas those in mitochondria are limited to aa_3 -type cytochrome c oxidases³⁶.

HCOs are themselves “defined by the primary sequence of their catalytic subunit, which is composed of twelve transmembrane helices with six invariant his-

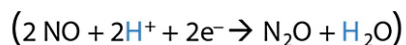
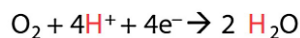
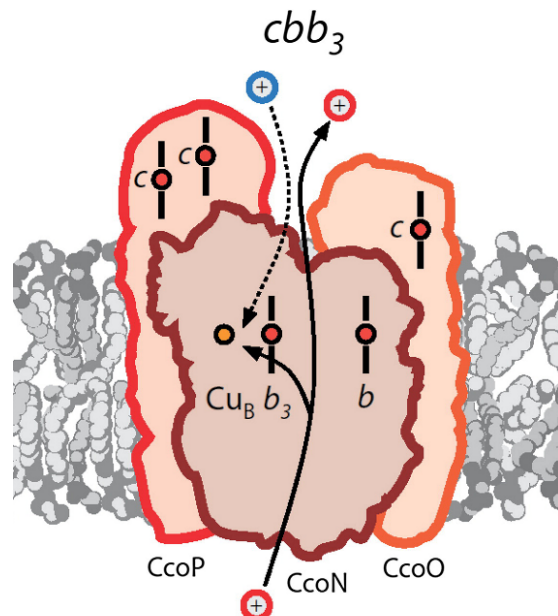


Figure 1.4: The *cbb₃* oxidase. This diagram shows the proton input pathway for Oxygen reduction shown in red, and the putative pathway for Nitric Oxide reduction in blue. Also shown are the 3 subunits and their associated heme centres. Adapted from Huang et al.³⁷.

tidines ligating three cofactors; a high spin heme (one His ligand) and a copper (3 His ligands) in the catalytic site and an additional low-spin heme (two His ligands)³⁷. Sequence alignment has also indicated that bacterial NO-reductase (NOR) might also be a divergent member of the HCO family. A schematic diagram of the *cbb₃* oxidase is shown in Figure 1.4, and the 3D structure of *cbb₃* from *Pseudomonas stutzeri* is shown in Figure 1.5. *cbb₃* is composed of three main subunits with CcoN being the catalytic subunit, which is related to subunit I of *aa₃* oxidases and NorB. This latter relation to NorB explains why *cbb₃* has some Nitric Oxide reduction activity (and conversely why NorB has some Oxygen reduction activity)³⁷. CcoN contains the catalytic site – the high-spin heme *b*₃-Cu_B – and a low spin heme *b*. CcoO is anchored in the inner membrane and contains just one *c-type* heme. CcoP contains two *c-type* hemes and is anchored to the inner membrane. CcoQ, the fourth subunit is small, and helps to stabilise the complex³⁷.

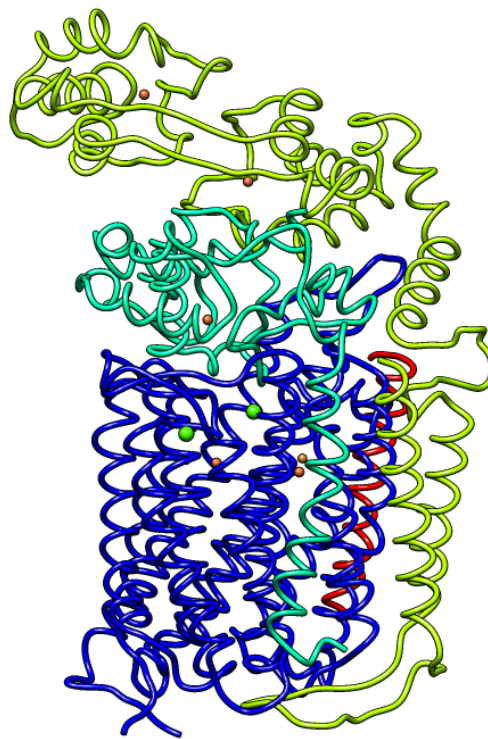
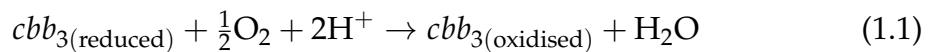


Figure 1.5: 3D Structure of *cbb₃* oxidase. This figure shows the structure of *cbb₃* from *Pseudomonas stutzeri*³⁸. CcoN is shown by the blue chain, with the heme and copper centres being brown. CcoP is shown by the green chain, and CcoO by the cyan chain. The PDB ID for this structure is 3MK7.

The mechanism of reduction of O₂ by *cbb₃* oxidases is not fully understood, as the reduction intermediates currently remain unknown³⁷. The cytochrome *cbb₃* oxidases have very low K_m values, allowing them to operate even under oxygen limiting conditions. *cbb₃* from *Bradyrhizobium japonicum* has a K_m of 7 nM, much lower than that of the mitochondrial aa₃ oxidase³⁹. This high affinity for oxygen suggests that *N. meningitidis* may have become adapted to surviving in the human host in areas of low oxygen concentration. Since this type of oxidase is also found in other human pathogens it is likely that it is used to allow those pathogens to survive in hypoxic environments in the human host⁴⁰.

The catalytic reaction for the *cbb₃* oxidase is:



1.5.2 NorB Nitric Oxide Reductase

Nitric Oxide Reductase is also a Haem Copper Oxidase enzyme which is found in bacteria as an integral membrane protein. There are three types of NOR, the cytochrome *bc* type complex (cNOR), the cytochrome *b* type complex lacking the cytochrome *c* component (qNOR) and a qNOR-type reductase that also includes Cu_A (qCu_ANOR). cNOR-type reductases receive electrons from soluble redox protein donors, whereas qNOR-type reductases receive electrons from quinol⁴¹.

The NOR in *N. meningitidis* is a qNOR-type reductase, and is encoded by the norB gene (NMB1622). It catalyses the reduction of Nitric Oxide to Nitrous Oxide receiving electrons directly from the quinone pool. Under microaerobic conditions this enzyme is important as during denitrification to support growth, Nitric Oxide accumulates as a result of reduction of Nitrite. The build up of Nitric Oxide inhibits aerobic respiration as it binds competitively to the *cbb*₃ oxidase. NorB protects the bacteria from the toxicity extracellular NO which is produced by host tissues and macrophages, which produce NO in quantity during infection²⁸.

The nitric oxide reductase in *Neisseria gonorrhoeae* is predicted to be an 84.3 kDa protein with significant sequence identity to *Ralstonia eutropha* and consists only of the NorB subunit⁴¹. The NorB protein is highly conserved across all *Neisseria* species as evidenced by sequence analysis⁴².

The catalytic reaction for NorB is:



1.5.3 AniA Nitrite Reductase

AniA nitrite reductase is an anaerobically induced, outer membrane associated protein which uses nitrite as an electron acceptor⁴³. It is a copper-containing protein found in many denitrifying proteobacteria.

Nitrite reductases catalyse the reduction of nitrite to nitric oxide with no associated proton translocation. There are two types of nitrite reductase, those that

have haem centres, and those which have copper centres. AniA in *N. meningitidis* is a copper-containing and accepts electrons from *c*-type cytochromes (*c*₅).

In *N. meningitidis* this enzyme is important during oxygen limiting conditions as it allows microaerobic respiration which can supplement growth by denitrification¹⁸.

Interestingly, according to its genome sequence *N. meningitidis* strain 053442 appears to lack the *aniA* gene in its entirety, suggesting that this strain would be unable to perform denitrification and respire anaerobically⁴². 32% of *N. meningitidis* strains sequenced by Barth et al.⁴² contain non-functional copies of *aniA* with frameshift mutations. These strains do still possess the *norB* gene for reducing Nitric Oxide however allowing them to prevent its toxic effects. It has been suggested by some that this may actually be evidence that *Neisseria meningitidis* is in the process of evolving away from denitrification to being a Nitric Oxide tolerant aerobe⁴⁴.

The catalytic reaction for AniA is:



1.6 Respiratory Electron Transporters in *N. meningitidis*

1.6.1 NADH Dehydrogenase

NADH (Reduced Nicotinamide Adenine Dinucleotide) Dehydrogenase is an inner membrane bound enzyme that catalyses the transfer of electrons from NADH to the quinone pool in many bacteria. There are three types of NADH dehydrogenase enzymes found in bacteria, NDH-1, NDH-2 and Na⁺-NDH. NDH-1 is related to Complex I of the mitochondrial respiratory chain and translocated protons across the inner-membrane whilst reducing the quinone pool⁴⁵⁻⁴⁷. NDH-2 does not have any proton pump activity, nor does it have any Fe-S clusters⁴⁸. Na⁺-NDH translocates Na⁺ ions across the membrane⁴⁹. The NADH dehydrogenase of *N. meningitidis* is of the NDH-1 type²³.

Mitochondrial complex I catalyses the oxidation of NADH and the reduction of ubiquinone whilst translocating 4 protons across the membrane. It does so using the following reaction scheme:

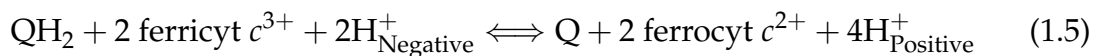


1.6.2 Cytochrome *bc*₁ Complex

The cytochrome *bc*₁ complex oxidises quinols and reduces metalloprotein electron transporters (usually c-type cytochromes). It is an important part of bacterial respiratory chains, and is also analogous to the mitochondrial complex III⁵⁰. Whilst catalysing the reduction of ubiquinol and the oxidation of c-type cytochromes, the *bc*₁ complex also translocates protons across the inner membrane from the cytoplasm to the periplasm producing an electrochemical gradient. The *bc*₁ complex is found in both Gram negative and Gram positive bacteria, however *E. coli* has no *bc*₁ complex. The homolog the *b*₆*f* complex is also used for electron transfer during photosynthesis in higher plants and phototrophic bacteria⁵¹.

In bacteria the *bc*₁ complex is formed of one cyt *b* subunit which contains two *b*-type hemes, one cyt *c*₁ subunit which contains a single *c*-type heme and an Rieske iron-sulfur protein. These subunits form the two catalytic sites of the *bc*₁ complex. The reduction of ubiquinol appears to occur in a concerted manner at 1 of these sites, Q_o⁵¹. Electrons from the quinol are shared between two reaction chains, 1 which transfers electrons to the high-potential iron-sulfur protein and *c*₁, and another which transfers electrons to the low-potential cytochrome *b*. The other catalytic site Q_i uses the two electrons from the high and low potential chains to reduce quinone, or other metalloprotein electron transporters^{52,53}. This modified Q-cycle is shown in Figure 1.6.

The reaction scheme for the *bc*₁ complex is:



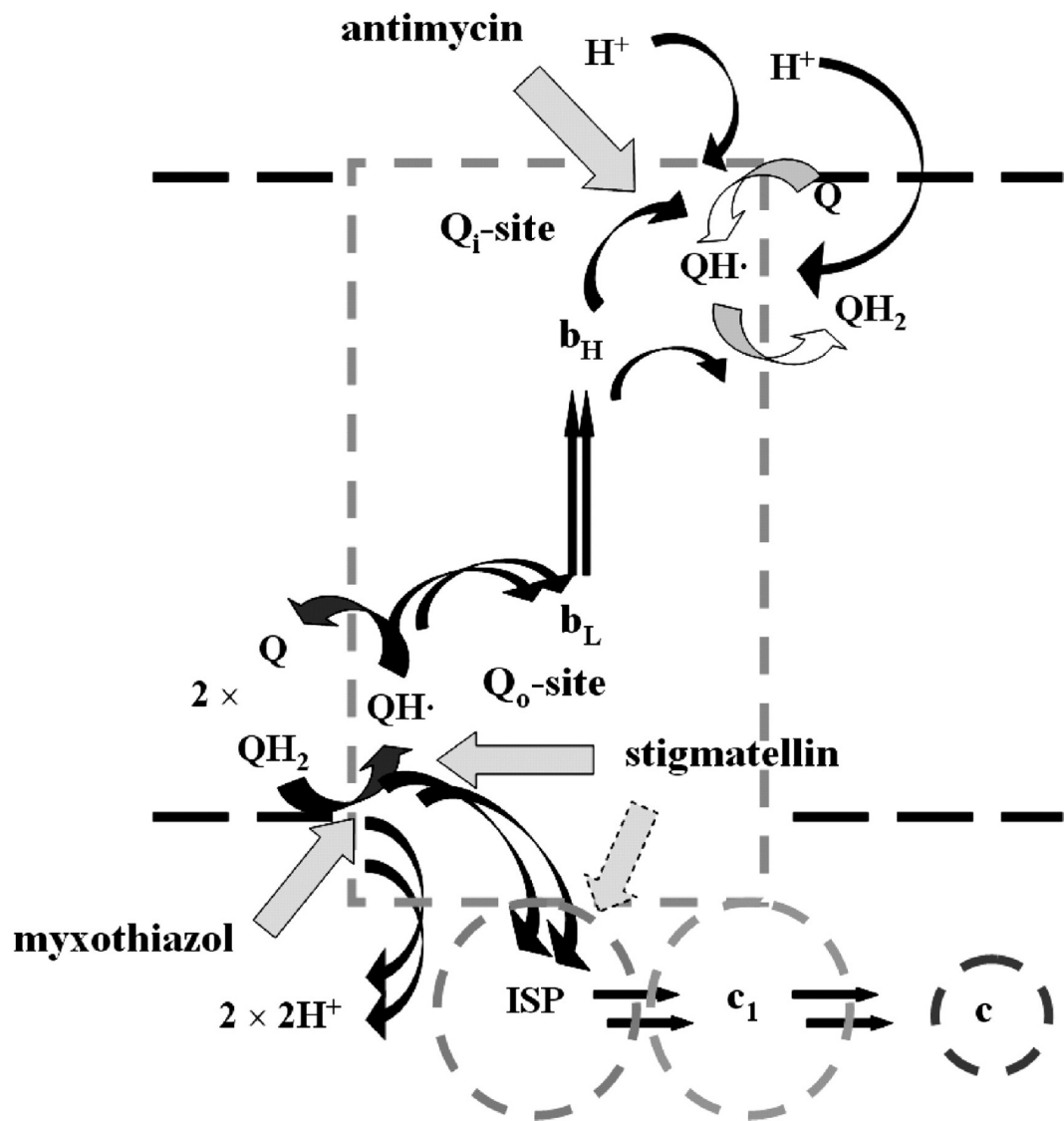


Figure 1.6: The modified Q-cycle used by the bacterial *bc*₁ complex. The cyt *b* subunit is represented by the *dashed gray* outline, and contains the *Q_o*- and *Q_i*-sites, connected by hemes *b_L* and *b_H*. The ISP and cyt *c*₁ catalytic domains and cyt *c* are represented by *dashed darker gray* circles. Electron transfer steps are shown by *dark narrow arrows*, proton release and uptake by *lighter arrows*, binding and release of quinone species by *broad curved arrows* (dark gray for *Q_o*-site, light gray for *Q_i*-site). Sites of inhibition are indicated by *block arrows* showing sites at which the bound inhibitor displaces quinone species. The *dashed inhibitor arrow* indicates that the reaction of ISPH with cyt *c*₁ is blocked by the interaction of ISPH with stigmatellin at the *Q_o*-site. Adapted from Crofts et al.⁵⁴.

1.6.3 Cytochromes c_4 , c_x and c_5

Cytochromes c_4 , c_x and c_5 are soluble c -type cytochromes. These are small heme proteins that are found in the periplasm and are loosely associated with the inner membrane. Along with their presence in proteobacteria, the c -type cytochromes also form part of the mitochondrial respiratory apparatus in the form of cytochrome c . Bacterial c -type cytochromes perform a very similar function to mitochondrial cytochrome c in that they transport electrons from the bc_1 complex to the terminal reductases. Cytochromes c -552, c -553 & c -554 from algal chloroplasts and cyanobacteria, c_2 from purple photosynthetic bacteria and c_4 and c_5 from *Azotobacter vinelandii* along with many others all have sequence and structural homology with mitochondrial cytochrome c ⁵⁵. The mitochondrial and bacterial soluble cytochromes all fall within Ambler's Class I of c -type cytochromes⁵⁶. Class I c -type cytochromes have their heme-attachment site towards the N-terminus, and the sixth ligand is provided by a methionine residue 40 residues further down the chain towards the C-terminus⁵⁶[Re-write this sentence, it is almost plagiarism!]. Cytochrome c_4 is a diheme cytochrome and is the electron donor to cbb_3 transferring electrons from the bc_1 complex in *N. meningitidis*^{23,29,57}.

Cytochrome c_x is a monoheme cytochrome which is also able to transfer electrons from the bc_1 complex to cbb_3 ^{23,29}.

Cytochrome c_5 is a diheme cytochrome which appears to be membrane associated. It transfers electrons from the bc_1 complex to AniA during Nitrite reduction^{23,29}.

1.6.4 Quinone Pool

The quinone source in *N. meningitidis* is predicted to be ubiquinone²³. Ubiquinone, also known as Coenzyme Q₁₀ is found in most eukaryotes. It is a vitamin-like lipid soluble molecule with a long tail made of 10 isoprenyl subunits. This is shown in Figure 1.7.

In its oxidised form it is known as ubiquinone, whereas when reduced it is

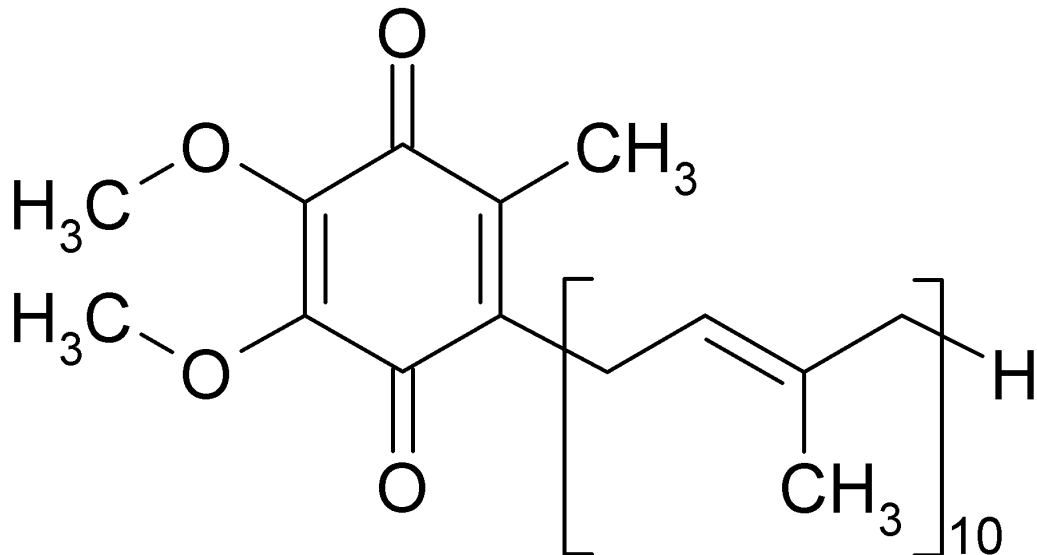


Figure 1.7: Structure of the ubiquinone molecule.

called ubiquinol. In the *N. meningitidis* respiratory chain, ubiquinone is reduced to ubiquinol by the acceptance of 2 electrons from NADH (amongst others). Ubiquinol then donates electrons either directly to the terminal reductase NorB, or to the *bc*₁ complex.

1.7 Respiration Regulatory Proteins in *N. meningitidis*

1.7.1 NsrR - Nitrite Sensing Repressor Protein

“NsrR is an NO-sensing Rrf2-type transcriptional repressor”⁴². In *N. meningitidis* (and *N. gonorrhoeae*) it negatively regulates *aniA* and *norB*, and derepression is caused by NO^{28,30,31}. Rrf2 proteins have two DNA-binding helix-helix domains³⁰, with a putative iron-sulfur cluster inbetween. The binding of the iron-sulfur cluster, which is expected to be by NO in NsrR, would perturb the structure of the repressor protein and prevent DNA binding³⁰.

norB is expressed in a somewhat constitutive manner, in that with no repression *norB* is still expressed to some extent⁵⁸. NsrR represses this expression until NO is present, at which point *norB* can be expressed and the NorB enzyme can start removing the NO that is present.

aniA is positively regulated by FNR, but this seems to be quite insensitive to oxygen in *N. meningitidis*, thus *aniA* would be expressed even at 60 to 80% air saturation with oxygen³⁰. *aniA* therefore needs to be corepressed in order to prevent it being expressed excessively in aerobic conditions.

1.7.2 FNR - Fumarate and Nitrate Reductase Regulator

Fumarate Nitrate Reductase is a transcriptional activator which binds to a 4Fe-4S cluster under anaerobic conditions. When oxygen concentrations are low, FNR causes increased expression of proteins that are necessary for anaerobic respiration. “The presence of the 4Fe-4S cluster is correlated with protein dimerization, which enables it to bind promoter DNA”⁵⁹. Four cysteine residues are believed to be ligated to the iron-sulfur cluster and these are required for FNR function. The oxygen sensitivity of FNR is achieved by the iron-sulfur cluster breaking down into 2Fe-2S via 3Fe-4S which is unable to bind DNA. In *N. meningitidis*, *aniA* expression is directly linked to the presence of FNR¹⁸. When no NsrR is present, *aniA* expression continues even up to 80% oxygen saturation suggesting that FNR is actually quite insensitive to oxygen, an unusual response compared to FNR from *E. coli*. FNR also becomes less sensitive to oxygen when it is bound to its cognate DNA⁵⁹.

1.7.3 NarQ/NarP - Nitrite Response Sensor/Regulator

NarP and NarQ are a two component signal transduction pathway that regulate expression of *aniA* in *Neisseria*. NarQ is the sensor protein located in the inner membrane, while the regulator protein, NarP is found in the cytoplasm. Being a two component system, the sensor protein phosphorylates the regulator allowing it to bind the target DNA (which may consist of multiple sequences) to activate expression of genes.

In *N. gonorrhoeae*, NarP was shown to enhance the expression of *aniA* in response to the presence of nitrite, as a mutant lacking *narP* was significantly slower

at growing under denitrifying conditions⁶⁰.

In *N. meningitidis* expression of *aniA* is increased greatly in conditions of high nitrite concentration¹⁸. This effect is much more pronounced than simply being in oxygen limiting conditions. FNR appears to be required for *aniA* expression even when NarP/NarQ are present¹⁸. This suggests that the organism is intentionally preventing expression of nitrite reducing components until there is both a high concentration of nitrite *and* a very low concentration of oxygen. This is plausible as even under oxygen limiting conditions oxygen reduction is still favoured over nitrite reduction.

1.8 Organisation of Respiratory Chains in Other Bacteria

The respiratory chain of *N. meningitidis* is shown in a simplified form in Figure 1.8. The components are coloured consistently throughout this section to allow easy comparison between the respiratory chains being discussed. As discussed previously, the respiratory chain of *N. meningitidis* contains an initial electron donor, in this case NADH dehydrogenase. In fact there are a number of other electron donors, but they are not discussed here as NADH provides most of the electrons to the respiratory chain. There is also a quinone pool, consisting of ubiquinone/ubiquinol, intermediate *c*-type cytochromes and terminal reductases.

1.8.1 The Respiratory Chain of *Paracoccus denitrificans*

The respiratory chain of *P. denitrificans* is shown in Figure 1.9. It is quite similar to that of *N. meningitidis* with the exception of having a larger number of terminal reductases, and the ability to perform complete denitrification. The chain possesses an initial electron donor, a quinone pool, intermediate cytochrome electron transporters and terminal reductases.

The *bc₁* complex of *N. meningitidis* is present as an analogue (Ubiquinol-cyt *c* oxidoreductase), and the chain includes 2 further downstream *c*-type cytochromes. *P. denitrificans* has 3 terminal oxygen reductases, *ba₃*, which oxidises the quinone



Figure 1.8: **Branched electron transport chains of *N. meningitidis*.** Blue denotes initial electron donor, red denotes quinone pool, purple denotes cytochrome electron transporters and green denotes terminal reductases. UQ = ubiquinone.

pool directly, and cbb_3 and aa_3 which oxidise the c -type cytochromes. All three oxygen reductases are HCOs. The branching of the aerobic ETC is quite common among bacteria, but the reason for this is not currently fully understood.

The nitro-reductases found in *P. denitrificans* are capable of complete denitrification as described in Figure 1.1. The nitrate reductases directly oxidise the quinone pool, whereas the nitrite and nitric oxide and nitrous oxide reductases oxidise the c -type cytochromes instead.

As with *N. meningitidis* there are a number of potential initial electron donors, but only NADH is shown for simplicity of comparison.

1.8.2 The Respiratory Chain of *Escherichia coli*

The respiratory chain of *E. coli* is shown in Figure 1.10. It can be seen to be quite distinct from other bacteria, and indeed from the mitochondrial respiratory chain. The most obvious difference between *E. coli* and many other bacteria is the lack of c -type cytochromes. The terminal reductases are able to be reduced directly



Figure 1.9: **Branched electron transport chains of *Paracoccus* species.** Blue denotes initial electron donor, red denotes quinone pool, purple denotes cytochrome electron transporters and green denotes terminal reductases. UQ = ubiquinone. Electron transfer between cytochromes c_{552} and c_{550} has not been demonstrated experimentally but is possible, given the redox potential of the proteins. Adapted from Baker et al.⁶¹.

by the quinone pool. Additionally, under anaerobic conditions, the quinone pool changes from being ubiquinone/ubiquinol to menaquinone/ubiquinol.

E. coli also has a number of different terminal reductases in the form of cyt bo_3 and cyt bd . Cyt bo_3 is an HCO and is structurally very similar to cyt aa_3 . Cyt bd shows no sequence similarity with the HCO superfamily and has no Cu_B site. Cyt bd has a much higher affinity for oxygen than cyt bo_3 so is synthesised at low oxygen concentration.

E. coli is also capable of partial denitrification and possesses enzymes to reduce nitrate and nitrite, which are also under the regulatory control of FNR. The reduction of nitrite differs from *N. meningitidis* and *P. denitrificans* as NO_2^- is not reduced to NO, but to NH_4^+ instead.

As with *N. meningitidis* and *P. denitrificans* there are a number of potential initial electron donors, but only NADH is shown for simplicity of comparison.



Figure 1.10: **Branched electron transport chains of *E. coli*.** Blue denotes initial electron donor, red denotes quinone pool and green denotes terminal reductases. UQ = ubiquinone. Under anaerobic conditions, ubiquinone is replaced by menaquinone. Adapted from Nicholls and Ferguson⁶².

1.9 Systems Biology

Systems biology is the process of “studying biological systems in their whole [...], reinforced by high throughput [...] molecular tests and considerable sophistication in computational modelling”⁶³. Systems biology “combines approaches and methods from systems engineering, computational biology, statistics, genomics, molecular biology, biophysics and other fields”⁶⁴.

The aim of Systems biology is to take our detailed understanding of organisms beyond the molecular and cellular level. These are the levels to which the disciplines of molecular and biology and biochemistry (among others) are more suited. It aims to take our understanding to the level of the entire “complex system”. Which is to say we gain understanding into the way the organism behaves as a whole, rather than just having knowledge of the individual parts.

The level of complexity in biological systems is far greater than the popular notion of what defines a complex system, however. Biological systems consist

of multiple different individual elements each performing specific tasks interacting with each other to create 'coherent' behaviour. This is very different from popular complex systems which are collections of simple, identical components interacting to produce 'complex' behaviour⁶⁵.

Gaining understanding such a complex system is difficult, and Kitano suggests that it requires insight into the following properties⁶⁶:

1. **Structure of the system.** This includes the way the system interactions are "laid out" both at a component level and an organismal level.
2. **The dynamics of the system.** This involves understanding how the organism behaves under any given conditions over a particular time period. This may include understanding how the metabolic processes change under these conditions etc.
3. **How the system is controlled.** The control mechanisms can be tailored to suit the desired function or to minimise the chance of malfunction.
4. **How the system is designed.** "Trial and error" experimentation can be done away with, as the system can be designed based on defined properties, backed up by models and simulations.

The level of integration between systems biology approaches and experimentation can be seen in Figure 1.11. This shows the iterative cycles that are necessary to gain understanding in both areas. The experimentation provides data to refine and develop the system model, and data from that model can go on to improve the design of the experiment.

Systems biology extends further into a computational discipline when you consider that if you can create a model of a system, you can potentially run a simulation of the system using the model. Simulations can be developed for multiple stages of the process, from molecular to organismal. Simulations of interactions based on gene regulatory network models are being studied⁶⁷, as are complete plant development models⁶⁸⁻⁷⁰.

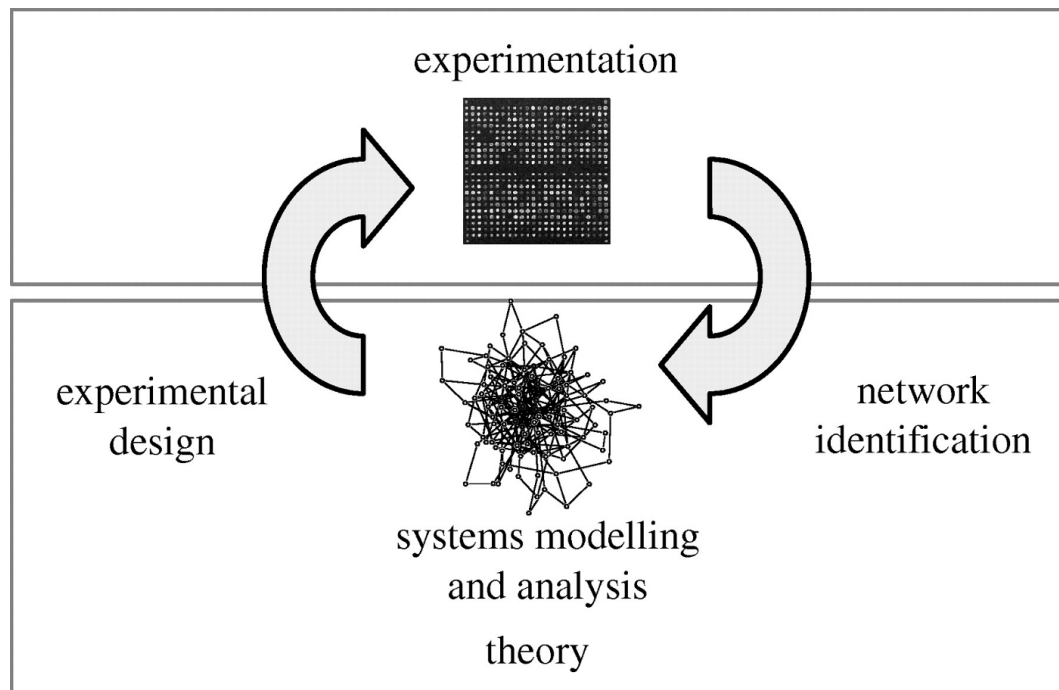


Figure 1.11: **Systems biology cycle.** Interactions between experimental analysis and theoretical approaches, and the main tasks for theory at the interfaces. Doyle and Stelling⁶⁴

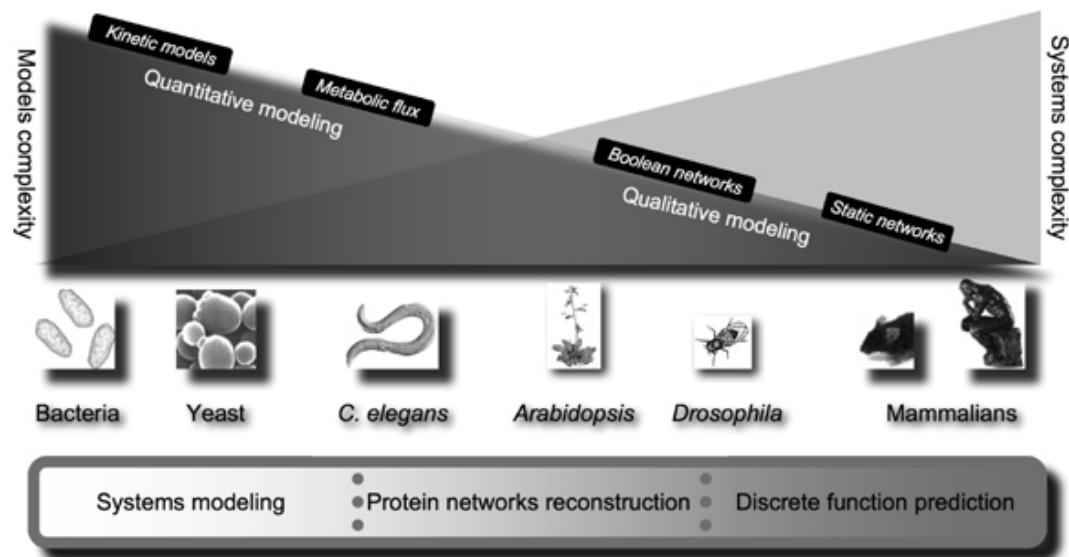


Figure 1.12: **System complexity.** Diagram showing how system complexity varies across organisms, and how the complexity of the models we can produce is currently the inverse of systems complexity. Kahlem and Birney⁶³

Figure 1.12 shows one of the limitations of the current technology “powering” systems biology. As organisms get more complex, the models we can produce get less complex and less quantitative⁶³. This concomitant lack of data in models of complex organisms decreases the likelihood of being able to produce a simulation of the model. We might be able to simulate *aspects* of a complex organism, such as the human heart⁷¹ but we are still a long way from being able to simulate the entire human body.

For simpler systems, like yeast, or *E. coli* an enormous amount of data already exists about individual gene regulation, protein interactions etc. and it is possible to build sophisticated models of the entire gene regulatory network and more^{72,73}.

A systems biology approach to understanding the mechanism of respiration in *Neisseria meningitidis* is necessary as there are a number of components in the system which are inherently unmeasurable.

1.10 Modelling

1.10.1 Modelling Respiratory Systems

A limited amount of modelling has been carried out on bacterial respiratory chains, these focused on the denitrification pathway and treated the pathway as a simple electrical circuit⁷⁴. An alternative approach involved modelling respiration using “P systems” which are probabilistic models of events. This assigned a probability of each reaction happening, dependant on the state of the system and then iterated through a given set of steps evaluating probabilities and altering values based on the outcome⁷⁵. This approach to modelling was limited in that it was only predicting the quantities of 1 component in each of 2 “compartments”; oxygen in the cell membrane and carbon dioxide in the thylakoid membrane (the model was developed using cyanobacteria).

Some modelling of parts of the respiratory chain in *E. coli* have also been modelled. Peercy et al.⁷³ created a kinetic model of how cytochrome production is

regulated by oxygen using differential equations. They created a set of differential equations to describe the relevant reactions and then populated the model using parameters gathered from the literature.

Since when modelling respiration in a cell, the most important factor is the change in concentration of components over time without any particular spatial constraints, ordinary differential equations (ODEs) are an appropriate technique. In these systems the model does not change with regard to the spatial arrangement of any of the components. If the system requires changes in time *and* space, then partial differential equations (PDEs) would be necessary (and more complicated)⁷⁶.

Ordinary differential equations only depend on one variable; the time (t). In this case, the change in concentration over time for each component can be modelled as a single differential equation. For multiple components this leads to multiple differential equations with some that rely on the result of another (if the rate of one reaction is directly related to the concentration of another component). These ODEs must then be solved in parallel at a suitable time-scale.

Complications arise when using differential equations if the processes are considered to be stochastic, as a differential equation model assumes that every component can have a continuous value, which is not the case as molecules are discrete. However if the system being modelled is sufficiently large, this effect can be ignored. If the reaction component size is small (< 100s of molecules) stochastic simulation algorithms have to be used as described by Gillespie⁷⁷. This method requires far more computation than solving ODEs, as the model will spend most of its time calculating values for reactions involving large molecules even though this is not necessary as the reaction is not stochastic. Additionally, the time interval used between reaction steps is usually very small, meaning the simulation progresses slowly⁷⁶.

1.10.2 Modelling Tools

A number of software packages exist that are capable of this type of modelling such as the Systems Biology Workbench⁷⁸ and COPASI⁷⁹. These allow you to enter biochemical reactions in a format familiar to biologists, and have pre-defined libraries for types of reactions such as mass-action, or one with Michaelas-Menten kinetics etc. The mathematical equations are then derived automatically from the reactions and can be modified by hand if necessary. Parameters for the mathematical equations must be entered, and these will usually be derived from experimental data, or in some cases educated guesses (at least initially). Once a parameter set has been created, the modelling software can run a time-course using a relevant solver-algorithm. COPASI includes 4 solvers, LSODA (Livermore Solver for Ordinary Differential Equations)⁸⁰ for deterministic systems (such as ODEs), Gibson-Bruck⁸¹ for stochastic systems and Runge-Kutta and LSODA for hybrid systems (where portions are not considered to be stochastic).

1.11 Aims

The over-arching aim of this study was to produce a working mathematical model of the respiratory system of *N. meningitidis* which has been refined and parametrised by experimental biological data. This mathematical model should be able to accurately simulate experimental datasets with known outcomes, and also be able to predict the outcome of experiments that have not been performed. This model, will also be able to provide insight into the states of various components throughout the respiratory process, such as enzymatic oxidation states, some of which are very difficult, if not impossible, to obtain in an *in vivo* study.

The layout of *N. meningitidis* respiratory chain, even though it is longer than that of the model organism *Escherichia coli* is more similar to most other bacteria. This, along with its profound medical importance make it an excellent target for the type of mathematical modelling described above.

The individual aims of the study are therefore:

1. Construct a mathematical model of the *N. meningitidis* respiratory chain.

This will involve the conversion of the kinetic reactions involved in respiration into mathematical equations that can be linked together, and if justified simplifying the chain.

2. Obtaining experimental data on respiratory rates and enzyme kinetics.

This will involve performing experiments on respiring *N. meningitidis* and recording the concentrations of respiratory substrates under different conditions.

3. Parametrise the model using experimental data. To do this a system will

need to be developed which can iteratively fit experimental data to specific parts of the mathematical model.

Chapter 2

Materials and Methods

2.1 *Neisseria meningitidis* Strains Used in This Work

Name	Description	Source
MC58	Wild-Type Strain	McGuinness et al. ⁸²
Δ norB::spc ^r	Wild-Type with insertion of spectinomycin resistance cassette into norB gene	Heurlier et al. ²⁸
Δ nsrR::spc ^r	Wild-Type with insertion of spectinomycin resistance cassette into nsrR gene	Rock et al. ³⁰
Δ norB::spc ^r - Δ nsrR::tet ^r	Wild-Type with insertion of spectinomycin resistance cassette into norB and insertion of tetracycline resistance cassette into nsrR genes	Heurlier et al. ²⁸
Δ aniA::spc ^r - Δ nsrR::tet ^r	Wild-Type with insertion of spectinomycin resistance cassette into aniA and insertion of tetracycline resistance cassette into nsrR genes	Heurlier et al. ²⁸

Table 2.1: Bacterial strains and sources

2.2 Culturing *Neisseria meningitidis*

2.2.1 Growth of *Neisseria meningitidis*

N. meningitidis strains were grown on plates on Columbia Agar Base (CAB) with defibrinated horse blood, and in liquid culture in Müller-Hinton Broth (MHB).

Plates were prepared by adding horse blood to a final concentration of 5% to molten agar, and poured into plastic petri dishes. After streaking with *N. meningitidis* the plates were incubated at 37 °C in a 5% carbon dioxide/air mixture.

Aerobic liquid cultures were grown in 10 ml MHB with 10 mM NaHCO₃ in plastic Sterilin tubes, and incubated at 37 °C at 200 rpm. Microaerobic cultures were suspended in 20 ml MHB, 10 mM NaHCO₃ in plastic Sterilin tubes, incubated at 37 °C at 100 rpm.

2.2.2 Preparation of Antibiotic Selective Media

Liquid stock solutions of required antibiotics were either added directly to liquid culture, or, if growing on plates, to the molten agar when also adding horse blood. The final concentrations of antibiotics are given in Table 2.2.

Antibiotic	Final concentration ($\mu\text{g}/\text{ml}$)
Spectinomycin	50
Tetracycline	2.5
Chloramphenicol	50

Table 2.2: Final antibiotic concentrations

2.2.3 Preparation of Frozen Bacterial Stocks

Bacteria were grown in liquid culture until late log phase prior to harvesting. Liquid cultures were then centrifuged at 4000 g for 15 minutes, and the pellet was then re-suspended in a 25% glycerol, 25% water and 50% MHB, all of which had been autoclaved beforehand. The bacterial stocks were then frozen at -80 °C.

2.2.4 Streaking Plates for OD to CFU Ratio Calculation

Bacterial cultures were grown overnight and then transferred into aerobic liquid culture and samples taken throughout the day to obtain a range of different optical densities. The optical density was recorded at 600 nm on a Jenway 6305 Spectrophotometer (Bibby Scientific Limited, Staffordshire UK), and each sample was serially diluted to the following levels: 10^{-5} , 10^{-6} and 10^{-7} . 100 μl of each of these dilutions was plated on a fresh blood agar plate and left to grow overnight. The following morning the number of colonies on each plate was counted and used to create a simple conversion factor for Optical Density to Colony Forming Units.

2.3 Measuring Oxygen Concentration

Oxygen concentration in respiring cultures was measured using a Clark electrode⁸³ from Rank Brothers, Cambridge, UK. This electrode has a silver anode and a platinum cathode and uses a saturated potassium chloride solution as electrolyte. The electrode is set at the bottom of a 7 ml reaction chamber separated from its contents by a thin Teflon™ membrane. This apparatus is shown in Figure 2.1. The Teflon™ membrane is permeable to dissolved oxygen, which is reduced by the electrode producing a measurable electrical current. The reaction chamber is maintained at 37 °C by an attached water bath. When performing experiments, 5 ml of culture is added to the reaction chamber, which is stirred by use of a magnetic flea, and the chamber covered with a plastic stopper. The stopper has a number of holes through which the NO probe, or Hamilton syringe can be inserted. Data is collected by attaching the electrode to an external data logger (Pico ADC20, Pico Technology).

2.3.1 Calibration of Oxygen Electrode

Calibration of the oxygen electrode assumes that anaerobic water will not produce any measurable current at the electrode. Oxygen saturated water contains



Figure 2.1: **Exploded view of the oxygen electrode.** This assembly sits atop a Rank Brothers Digital Model 10 Controller which acts as a magnetic stirrer and provides the polarising voltage to the electrode (Rank Brothers Ltd⁸⁴).

210 μM Oxygen at 37 °C⁸⁵. 5 ml of ultra pure ($18 \text{ M}\Omega$) water was added to the electrode chamber, and then aerated to saturation by use of a Pasteur pipette. The maximum value recorded by the data logger then corresponds to a concentration of 210 μM Oxygen, with the relationship between mV as recorded against concentration being linear.

2.4 Measuring Nitric Oxide Concentration

Nitric Oxide concentration was measured using a Nitric Oxide probe (ISO-NOP, World Precision Instruments) connected to a Nitric Oxide Meter (ISO-NO mkII, World Precision Instruments). This is also a Clark type electrode, contained within a steel sleeve with a semi-permeable membrane separating the working electrode from the system being measured^{86–88}. The NO probe is inserted through one of the holes in the plastic lid of the reaction chamber of the oxygen electrode assembly. The tip of the electrode should be immersed in the culture, with care being

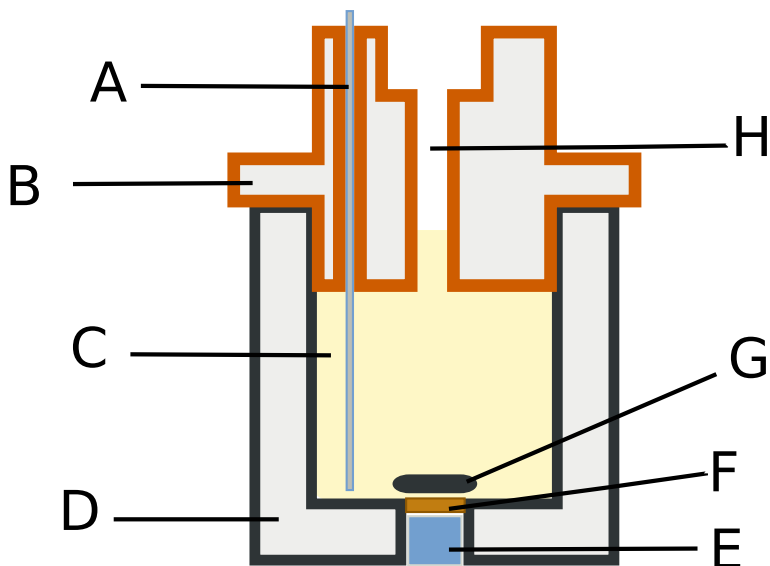


Figure 2.2: Oxygen electrode chamber with nitric oxide probe inserted. This shows the set up used to obtain all oxygen and nitric oxide measurements. A - ISO-NOP Nitric Oxide probe. B - Electrode chamber cap. C - Culture media. D - Oxygen electrode chamber. E - Oxygen working electrode. F - Teflon™ membrane. G - Magnetic Flea. H - Air gap.

taken not to trap any air bubbles on the surface of the probe. The sensor is also attached to the same data logger as above. In this way both Oxygen and Nitric Oxide concentrations can be measured in parallel. A diagram of the apparatus when set up is shown in Figure 2.2.

2.4.1 Calibration of Nitric Oxide Electrode

Calibration of the nitric oxide electrode relies on adding known quantities of Nitric Oxide to the electrode chamber. Sodium Nitrite will liberate Nitric Oxide with a 1:1 ratio when added to a solution of excess Potassium Iodide and Sulfuric acid based on the following reaction:



5 ml of 0.1M Potassium Iodide/Sulfuric Acid was added to the electrode chamber and allowed to stabilise. Then, increasing concentrations of Sodium Nitrite solution were successively added to produce a standard curve of Nitric Oxide concentration to recorded electrode mV. The volume and concentrations of Sodium

NaNO_2 Concentration (μM)	Volume (μl)	NO Concentration (nM)
10	50	99
100	25	591
100	50	1561

Table 2.3: Sodium Nitrite concentrations used to calibrate ISO-NOP Nitric Oxide sensor.

Nitrite added to the electrode chamber are detailed in Table 2.3.

2.5 Measuring Nitrite Concentration (Griess Assay)

Nitrite concentration in liquid culture was determined using the colorimetric assay described by Nicholas and Nason⁸⁹. This reaction is based on chemical diazotization which uses sulfanilamide and *N*-1-naphthylethylenediamine dihydrochloride (NED) under acidic (hydrochloric acid) conditions. Nitrite is converted to nitrous acid under acidic conditions and this then forms a diazonium salt with the sulfanilamide. The diazonium salt combines with NED and forms a pink azo dye which can be detected using absorbance spectrophotometry at a wavelength of 540 nm. Depending on the expected concentration of nitrite, different sample volumes are used in the assay. The most common sample volume used was 25 μl which allows detection up to around 1 mM nitrite with the following reagent volumes: 875 μl of 1% sulfanilamide in 1 M HCl and 100 μl of 0.02% NED in 1 M HCl. When using different sample volumes, the volume of sulfanilamide was altered such that the volume of sample + sulfanilamide always equalled 900 μl . After adding the sample to the reagents, it was left for 20 minutes for the colour to develop, then the absorbance at 540 nm was measured and compared to a standard curve.

2.6 Nitric Oxide Production

Solutions of Nitric Oxide were prepared using a method derived from one described by Aga and Hughes⁹⁰. The apparatus setup is shown in Figure 2.3. A



Figure 2.3: **NO making apparatus.** 1 & 2 - N₂ release valves. 3 - Pressure equalizing dropping funnel, containing 50 ml 4 M H₂SO₄. 4 - Stirred, round-bottomed flask, containing 200 ml 2 M NaNO₂. 5 - Dreschel bottle with sintered bulb, containing \approx 200 ml 1 M NaOH ($\frac{2}{3}$ full). 6 - Dreschel bottle with sintered bulb, containing \approx 200 ml dH₂O ($\frac{2}{3}$ full). 7 - Small glass bottle with rubber septum and needle entry valve, containing dH₂O $\frac{2}{3}$ full. This bottle either needs to also have a gas exit needle, or at least not be sealed during the process.. 8 - To N₂ gas bottle. Viton rubber tubing is used for all the flexible hoses in this apparatus.

concentrated solution of Sulfuric acid is added from a pressure-equalizing dropping funnel to a concentrated solution of Sodium Nitrite solution in a stirred, round-bottomed flask. This releases NO gas which passes through a solution of Sodium Hydroxide to neutralise any Sulfuric acid present, then through distilled water to remove any Sodium Hydroxide before finally being bubbled into a collection vessel with a sealed rubber septum containing distilled water. The concentrations of the chemicals used in this preparation are shown in Table 2.4. The system should be set up in a fume cupboard as shown in Figure 2.3 and sparged with N₂ gas for 15 minutes (the dropping funnel will allow gas to pass into the round bottomed flask even when the bottom valve is closed). The H₂SO₄ should be sparged separately. Valve 2 should be left open at all times. After sparging close valve 1 and then add the Sulfuric acid drop-wise from the drop-

Chemical	Volume (ml)	Concentration (M)
NaNO ₂	200	2
H ₂ SO ₄	50	4
NaOH	200	1

Table 2.4: Chemicals needed for preparation of Nitric Oxide solution.

ping funnel. Brown gas will start to bubble through to the collection vessel. This apparatus should produce enough NO gas to saturate several small (10 ml) collection vessels which should have the needle removed and be sealed once saturated. Once all the Sulfuric acid has been added leave the reaction to finish which could take 1-2 hours. Before disassembly the apparatus should be sparged with N₂ gas to remove residual NO gas.

The eventual concentration of NO in the solution will vary depending on the temperature, but at 25 °C in ultra pure (18 MΩ) water the concentration will be between 1.88 and 1.96 mM^{90,91}.

Chapter 3

Model - Construction and Parameters

3.1 Construction

The model was constructed based on existing knowledge of the respiratory chain in *Neisseria meningitidis* from the ETC shown in Figure 1.2 (Chapter 1). No *a priori* assumptions are made about separation of time-scales that would permit the use of Michaelis-Menten kinetics, as the rates of intermediate reaction steps are not known. This approach also permits tracking of the oxidation state of all the intermediates which allows understanding and offers the potential for predictions that may be explored in future *in vivo* studies.

The model was generated as a set of ordinary differential equations which describe the bulk-average concentration of substrates, products, enzymes and their activity within a well-mixed vessel. No assumptions are made about the bacterial population structure or the variations in concentrations of substrates between the bulk media and within the bacterial cells. Stochastic effects are ignored at the protein level, but they are unlikely to be of importance. Initially protein production is largely ignored as the switching mechanism is thought to happen on a time-scale that is much shorter than the transcription and translation of new proteins, they are therefore assumed to be expressed constitutively except where stated otherwise. However some datasets were available in the published literature¹⁸ that suggested otherwise, and were tested using an extension to the model described

below which includes transcription and translation of certain components.

3.1.1 Normalising the Data

The model contains no implied information about cell density. This means the values for various component concentrations will differ between experiments. Initially the optical density of cultures was used to determine the cell density however experiments proved that this was not a completely reliable proxy as the optical density is also affected by dead cells. Using optical density as a cell density proxy should give linear relationships between cell densities and overall reduction rates, however this proved not to be the case, with rates of oxygen reduction differing between cultures with the same optical density (data not shown). Therefore where possible, any normalisation that was carried out used the initial oxygen reduction rate as a relative indicator of living cells. Plating out serial dilutions of high density cultures showed that a culture with $OD_{600} = 1$ contains approximately 1×10^9 cells/ml.

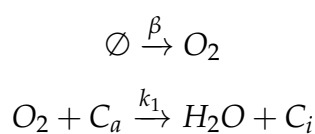
3.1.2 Converting Biological Reactions into Differential Equations

The rationale for obtaining the form for each of the 9 component equations is described below. Throughout the model the reduced components, i.e. those with available electrons, are denoted as active and have a subscript a . Components lacking a subscript denote the total, constant, amount of a component. \emptyset denotes nothing (this is used as the source or sink when substrates are entering or exiting the system).

3.1.2.1 Respiratory Substrates

Oxygen

The change in concentration of oxygen is affected by the following kinetic processes.



where β is the rate constant of passive diffusion (as a function of O_2 concentration) of O_2 into the electrode chamber. The rate constant k_1 describes the reduction of oxygen and the oxygen reductase cbb_3 ; this value depends on the concentration of reduced (i.e. active) cbb_3 , C_a and the concentration of O_2 . The differential equation that gives the change in oxygen concentration is

$$\frac{d[O_2]}{dt} = \beta(1 - [O_2]/K_O) - k_1[C_a][O_2] \quad (3.1)$$

In isolation the first term gives rise to a simple exponential input of oxygen until the saturation level (K_O) is reached to account for diffusion into the system. The rationale for the form of the equation is given below.

During the course of the experimental stages of this work, on occasions where the respiring cultures had died, either through being left in essentially anaerobic conditions for too long, or were treated with Chloramphenicol (which stops all protein production in the cell), the oxygen levels in the culture media would begin to rise slowly. This did not occur in every case, and after some further experimentation it was concluded that it probably occurs when an air bubble gets trapped underneath the lid of the oxygen electrode chamber. To try and abate the rate of diffusion in all subsequent experiments particular care was taken to avoid an air bubble being trapped in the electrode chamber.

Unfortunately even with no air bubble a small amount of oxygen was diffusing in, so an experiment was set up to try and quantify the rate of diffusion. Wild-type *N. meningitidis* cultures were grown to various different cell densities and left to respire aerobically. Once the cultures had used all the available oxygen they were killed either by adding a small volume of Chloramphenicol ($25\mu l$), or by heating the culture to $95^\circ C$ for 10 minutes. Oxygen concentrations were then recorded as the gas diffused back into the electrode chamber. It should be noted that Chloramphenicol should not actually kill the cells as it merely prevents further protein production in the cell, however the results of this experiment showed that under anaerobic conditions after addition of Chloramphenicol the cultures

are no longer capable of respiring oxygen.

The experimental data showed that the increasing oxygen concentration takes the form of an inverse exponential decay and therefore can be fit very easily to an exponential function. The exact parameters of the diffusion seem to differ between cultures but it appeared to have a dependence on the cell density whereby lower cell densities generally had higher rates of diffusion than higher cell densities, but there was no obvious direct relationship. The equation used to fit raw data for oxygen diffusion is a 3 parameter exponential:

$$f(x) = c - ae^{-bx}$$

In the differential equation this collapses to two parameters, the oxygen saturation level, and the rate of oxygen recovery thus:

$$\frac{d[O_2]}{dt} = \beta(1 - O_2/K_O)$$

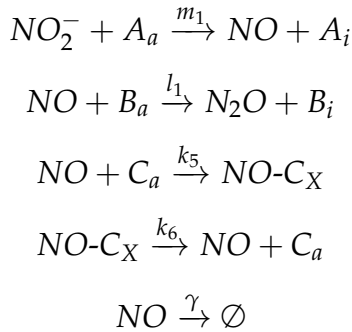
Integrating and separating this equation gives:

$$\begin{aligned} -\beta \frac{t}{K_O} + C &= \ln([O_2] - K_O) \\ \Rightarrow [O_2] - K_O &= Ae^{\left(-\beta \frac{t}{K_O}\right)} \\ \Rightarrow [O_2] &= K_O + Ae^{\left(-\beta \frac{t}{K_O}\right)} \end{aligned}$$

Nitric Oxide

The change in nitric oxide concentration is affected by the following kinetic pro-

cesses.



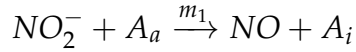
The equations above have a number of additional interactions in comparison to O₂. NO is created by the reduction of NO₂⁻ by AniA, is reduced by its dedicated reductase, NorB, and converted to N₂O which is lost from the cell, interacts with *cbb*₃, and is also spontaneously lost from the electrode chamber. It is assumed that the interaction with *cbb*₃ occurs only in a reversible manner, leading to an NO bound and temporarily inactive form C_X. There is evidence that this interaction can also lead to permanent degradation of *cbb*₃ via the formation of peroxy nitrite at the terminal oxidase. This is not currently considered in this version of the model. These effects are described mathematically in the equation below.

$$\frac{d[NO]}{dt} = m_1[NO_2^-][A_a] - l_1[NO][B_a] - k_5[C_a][NO] + k_6[C_X] - \gamma[NO] \quad (3.2)$$

The rate of synthesis of NO is captured by the first term, with rate constant *m*₁ and depends on the both the concentration of NO₂⁻ and reduced AniA (*A*_a). The reduction of NO is described by the next term with the rate constant *l*₁ and also depends on the concentration of NO and reduced NorB (*B*_a). Inhibition of *cbb*₃ by NO is modelled by the 3rd component of the equation. *k*₅ is the rate constant describing the reversible binding of NO to *cbb*₃ to form the inactive form of *cbb*₃, C_X. *k*₆ is the rate of recovery of this inhibited *cbb*₃. γ is the spontaneous rate of loss of NO from the electrode chamber.

Nitrite

The change in nitrite concentration is affected by the following kinetic process.



Which can be modelled mathematically by this equation

$$\frac{d[NO_2^-]}{dt} = -m_1[NO_2^-][A_a] \quad (3.3)$$

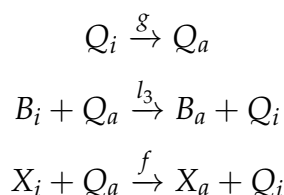
where m_1 is the rate constant for reduction of NO_2^- by reduced (active) AniA (A_a).

3.1.2.2 Electron Transporters

In addition to the rate of change of concentration of the respiratory substrates, the model also contains information about the upstream state of components of the transfer chain, starting from the quinone pool. The ultimate upstream source of electrons into the respiratory chain is from NADH, but for the sake of simplicity all processes prior to the quinone pool are subsumed into a simple single rate constant. This simplification is made to avoid further complications associated with varying metabolism and to avoid distraction from the stated primary aim of understanding the switching behaviour of the downstream chain. The quinone pool was chosen as the starting point because it is known that NorB draws electrons directly from this point and therefore this represents the first branch in the chain. The desire was to understand how competition for electrons at branches affects function and therefore the quinone pool is included in the model.

Quinones

The change in concentration of reduced quinones is affected by the following kinetic processes.



The differential equation that models these reactions is

$$\frac{d[Q_a]}{dt} = g([Q] - [Q_a]) - l_3[Q_a](B - B_a) - f[Q_a](X - X_a) \quad (3.4)$$

Q_a is the reduced quinone, and Q the total concentration of quinones in the system (Q_i is calculated from these two values). g represents the constant rate of availability of electrons into the quinone pool from NADH. The reduction of NorB by active quinones is parametrised by the rate constant l_3 . NorB and reduced NorB are given by B and B_a respectively. As the quinones also reduce the cytochromes, this also needs to be modelled. f is the rate constant parametrising the reduction of cytochromes by the active quinones. Total cytochromes and total reduced cytochromes are given by X and X_a respectively which are used to calculate X_i in the kinetic process.

Cytochromes

A simplified version of cytochromes was used and therefore X actually represents a pool of different cytochromes, c_x , c_4 , c_5 and the bc_1 complex. These are amalgamated into one here to simplify the equations and focus on the simple branching of the chain and competition for electrons. This is a modelling choice and it is further discussed in Chapter 9.

The concentration of active cytochrome pool changes due to both reduction by the upstream quinone pool and oxidation by both of the remaining downstream terminal enzymes can be seen in the following kinetic processes.



These are modelled with the following differential equation

$$\frac{d[X_a]}{dt} = -k_3([C] - [C_a] - [C_X])[X_a] - m_3([A] - [A_a])[X_a] + f[Q_a]([X] - [X_a]) \quad (3.5)$$

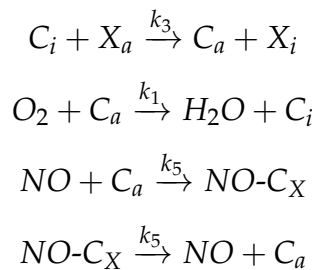
where k_3 is the rate constant describing the reduction of the available oxidised cytochrome c oxygen reductase (cbb_3) by the quinone pool (via c_x & c_4). C , C_a and C_X represent the overall concentration of cbb_3 , reduced (active) cbb_3 and NO inhibited cbb_3 respectively. m_3 is the rate constant describing the reduction of AniA by the cytochrome pool (via c_5). The concentration of active cytochromes is thus increased by their reduction by the quinone pool, but this in turn can reduce the flux from the pool because less oxidised cytochrome is available to accept electrons. As stated previously, the relative time scales are unknown so all processes appear explicitly.

3.1.2.3 Terminal Reductases

Finally the changes in concentration of reduced terminal oxidases, cbb_3 , AniA and NorB are described by the following equations. All the terms present in this section have been introduced previously. These equations of course could equally have been written for the oxidised form but these can easily be recovered because it is assumed that the total concentration of the oxidases remains constant.

Reduced cbb_3

The kinetic processes which affect the concentration of reduced (active) cbb_3 are



which is described by

$$\frac{d[C_a]}{dt} = k_3([C] - [C_a] - [C_X])[X_a] - k_1[C_a][O_2] - k_5[C_a][NO] + k_6[C_X] \quad (3.6)$$

Inhibited *cbb*₃

The following kinetic process alters the concentrations of reversibly inhibited *cbb*₃.

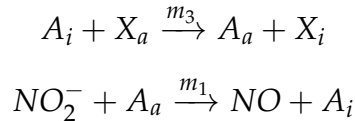


which is described by

$$\frac{d[C_X]}{dt} = k_5[C_a][NO] - k_6[C_X] \quad (3.7)$$

Reduced AniA

The concentration of reduced AniA is affected by the following kinetic processes.



which can be modelled by

$$\frac{d[A_a]}{dt} = m_3([A] - [A_a])[X_a] - m_1[NO_2^-][A_a] \quad (3.8)$$

Reduced NorB

Changes in NorB concentration occur via the following kinetic processes.



and are modelled by this equation

$$\frac{d[B_a]}{dt} = l_3[Q_a]([B] - [B_a]) - l_1[NO][B_a] \quad (3.9)$$

3.1.3 Assumptions and their Justifications

A number of assumptions were made regarding the kinetics and reactions taking place in the model.

1. **It is assumed that NO inhibits the reduced cbb_3 and not the oxidised form, since it is not expected that Nitric oxide to bind to an inactive enzyme.** This is corroborated by Giuffre et al.⁹², who show significant levels of inhibition of reduced cytochrome. They do also however observe low levels of inhibition of the oxidised enzyme also. Their experiments used cytochrome c oxidase (aa3) rather than cbb_3 , but I believe this assumption still stands as the enzymes are of the same family. This also implies that the model deals exclusively with reversible inhibition.
2. **Bacterial population structure and concentration variation not considered.** The primary substrates of interest are gases and substrates which are thought to freely diffuse in and out of the cells. Additionally the culture is kept well-mixed at all times, thus it can be assumed that the culture is homogeneous.
3. **No backwards reactions.** For simplicity, backwards reactions are not included. However they may be important, and could easily be included in a future study with the concomitant increase in parameter count.
4. **No Michaelis-Menten kinetics.** Separation of time-scales cannot be assumed as the rates of intermediate reaction steps are not known. Future information regarding time-scale separation could easily be incorporated.
5. **All cytochromes can be modelled as one.** The main effort of modelling was to concentrate on the position of branches in the respiratory chain. In the same way the effects of Laz and c_5 on AniA and cbb_3 respectively can also be ignored. They are not the prime electron donors to their terminal reductases and contribute very little overall to the reduction²³.

3.2 Parameters and their Prior Distributions

None of the rate constants or concentrations which were required for this model have previously been determined for *Neisseria meningitidis*, so values from other similar organisms had to be used instead. In some cases there appears to be no data in the literature regarding values of particular components. Table 3.1 lists the values that have been obtained from the literature.

Variables

O₂ - Oxygen concentration

This variable is always obtained directly from the experimental dataset as it indicates the starting point for oxygen in the model. It is calculated from a linear regression analysis of the first section of oxygen reduction to eliminate noise in the data.

NO - Nitric oxide concentration, and NO₂⁻ - Nitrite concentration

As for Oxygen concentration, these variable is simply obtained from the dataset and the same conditions apply.

X_a, A_a, B_a, C_a, Q_a - Reduced enzyme concentrations, and C_X - Reversibly NO inhibited *cbb*₃

These values are unknown at start of simulations. They have to be lower than the total concentrations for each enzyme, and the model enforces this. Given the rates of reduction of these enzymes they are all set to very low values, determined from exploratory runs of the parameter estimation algorithm. The rates of reduction for these enzymes actually make the initial value (so long as it is low) largely irrelevant as they reach their steady-state after only a few integration cycles.

Symbol	Description	Value	Source
k_1	Rate constant for O_2 reduction by reduced cbb_3	$415 \mu M^{-1}s^{-1}$	Forte et al. ⁹³ and Hunter ⁹⁴
k_3	Rate constant for cbb_3 reduction by cytochrome pool	$3 \mu M^{-1}s^{-1}$	Chang et al. ⁵⁷
l_1	Rate constant for NO reduction by reduced NorB	Unknown	N/A
l_3	Rate constant for NorB reduction by quinone pool	Unknown	N/A
m_1	Rate constant for NO_2^- reduction by reduced AniA	Unknown	N/A
m_3	Rate constant for AniA reduction by cytochrome pool	$4.8 \pm 0.2 \mu M^{-1}s^{-1}$	Nojiri et al. ⁹⁵
k_5	Rate constant for cbb_3 inhibition by NO	$100 \mu M^{-1}s^{-1}$	Giuffre et al. ⁹² and Blackmore et al. ⁹⁶
k_6	Rate constant for recovery of NO inhibited cbb_3	$38 s^{-1}$	Rock et al. ¹⁸
β	Rate constant for passive diffusion in of O_2	Unknown	N/A
K_O	Saturation O_2 level	$48 \mu M$	This work
g	Rate of electrons in from NADH	$0.8 s^{-1}$	This work
f	Rate constant for reduction of cytochromes by quinones	$8 \mu M^{-1}s^{-1}$	This work
γ	Spontaneous loss of NO	Unknown	N/A
Q	Concentration of quinones	$0.3 \mu M$	Hedrick and White ⁹⁷
X	Concentration of cytochromes	$\approx 3.97 \mu M$	Deeudom ²³
A	Concentration of AniA	$0.003 - 0.03 \mu M$	This work
B	Concentration of NorB	$0.003 - 0.03 \mu M$	This work
C	Concentration of cbb_3	$0.003 - 0.03 \mu M$	This work

Table 3.1: **Model parameters.** This table shows all the parameter values that have been obtained from the extant literature, or interpolated from preliminary experiments done during the course of this work. These values represent the initial data that is used to populate the model, from which all subsequent parameter sets are generated. For values that show concentrations of components, they represent the value for a culture with $OD_{600} = 1.00$.

Parameters

k₁ - Rate constant for O₂ reduction by reduced cbb₃

A value for k_1 , the constant for O₂ reduction by reduced *cbb₃* was calculated by using the K_{cat} value from *Pseudomonas stutzeri*, and the k_m value from *Neisseria lactamica*, which Forte et al.⁹³ and Hunter⁹⁴ determine are 166 s⁻¹ and 0.4 μM respectively. k_1 can be calculated as $\frac{166\text{ s}^{-1}}{0.4\text{ }\mu\text{M}} = 415\text{ }\mu\text{M}^{-1}\text{s}^{-1}$.

k₃ - Rate constant for cbb₃ reduction by cytochrome pool

k_3 , the rate constant for reduction of *cbb₃* by the cytochromes was calculated from values obtained from the maximum reduction rate of *cbb₃* by cytochrome *c₄* in *Vibrio cholerae* by Chang et al.⁵⁷. A rate of 300 electrons transported per second was observed with a cytochrome *c₄* concentration of 100 μM. This concentration was not saturating, but there appears to be a linear relationship between rate and concentration. We assume that 1 electron equals 1 reduction of *cbb₃*, thus the rate constant for reduction of *cbb₃* by cytochromes is $\frac{300\text{ s}^{-1}}{100\text{ }\mu\text{M}} = 3\text{ }\mu\text{M}^{-1}\text{s}^{-1}$.

l₁ - Rate constant for NO reduction by reduced NorB

An estimate for the rate constant for NO reduction by reduced NorB can be obtained from Rock et al.³⁰. They observed rates of NO reduction of $54 \pm 6\text{ nmol min}^{-1}\text{mg}^{-1}$. This was in total protein content from dry weight. Thus the rate of NO reduction is $0.9 \pm 0.1\text{ }\mu\text{mols}^{-1}\text{g}^{-1}$ bacterial protein. The protein content of the cells was assumed to be similar to that of *E. coli* at 50% of dry weight, where each cell weighed 2 pg. A culture of *Neisseria meningitidis* with OD₆₀₀ = 1 has 1×10^9 cells/ml, therefore the rate is 4.5 nmols⁻¹ of quinones in 5 ml culture ($5 \times 10^9\text{ cells} \times 2 \times 10^{-12}\text{ g} \times 50\% \times 0.9\text{ }\mu\text{mols}^{-1}\text{g}^{-1}$), converted to molarity is 0.9 μMs⁻¹.

l₃ - Rate constant for NorB reduction by quinone pool

No information available in the literature, so the rate constant is set to 1 μM⁻¹s⁻¹.

m₁ - Rate constant for NO₂⁻ reduction by reduced AniA**m₃ - Rate constant for AniA reduction by cytochrome pool**

The value for m_3 , the rate constant for reduction of AniA by cytochromes, is the observed electron transfer rate between the equivalent cytochrome and nitrite reductase from *Achromobacter xylosoxidans*. A value of $4.8 \pm 0.2 \mu M^{-1}s^{-1}$ was observed during stopped-flow experiments by Nojiri et al.⁹⁵.

k₅ - Rate constant for cbb₃ inhibition by NO

Giuffre et al.⁹² and Blackmore et al.⁹⁶ showed with cytochrome *c* oxidase that NO could bind reversibly and inhibit the activity of the enzyme. The rate constant they calculated was $10^8 M^{-1}s^{-1}$. I assume that even though the enzyme is different, its NO binding characteristics would be similar to that of *cbb₃* as it is of the same family.

k₆ - Rate constant for recovery of NO inhibited cbb₃

Giuffre et al.⁹² calculated a half-life of $t_{1/2} \approx 80$ min, however without any concrete values for concentration of $C_X\text{-NO}$ this can't be used to calculate a rate constant. Rock et al.¹⁸ observed the apparent K_i and calculated it to be 380 nM at 50 μM O₂. Since $K_i = \frac{k_6}{k_5}$, a value for k_6 can be estimated as $k_6 = K_i \times k_5 = 0.38 \mu M \times 100 \mu M^{-1}s^{-1} = 38 s^{-1}$.

 β - Rate constant for passive diffusion in of O₂, and K_O - Saturation O₂ level

The parameters obtained from fitting oxygen diffusion data showed a small difference in K_O between cell densities, thus $K_O = 48 \mu M$ we selected as the standard value for this parameter. β differed more between the experiments thus in the parameter estimation system is not fixed and allowed to be modified freely. An example of the experimentally observed diffusion rates are shown in Figure 3.1.

Oxygen Diffusion Rates



Figure 3.1: Oxygen Diffusion Rates. This figure shows experimentally observed rates of oxygen diffusion back into the electrode chamber. An exponential decay function has been fitted to the green dataset and produces the K_O value of $\approx 48 \mu M$.

g - Rate of electrons in from NADH (or rate of reduction of quinones)

This value is unknown, but initial runs of the algorithm suggest the value to be about $0.8 s^{-1}$.

f - Rate constant for reduction of cytochromes by quinones

Snyder et al.⁵² showed by reducing yeast cytochrome bc₁ by using 25 μM mena-quinol the rate constants were $7.9 s^{-1}$ for cytochrome b, and $1.55 - 6.9 \times 10^5 M^{-1}s^{-1}$ for cytochrome c₁ (second order). However preliminary tests showed that a value of $8 \mu M^{-1}s^{-1}$ was more appropriate.

γ - Spontaneous loss of NO

This value is assumed to be the same as the β , the rate constant for oxygen diffusion in across the liquid-gas barrier, as this is simply the reverse.

Q - Concentration of quinones

Q , the concentration of quinones was calculated based on data from Hedrick and White⁹⁷. The protein content of the cells was assumed to be similar to that of *E. coli* at 15% of wet weight, where each cell weighed 2 pg, and that there were 1 μmol of respiratory quinones per g of bacterial protein. A culture of *Neisseria meningitidis* with $OD_{600} = 1$ has 1×10^9 cells/ml, therefore there are 1.5 nmol of quinones in 5 ml culture (5×10^9 cells $\times 2 \times 10^{-12}$ g $\times 15\% \times 1 \mu\text{mol/g}$), converted to molarity is 0.3 μM .

X - Concentration of cytochromes

Deedom²³ suggests that the total cytochrome concentration (inc. cbb_3) is about 4 μM in *Neisseria meningitidis*. Thus subtracting the value for C leaves a concentration of $\approx 3.97 \mu\text{M}$.

A, B, C - Concentration of Respiratory enzymes

Given the lack of concrete values for these parameters, the assumption is that all the respiratory enzymes are present in roughly equal quantities. Based on the values given for Q above, there are 1.5 mg of cell protein in 5 ml of $OD_{600} = 1$ culture. cbb_3 is thought to be about 0.1-1% of the total cell protein and is approximately 100 kDa in molecular weight. Therefore converting these values to molarity gives a concentration of approximately 3-30 nM.

3.3 Solving Ordinary Differential Equations

The model equations (given previously) are solved in parallel using the common 6th order Runge-Kutta-Fehlberg algorithm for integrating ordinary differ-

ential equations⁹⁸. Adaptive step-sizes were implemented using the Cash-Karp method⁹⁹. The adaptive step size system was required as it prevented the introduction of systemic numerical instabilities (see appendix for further details of why this was necessary).

3.4 Implementation of the Model in Software

The parameter estimation system and ODE solver were a bespoke implementation written in Java. The Runge-Kutta algorithm was modified from that found in Numerical Recipes in C¹⁰⁰. I decided to write a custom implementation rather than using off the shelf systems for solving ODEs and parameter estimation as I wanted the greatest flexibility in how I integrated the two techniques, and it allowed me to quickly and easily tailor the code to my needs. Initially I tried using COPASI⁷⁹, however at that time it had limitations that could not be overcome, such as an inability to allow bulk addition of components at arbitrary time-points.

The implementation of the model has no constraints on respiratory substrate concentration, thus allows the altering of these concentrations whilst solving the equations. This ability means that the switch between aerobic and anaerobic respiration can be examined synthetically, and the model is also capable of simulating how the respiratory system responds to the sudden addition of substrates such as Nitric Oxide. More complicated methods are possible, but given the high diffusion of the substrates concerned as well as the deliberate injection of the relevant substrate this method was a simpler and reasonable mimic for my empirical method. This ability was an absolute requirement, as in order to fully parametrise the model it was necessary to isolate sections of the model, which required adding aliquots of respiratory substrate during respiration.

3.5 Parameter Estimation

Estimating the parameter values for the components in the mathematical model involved comparing the biological results with those produced by solving the

ODEs and adjusting the parameter values to minimise the difference between the two results. The different methods for parameter estimation that were investigated are detailed in Chapter 4 [Parameter Estimation Methodologies].

Chapter 4

Parameter Estimation Methodologies

Below are the various different methods for parameter estimation that were investigated during the course of this work. All of these methods involve a sampling system that attempts to select parameter values which minimise the difference between the simulation result and the experimental data by calculating a likelihood. The aim of the parameter estimation methodology was to get this likelihood as close to zero (perfect fit/no difference) as possible. Two different calculations were used to create the likelihood. One was the sum of the Least Squares Differences between the measured components in the experimental data and the simulation result. This was used in early parameter estimation runs.

$$f = \sum_{j=1}^n \left(\sqrt{\sum_{i=1}^m (\Delta x_{ij})^2} \right) \quad (4.1)$$

The second method for calculating the likelihood was a normal correlation which allowed greater tuning, as the standard deviation of the distribution could be set to adjust how much fitter the simulation result needed to be to be accepted.

$$f = \sum_{j=1}^n \left(\sum_{i=1}^m \left(\ln \left(\frac{1}{2\pi\sigma_j^2} e^{-\frac{(0-0)^2}{2\sigma_j^2}} \right) - \ln \left(\frac{1}{2\pi\sigma_j^2} e^{-\frac{(x_{ijFIT} - x_{ijDATA})^2}{2\sigma_j^2}} \right) \right) \right) \quad (4.2)$$

In most cases the components used for calculating the likelihood are Oxygen and Nitric Oxide, as these were the primary measured chemicals.

The main difference between the parameter estimation methodologies laid out below are the ways in which they generate new parameter values, either from a probability distribution or based on the previous value, and the way this is applied and tested against the experimental data.

Monte Carlo Methods

A brief section is included here to describe Monte Carlo Methods, as the techniques used for parameter estimation all use this method as their estimator in some form. “Monte Carlo Methods” is a generalised term to describe a stochastic technique that makes use of random numbers to examine a problem in conjunction with probability statistics. Monte Carlo Methods allow us to model complex systems without having to exhaustively search every possible outcome. Large systems are sampled in random configurations and that data applied in such a way that it can be used to describe the system as a whole. “Monte Carlo techniques are often the only practical way to evaluate difficult integrals or to sample random variables governed by complicated probability density functions”¹⁰¹.

4.1 Simulated Annealing

This technique was described independently by Kirkpatrick et al.¹⁰² and Černý¹⁰³. The name comes from the metallurgical annealing process whereby large crystals are formed while a material is slowly cooled. The slow cooling increases the probability of individual crystals obtaining lower energy states than the initial. As the material cools the “distance” each crystal can move along the energy landscape decreases. Simulated annealing “consists of a discrete-time inhomogeneous Markov chain”¹⁰⁴ whereby the previous state is modified with a perturbation kernel (the neighbouring states) and then accepted or rejected using a transition probability which depends on the current temperature and the ener-

```
c1 <- c0;
c2 <- mutate(c1);
i <- 0;
while i < i_max
  if fitness(c1) > fitness(c2)
    c2 <- mutate(c1)
  else
    c1 <- mutate(c2)
  i <- i + 1
if fitness(c1) > fitness(c2)
  return c1
else
  return c2
```

Figure 4.1: Pseudo-code showing how the simplest annealing algorithm works.

gies of the previous and current states. The advantage of this scheme is that areas of local minima have a lesser effect on the outcome of the Markov chain as the high initial temperature allows for the chain to “jump” out of this minima.

Figure 4.1 contains some simple pseudo-code which shows how the basic algorithm works (without the annealing temperature). This will provide a “best” parameter set, but there is no information about the possible spread of values in the parameter set. Given that it is unlikely that a single point-value parameter-set solution exists that will accurately describe the system it is necessary to produce a spread of results that will adequately describe the system instead. To this end a modified version of simulated annealing was used integrated with aspects of a simple genetic algorithm. In the genetic algorithm paradigm a synthetic “chromosome” is created containing which contains “genes” representing the parameters in the simulation. These include the rate constants, concentrations of various components and initial concentrations of substrates and products. This chromosome is then copied and perturbed several times (depending on the eventual population size required), with the size of the perturbation being dependent on the current annealing temperature. For instance the highest temperature could indicate that the individual parameters can be perturbed by up to $\pm 10\%$, and as the temperature decreases the perturbation percentage has a concomitant decrease. An example annealing temperature schedule is shown in



Figure 4.2: **Example simulated annealing temperature schedule.** This represents how the annealing temperature changes as the annealing process progresses. Temperature is denoted by the y-axis value, and simulation progress by the x-axis value. This is a heavily compressed time-frame, as in reality the system would normally process 10,000 sets of parameters at each annealing temperature.

Figure 4.2. The annealing temperature is programmed to decrease after a defined number of iterations such that the magnitude of individual mutations becomes smaller as the simulation progresses. This should have the effect of honing in on a set of parameters with a better likelihood. Once the chromosome population has been created, 2 are selected at random and their likelihoods evaluated, in this case by the Least Squares Difference method. The chromosome with the lowest likelihood is discarded and the other is cloned and perturbed. The two chromosomes are then added back to the chromosome population. The genetic algorithm is used to improve the parameters sets by perturbing genes (individual parameters) from fit chromosomes (complete parameter sets), re-running the simulation and discarding unfit parameter sets. An unfit parameter set is defined as one with an likelihood lower than the highest so far. This technique involves having two chromosomes selected at any one time. The parameters from each



Figure 4.3: Schematic diagram showing the technique used to generate a spread of parameters using a synthetic chromosome. The parameters are loaded as genes on the chromosome which are then perturbed, 2 chosen and the fittest kept and perturbed. Each time a chromosome is perturbed it is reintroduced into the chromosome pool, and the next 2 chromosomes are chosen at random.

chromosome are simulated and the least fit one is discarded. At this point the contents from the fitter chromosome are cloned and perturbed, and the cycle is repeated. Figure 4.3 shows this diagrammatically. After many cycles (upwards of 1000) the chromosome pool should only contain the best fitting parameter sets to the experimental data. The spread of the parameters can be used to infer the sensitivity of the simulation to changes in parameter values in a similar way to that described by Toni et al.¹⁰⁵.

This algorithm was rejected as unsuitable as it seemed to be incapable of settling on solutions to the Nitric Oxide reduction datasets during testing. Additionally this technique doesn't produce probability distributions which were eventually required to incorporate data from previous datasets.

4.2 Approximate Bayesian Computation by Sequential Monte Carlo

“Approximate Bayesian Computation methods have been conceived with the aim of inferring posterior distributions where likelihood functions are computationally intractable or too costly to evaluate. They exploit the computational efficiency of modern simulation techniques by replacing calculation of the likelihood with a comparison between the observed data and simulated data”¹⁰⁵.

To incrementally improve the parameter sets, a version of Bayesian inference is used in conjunction with a standard Monte Carlo method in a system called Approximate Bayesian Computation by Sequential Monte Carlo (ABCSCMC) as described by Toni et al.¹⁰⁵. An implementation of algorithm (S) was used from that paper.

Bayesian Inference - This a statistical method for inferring the probability of a hypothesis based on available evidence. As more evidence is accumulated, the inference is updated and the probability of the hypothesis being true is changed. Given enough evidence, the probability of the hypothesis being true should either be very high or very low causing you to either accept or reject the hypothesis. Bayesian inference relies on having a prior probability (or probability distribution) for the hypothesis, and this can inevitably introduce a level of bias into the inference. Bayesian inference can be described thus:

$$P(H | E) = \frac{P(E | H)}{P(E)} \cdot P(H) \quad (4.3)$$

- $P(H | E)$ is the posterior distribution of H given E .
- $P(H)$ is the prior distribution
- $\frac{P(E | H)}{P(E)}$ is the impact of E on the degree of belief in H .

A simplistic example of using Bayesian inference to alter a hypothesis could happen in the case of having two jars of sweets. Jar 1 has 15 strawberry sweets and 25 raspberry sweets. Jar 2 has 20 of each. Supposing a third party selects 1

sweet at random from 1 of the jars. They select a strawberry sweet, what is the probability that it came from Jar 1? From the point of view of our third party both jars are identical, therefore $P(H_1) = P(H_2)$ and the total probability must equal 1, so the prior probability of each jar is 0.5. The observation, E is of a strawberry sweet, which we can then use to calculate the likelihood of it being from each jar individually by $P(E | H_1) = 15/40 = 0.375$ and $P(E | H_2) = 20/40 = 0.5$. Bayes formula can then be used to work out the probability of the strawberry sweet being from jar 1, that is $P(H_1 | E)$.

$$\begin{aligned}
 P(H_1 | E) &= \frac{P(E | H_1)P(H_1)}{P(E | H_1)P(H_1) + P(E | H_2)P(H_2)} \\
 &= \frac{0.375 \times 0.5}{0.375 \times 0.5 + 0.5 \times 0.5} \\
 &= 0.429
 \end{aligned} \tag{4.4}$$

Before the observation of the sweet, the probability of the third party taking from jar 1 was the prior probability of 0.5. After the observation this probability must be revised to 0.429.

Bayesian inference is widely used in computational analysis for artificial intelligence and email spam identification. It is also used in the field of population genetics and phylogenetics¹⁰⁶.

Approximate Bayesian Computation - This is an adaptation of Bayesian inference which allows approximately the same inferences to be made, with considerably less computation. It operates on representations of the datasets rather than the datasets themselves. Common examples are population mean and variance. This is useful for large complex datasets where the probability of a simulation of the dataset matching the original is very small (unacceptably so), in this case a representation of the datasets can be used, and the difference calculated.

If the difference is less than a pre-defined acceptance threshold, then the simulated dataset is accepted. ABC originally came from the fields of population and evolutionary genetics¹⁰⁷, but are now being applied to complex and stochastic dynamical systems^{105,108,109}.

ABC differs from standard Bayesian inference shown in Equation 4.3 in that the likelihood term does not need to be calculated. Instead the difference between the summary statistics of the observed data and the simulated data is used. The simulated data is considered a true sample from the posterior distribution if the difference in summary statistics is less than a predefined acceptance threshold.

The most basic ABC methods takes the following form:

θ is a parameter vector to be estimated, $\pi(\theta)$ is the prior probability distribution, and x is the observed data. The posterior distribution is $\pi(\theta | x) \propto f(x | \theta) \cdot \pi(\theta)$.

1. Create a candidate parameter vector θ^* from the prior distribution $\pi(\theta)$.
2. Simulate dataset x^* using the model and parameter vector θ^* .
3. Compare x^* with x using a distance function d and an acceptance criteria ϵ .
If $d(x, x^*) \leq \epsilon$, accept θ .

Given a low enough value for ϵ , the output distribution should approximate the true posterior distribution if sampled a large enough number of times.

Sequential Monte Carlo - This is a method of particle filtering whereby a large set of samples (N) are drawn from the prior distribution, and for each sample, the probability is calculated. Weights for each particle are assigned based on the probabilities, and these affect how likely a particle is to be selected in subsequent rounds of selection. At the end of each round, the posterior distribution, that of the N particles becomes the prior distribution for the next round.

Approximate Bayesian Computation by Sequential Monte Carlo - This combines the previous two methods by drawing a large number of particles from the prior distribution using Bayesian inference. The prior distribution is discrete in the scheme used here, so a perturbation kernel based on a Laplacian or Gaus-

sian distribution is used on each sample to provide small deviations to better approximate a continuous prior distribution. Each sample is simulated and only accepted if it exceeds the acceptance threshold. This is calculated based on the least-squares difference (LSD) between the simulated data and the original dataset. If a sample is rejected, a new one is drawn from the prior distribution and SMC then continues as described above. The weights of the accepted samples are calculated based on the probabilities of being selected from the prior and the samples go on to form the posterior distribution. For each subsequent round, the mean LSD of the posterior distribution from the previous round is used as the acceptance threshold. This ensures that each round results in better fitting parameter sets. The cycle is then repeated until a pre-defined cycle limit is reached¹⁰⁵.

A significant advantage of this technique is that it is readily parallelisable, as each particle in the SMC process is independent, thus can be simulated in parallel. A parallel version of this algorithm was implemented in the JAVA programming language which resulted in significant speed-ups when multiple processing threads can be used. The threading manager means that the algorithm is theoretically most efficient (in terms of computational time) when the number of particles is an exact multiple of the number of processing threads. In practice however this is negated by the fact that some particles require multiple samples due to them not meeting the acceptance criteria.

This algorithm was rejected on the grounds that it seemed incapable of settling on sensible posterior distributions with some datasets. It is suspected that the distance function used was causing a conflict which meant the algorithm was accepting bad parameter sets and rejecting good ones. The requirement of a suitable distance function or summary statistic is a major disadvantage of this algorithm.

4.3 Metropolis Hastings Monte Carlo

The Metropolis-Hastings algorithm is Markov Chain Monte Carlo method to retrieve sequences of random samples from a probability distribution which cannot be sampled directly (or would be very difficult) such as when no probability distribution function exists. The algorithm was originally developed by Metropolis et al.¹¹⁰ for generating samples from the Boltzmann distribution. It was later extended to a more general form for any distribution by Hastings¹¹¹.

MHMC allows each individual parameter to follow a biased random walk until it reaches a point of maximum likelihood. The typical output of this algorithm is a set of parameter trajectories (Markov Chains) which begin with a “burn in” period, followed by a parameter distribution. The “burn in” period contains data that is discarded, as it does not form part of the target distribution. The length of this burn in period often varies depending on how far the starting samples are from the target distribution. The parameter distribution can be calculated from the data that is left after the burn in period. This is done by a simple statistical analysis of the resulting data points. Since the distributions cannot easily be described as functions, the data are transformed into histograms with a set bin width. These histograms can be read and used a priors for subsequent runs of the MHMC algorithm.

The MHMC algorithm has been validated initially by using a much simpler ODE system than is required by the respiration model. A Lotka-Volterra system was used as this can be solved much more quickly by virtue of having far fewer parameters (4 as opposed to >20). The Lotka-Volterra system describes a simple predator-prey relationship and only requires two first-order, non-linear differential equations, which are shown in equation 4.5.

$$\begin{aligned}\frac{dx}{dt} &= x(\alpha - \beta y) \\ \frac{dy}{dt} &= -y(\gamma - \delta x)\end{aligned}\tag{4.5}$$

Validation of using this system required a simulated dataset with known parameter values to be produced. This dataset then forms the input for the MHMC algorithm which will try and obtain those same parameter values. Given the simplicity of this system, a particularly bad set of initial parameter estimates was given to exaggerate the burn in period, and to show that given a long enough time the simulation will eventually settle on “correct” values. This validation step also informs the likely values for two tuning variables in the algorithm; the *acceptance* - how stringent the algorithm is on accepting new parameter sets, and the *sigma* value - this describes the magnitude of parameter perturbation at each iteration. The graphical results of the Lotka-Volterra validation are shown in Figures 4.4 and 4.5.

4.4 Implementation

The initial parameters used to solve the equations were a set of priors based on preliminary experimental results. These parameters only provide a starting point as the second stage of computation involves modifying the parameters in order to provide a better fit against experimental data. To incrementally improve the parameter sets, a version of Bayesian inference is used in conjunction with a standard Metropolis-Hastings Monte-Carlo method.

Bayesian inference was used to inform the simulation parameters for a particular dataset based on prior probability distributions. These distributions were obtained as output from a previous dataset. This was integrated this with a Metropolis-Hastings algorithm for sampling the prior probability distributions. Each parameter was sampled, and the parameter set was used to solve the ODE



Figure 4.4: Simulation results of the Lotka-Volterra validation run.

Lotka-Volterra parameter search by Metropolis-Hastings

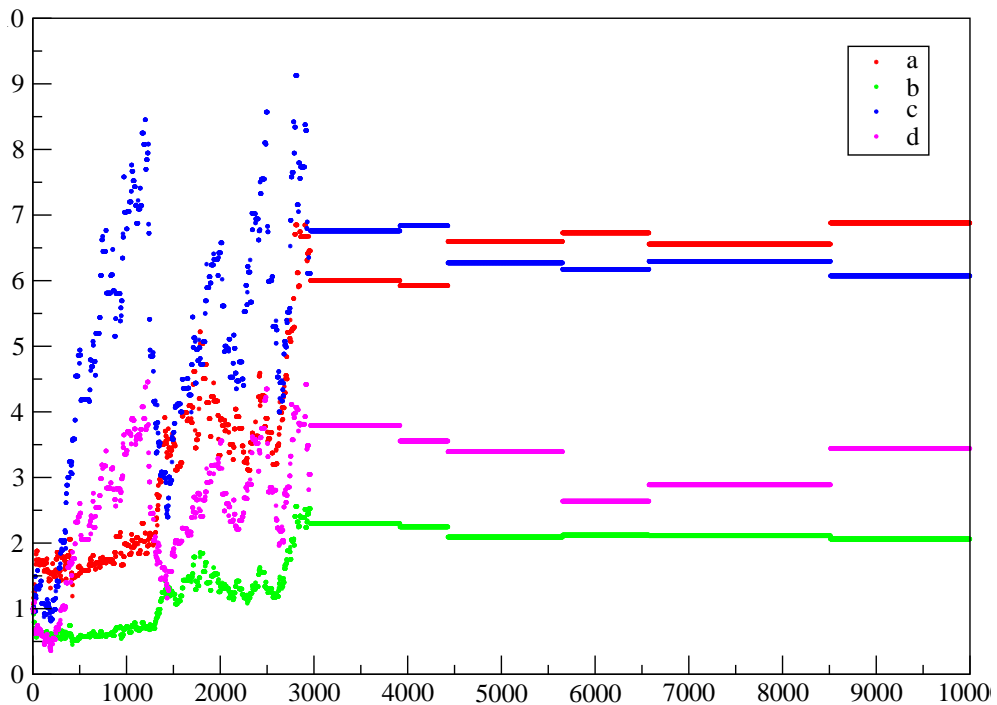


Figure 4.5: MHMC results of the Lotka-Volterra validation run. Note the initial burn-in period followed by the distribution trajectory.

model. Based on the likelihood of the solved model, the Metropolis-Hastings algorithm allows parameters to be modified in a biased random walk which ultimately leads them to their most fit state, calculated using Normal likelihood.

This algorithm was accepted as suitable since it seems to settle on reasonable solutions to the experimental datasets and produces usable posterior probability distributions for each of the parameters being estimated.

4.5 Integrative Scheme

Currently copied verbatim from paper

In order for us to iteratively generate a parameter set we needed to separate the model into simpler units whereby we can obtain data about a specific set of variables. We did this so that the simplest part of the model was parametrised first. In this case it was oxygen respiration, which only requires one enzyme (although it does still require the ETC). This section of the model also has the simplest experimental dataset. After parametrisation, a new section of the model was introduced, with its associated experimental dataset.

Experimental data was gathered for the first dataset, and this is used as a training set, with almost flat priors based on preliminary experimental data. The data was pre-processed and normalised if necessary and then presented to the Bayesian Parameter Estimation system. The MHMC algorithm samples from the prior distribution and then uses those samples as parameters to solve the model. It aims to improve the calculated likelihood and is ordinarily run for at least 10,000 iterations to give the system time to settle on the fittest parameters. The system is run on the same dataset 10 times to generate statistically significant results. The eventual output of the MHMC runs are posterior probability distributions for each of the parameters in the model. In accordance with Bayesian inference these are then used as prior distributions.

At this point the next section of the model to be parametrised is decided, the appropriate experimental data identified and obtained, and the process is re-

peated until the entire model has been populated. The final result should be a set of reasonably narrow probability distributions for each of the parameters which describe the system accurately enough to correctly predict the behaviour of the system *in vivo*.

Chapter 5

Oxygen Reduction in *N. meningitidis*

5.1 Aerobic Reduction of Oxygen

5.1.1 Introduction

The first dataset used in the iterative approach to parameter estimation was of a simple oxygen reduction experiment carried out in aerobic conditions. This dataset is the simplest biologically as under aerobic conditions and without the presence of any microaerobic substrates (nitrite or nitric oxide) the only respiratory pathway that is active is the oxygen reducing one. Additionally, the other parts of a respiratory chain influence the oxygen reducing pathway either by competing for electrons, or chemically inhibiting it. The relevant portions of the ETC are shown graphically in Figure 5.1.

The equations that describe this portion of the ETC are:

$$\begin{aligned}\frac{d[O_2]}{dt} &= \beta(1 - [O_2]/K_O) - k_1[C_a][O_2] \\ \frac{d[Q_a]}{dt} &= g([Q] - [Q_a]) - l_3[Q_a]([B] - [B_a]) - f[Q_a]([X] - [X_a]) \\ \frac{d[X_a]}{dt} &= -k_3([C] - [C_a] - [C_X])[X_a] - m_3([A] - [A_a])[X_a] + f[Q_a]([X] - [X_a]) \\ \frac{d[C_a]}{dt} &= k_3([C] - [C_a] - [C_X])[X_a] - k_1[C_a][O_2] - k_5[C_a][NO] + k_6[C_X]\end{aligned}$$

These equations describe the change in concentration of oxygen over time, which



Figure 5.1: **Oxygen reducing electron transport chain of *N. meningitidis*.** This shows the complete electron transport chain of *Neisseria meningitidis* with the components irrelevant to oxygen reduction greyed out. In the mathematical model all of the purple elements (cytochromes) are amalgamated into one entity.

is the experimentally observable value, the reduction state of the quinone pool and the reduction state of the cytochrome “pool”. This portion of the model involved 13 parameters and variables which were to be estimated (the model actually contains 17 such parameters and variables, but under these conditions the remaining 4 are set to 0 as they are related to nitrite reduction effects). This large number of parameters will clearly result in over-fitting, however this was necessary to generate loose bounds for all of the parameters.

5.1.2 Experimental Results

Generation of oxygen reduction datasets required the growth of MC58 (wild-type *Neisseria meningitidis*) in aerobic conditions until mid log-phase growth had been achieved. This corresponds to an OD₆₀₀ of 0.3-0.9 and usually required an incubation period of roughly 3 hours. Once the required cell density had been obtained, the culture was transferred to the oxygen electrode chamber and recorded the oxygen concentration as the culture respiration. At this point the cells are only

Aerobic Oxygen Reduction in *Neisseria meningitidis*

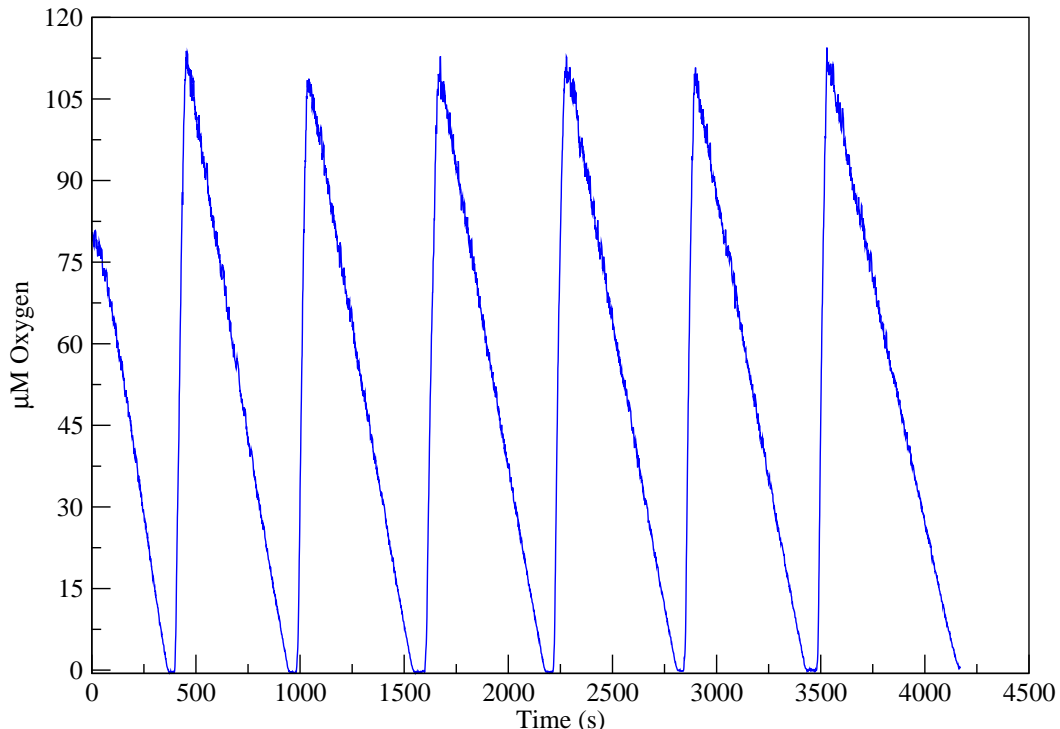


Figure 5.2: **Highly repeatable oxygen reduction.** This shows an oxygen reducing culture being repeatedly aerated after oxygen depletion with very similar rates of subsequent oxygen reduction

using whatever amount of oxygen is presently dissolved in the culture medium in addition to that diffusing in through the cap (negligible). Once the culture had used up all its dissolved oxygen, the electrode chamber cap was removed and the culture media aerated using a Pasteur pipette. This restores oxygen levels throughout the culture and allows the bacteria to continue respiring in aerobic conditions. A typical oxygen reduction plot is shown in Figure 5.2. This is split into individual reduction sections, which can then be used as input data for parameter estimation. In many cases if the culture is allowed to become completely anaerobic for a prolonged period of time, the bacteria will die, evidenced by a subsequent lack of oxygen reduction, however this is not always the case as shown in Figure 5.3.

The experiments used to generate data for oxygen reduction are highly repeatable and consistently generate the same basic result of a linear reduction of oxygen with time.

Oxygen Reduction with Delayed Aeration

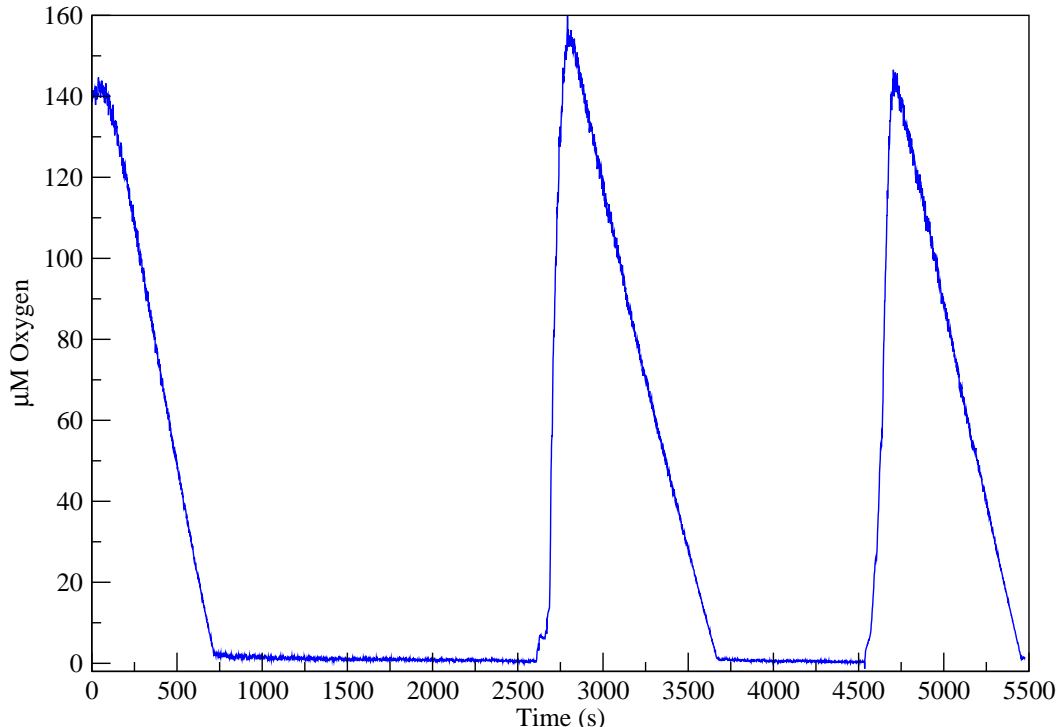


Figure 5.3: **Aerating oxygen reducing cultures with significant delay.** The oxygen reducing ability of *N. meningitidis* can be robust as evidenced by the 1000s delays between aeration with no change in subsequent respiration rate. Also of note is that nitric oxide concentration is not changing, suggesting that reduction of nitrite is not occurring either.

The oxygen reduction datasets generated and used for parametrising this portion of the mathematical model are shown in Figure 5.4.

5.1.2.1 Generation of Prior Probability Distributions

In accordance with the integrative scheme that was introduced in Chapter 4, An attempt was made to estimate the distributions of the parameters involved in modelling these data. In order to do this probability distributions were needed to act as priors to feed into the estimation system as this is required for a Bayesian approach. These probability distributions were generated from data obtained in the published literature, which is described in Chapter 3, and preliminary experimental data. It was assumed that all the prior probabilities would be log-normally distributed, therefore the distributions used were created under the following scheme:

Oxygen Reduction in *Neisseria meningitidis*

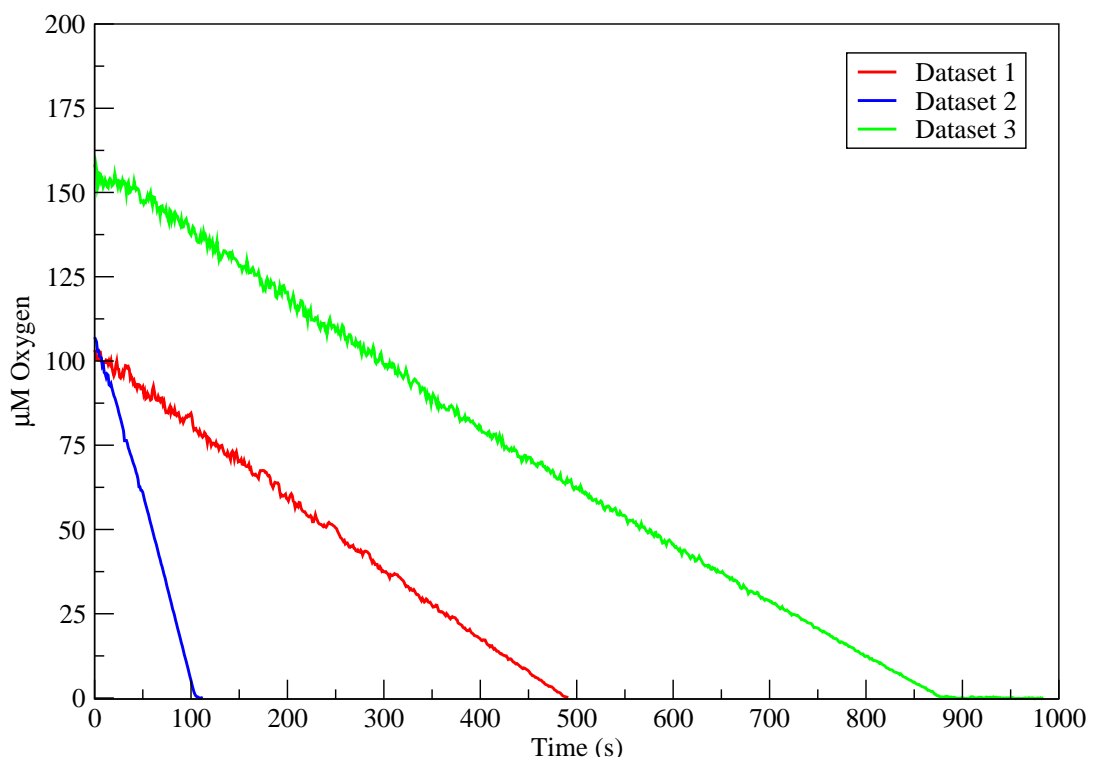


Figure 5.4: **Oxygen Reduction in *Neisseria meningitidis*.** These three experimental datasets were used as input data for the parameter estimation algorithm. They all show the same linear oxygen reduction. The different rates are due to differing starting cell densities.

- Where the literature value had bounds associated with it (i.e. published with \pm values), the bounds were assumed to cover 3σ of the normal distribution. Thus the variance used for the lognormal distribution is $\left(\frac{bounds}{3}\right)^2$ with narrow upper and lower limits.
- Where the literature value has no bounds associated with it (i.e. published as a single figure), the bounds were assumed to be $\pm 10\%$ of the literature value, and this was used as σ . Wider upper and lower limits were used in these cases.
- Where there are no literature values available, the value was estimated based on preliminary experimental data and bounds of $\pm 10\%$ were used again. In this case upper and lower limits for the distribution were made very wide to try and accommodate for incorrect assumed prior values.

With reference to the above, the values required to create prior probability distributions from Table 3.1 in Chapter 3 are shown in Table 5.1.

Parameter	\bar{x}	σ	Parameter	\bar{x}	σ
k_1	415	13.83	X	3.97	0.134
k_3	3	0.1	C	0.03	0.001
β	0.00014	4.67×10^{-6}	Q_a	0.24	0.008
g	0.847	0.028	X_a	3.176	0.105
f	8.749	0.292	C_a	0.024	0.0008
Q	0.3	0.01			

Table 5.1: **Prior Probability Table** This table shows the prior means and variances used to create lognormal distributions to be used as the prior probability distributions.

A graphical representation of the data in Table 5.1, the initial probability distributions used to start the Monte-Carlo run are shown in Figure 5.5.

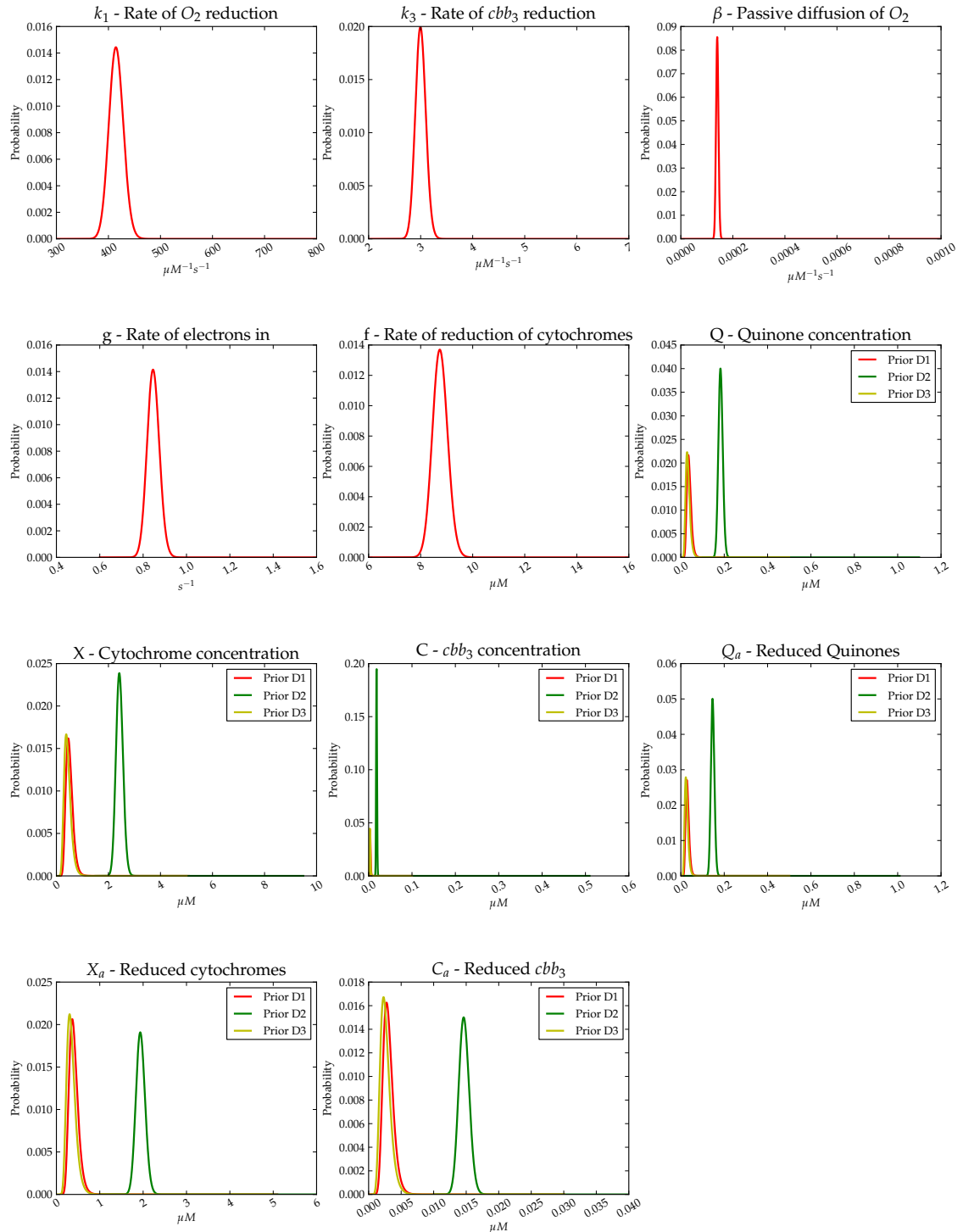
Prior probability distributions used for parameter estimation


Figure 5.5: **Prior probability distributions for oxygen reduction.** These are the probability distributions used as priors by the parameter estimation algorithm.

5.1.2.2 Initial Parameter Estimation Results

The parameter estimation process produces a large amount of output data which can be processed. Included in these data are the best simulation results from each run. Best is defined here as the simulation with the best goodness-of-fit, i.e. the one with the closest match to the experimental data. For the oxygen reduction training datasets, of which there are 3, each was run 20 times for 20,000 iterations. This lower iteration count was chosen as a compromise between execution time and statistical accuracy. In fact given that the burn-in time for these runs was relatively short, 20,000 iterations still provides plenty of data. A representative example of the simulated data is shown in Figure 5.6. This figure was generated from the set of parameters that produced the most fit output compared to the input dataset.

Initially the simulation results are not particularly good fits compared to the experimental data and as such have a low goodness-of-fit. The calculation performed actually produces a value that represents the “badness-of-fit” related to the distance of the solved data away from the experimental data and accounting for Gaussian noise. As such the quality of the solved data will be given in terms of its “badness-of-fit” or *BOF*. As the parameter estimation progresses the *BOF* reduces as the simulated result gets closer and closer to the experimental data. Quite often this does not take many iterations and a representative plot showing how the simulation’s *BOF* decreases is shown in Figure 5.7. The initial period where the *BOF* is high up until the point it settles at a lower value is classed as “burn-in” and is discarded when generating posterior distributions.

Each of the parameters that are to be estimated produces a trajectory of values for each run of the estimation algorithm. These trajectories are used to generate the posterior probability distributions required for Bayesian inference in subsequent steps. During the “burn in” period the parameter values can be observed to change rapidly from one iteration to the next as they approach their optimum values. Once the “burn in” has completed the values settle and produce largely

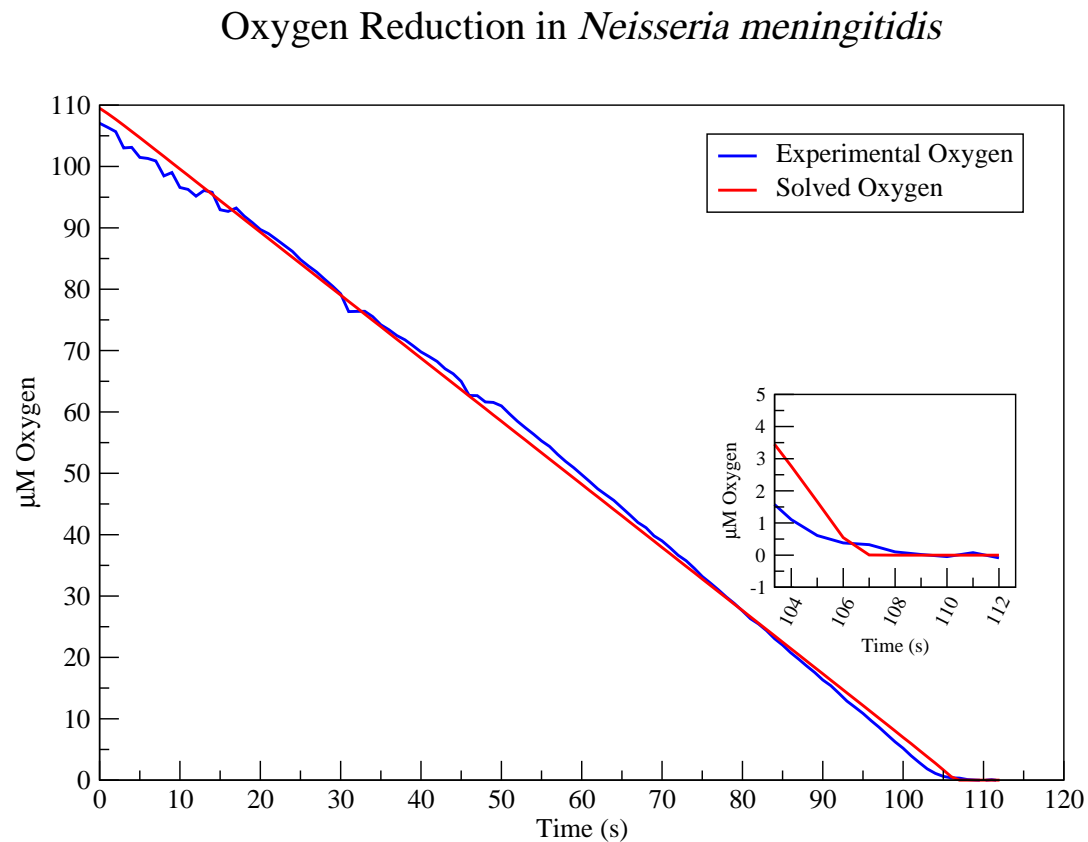


Figure 5.6: **Oxygen Reduction in *Neisseria meningitidis*.** This dataset shows the simple linear reduction of Oxygen in aerobic conditions. The high affinity of cbb_3 for oxygen is evidenced by very little non-linearity at low oxygen concentrations. The solved output is a representative result of the parameter estimation system. The inset shows that the solved output is achieving much higher affinity than the experimental data.

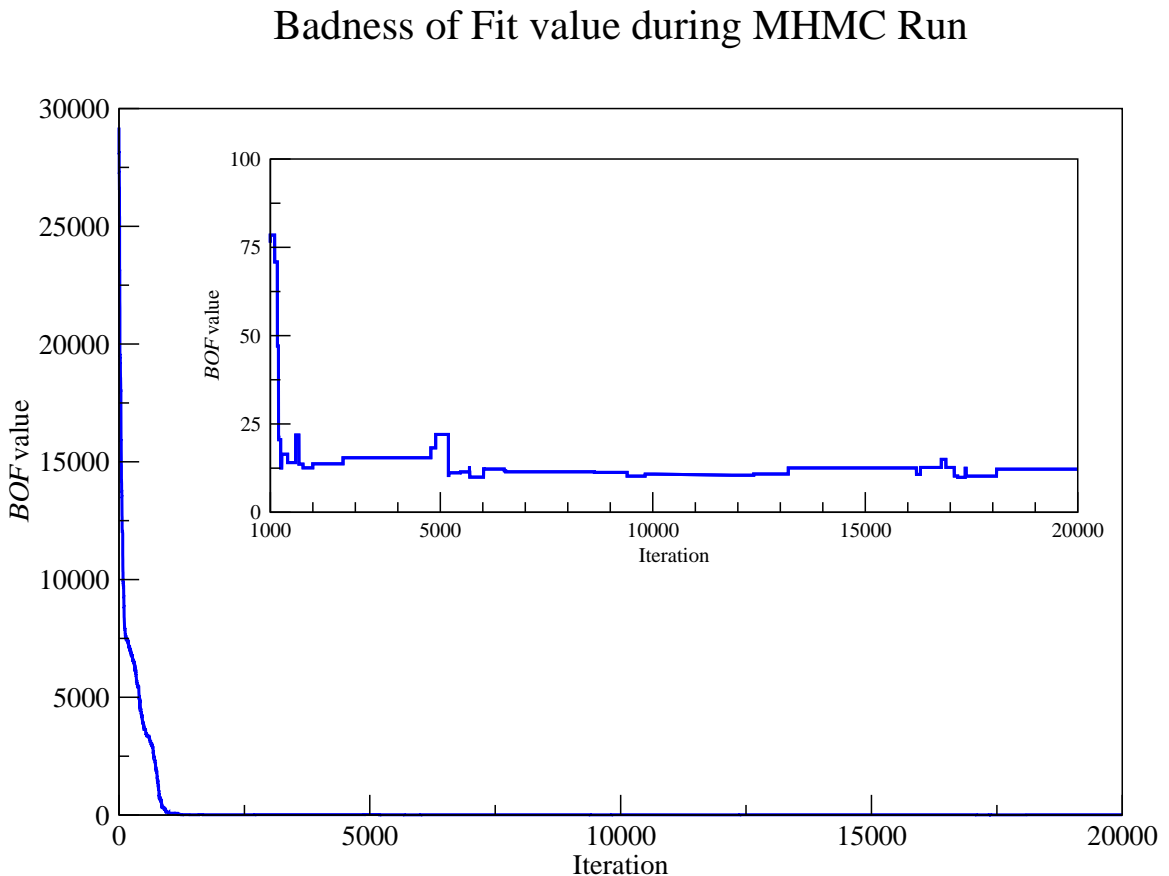


Figure 5.7: **Simulation BOF improves as parameter estimation progresses.** This is a representative figure constructed from a single run on one dataset. Initially the BOF is high showing that the simulated result does not match the experimental dataset. As the parameter estimation algorithm progresses, the BOF decreases as the simulated result approaches the experimental dataset. The inset shows a zoomed in view of the BOF after the “burn-in” process has finished.

flat trajectories with minor deviations around the optimum value. This settled region is used as the source for generating the posterior probability distributions.

Figure 5.8 shows the trajectories from each simulation run on a single dataset for the k_3 parameter.

Not all parameters in this stage of the model will produce trajectories like the one shown, as if there is a great deal of freedom as to what value a particular parameter can take without drastically decreasing the *BOF* it will be accepted by the parameter estimation algorithm. In this case the trajectories will not converge, and will ultimately produce a wide probability distribution. This is not necessarily indicative of a problem however, as this output still contains information that can be used in the next stage of parameter estimation with new datasets.

The trajectories above are processed to produce probability distributions given as histograms. The “burn in” is discarded and the settled data is then binned and counted. For the datasets used, the burn-in period was 1500 iterations (10,000 for dataset 3). These histogram probabilities are then assigned as the posterior distributions and in turn are used directly as prior probability distributions for new datasets. For simplicity’s sake when referring to the distribution of individual parameters for purposes of comparison, these histograms are transformed into log-normal distribution such that they can be represented by two numbers, \bar{x} - the mean, and σ^2 - the variance.

The posterior probability distributions generated from the three experimental datasets, each started with 20 runs are shown in Figure 5.9. In the case of parameters which represent concentrations, such as X and C, the concentrations of cytochromes and cbb_3 respectively, the individual dataset probability distributions are shown, as they cannot be sensibly combined, and it emphasises the fact that the datasets were different.

As can be seen from the posterior distributions, the parameter estimation algorithm has not satisfactorily produced posterior distributions that are contained within the bounds of the prior distributions whilst also still managing to fit to the

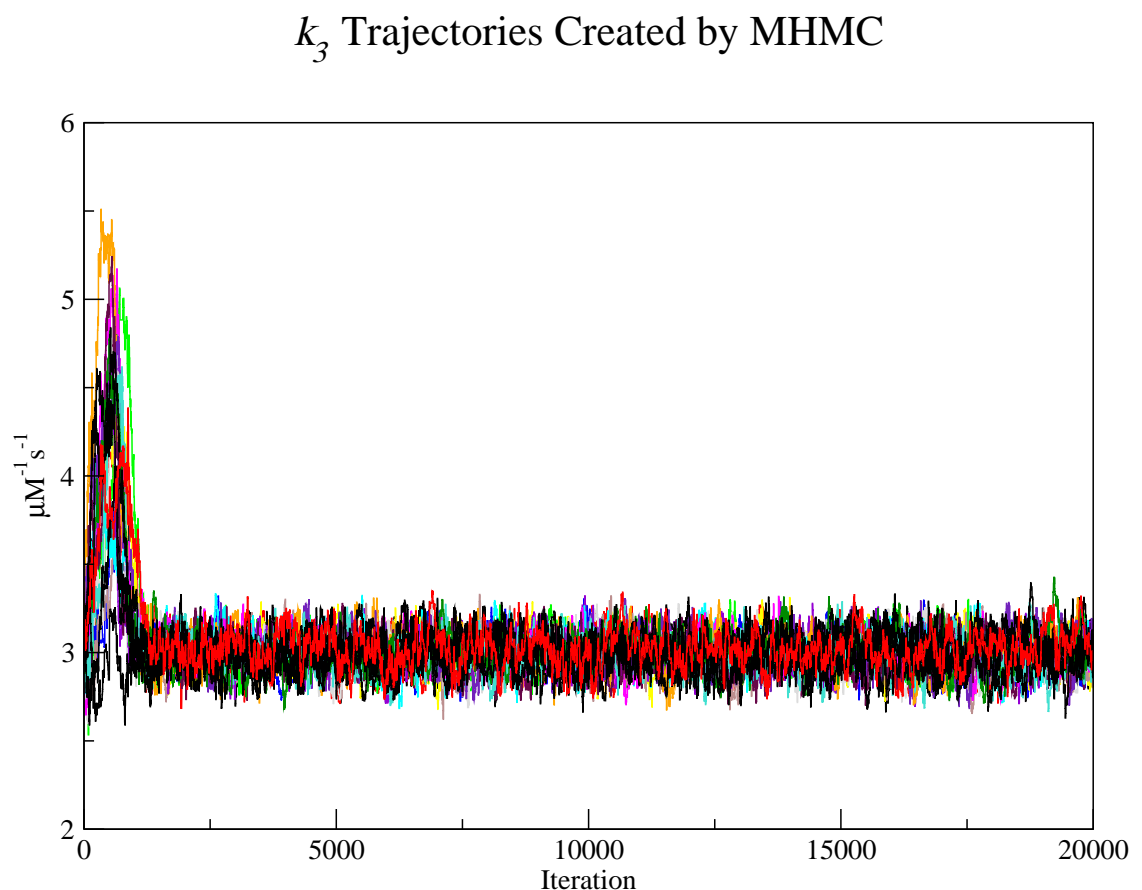


Figure 5.8: **Individual parameter trajectories for multiple runs on the same experimental dataset.** This figure shows the trajectories for the same parameter, in this case k_3 - the rate constant for cbb_3 reduction, from 20 individual runs of parameter estimation upon the same input data. The trajectories show clear convergence after the “burn-in” period.

Posterior probability distributions created by parameter estimation

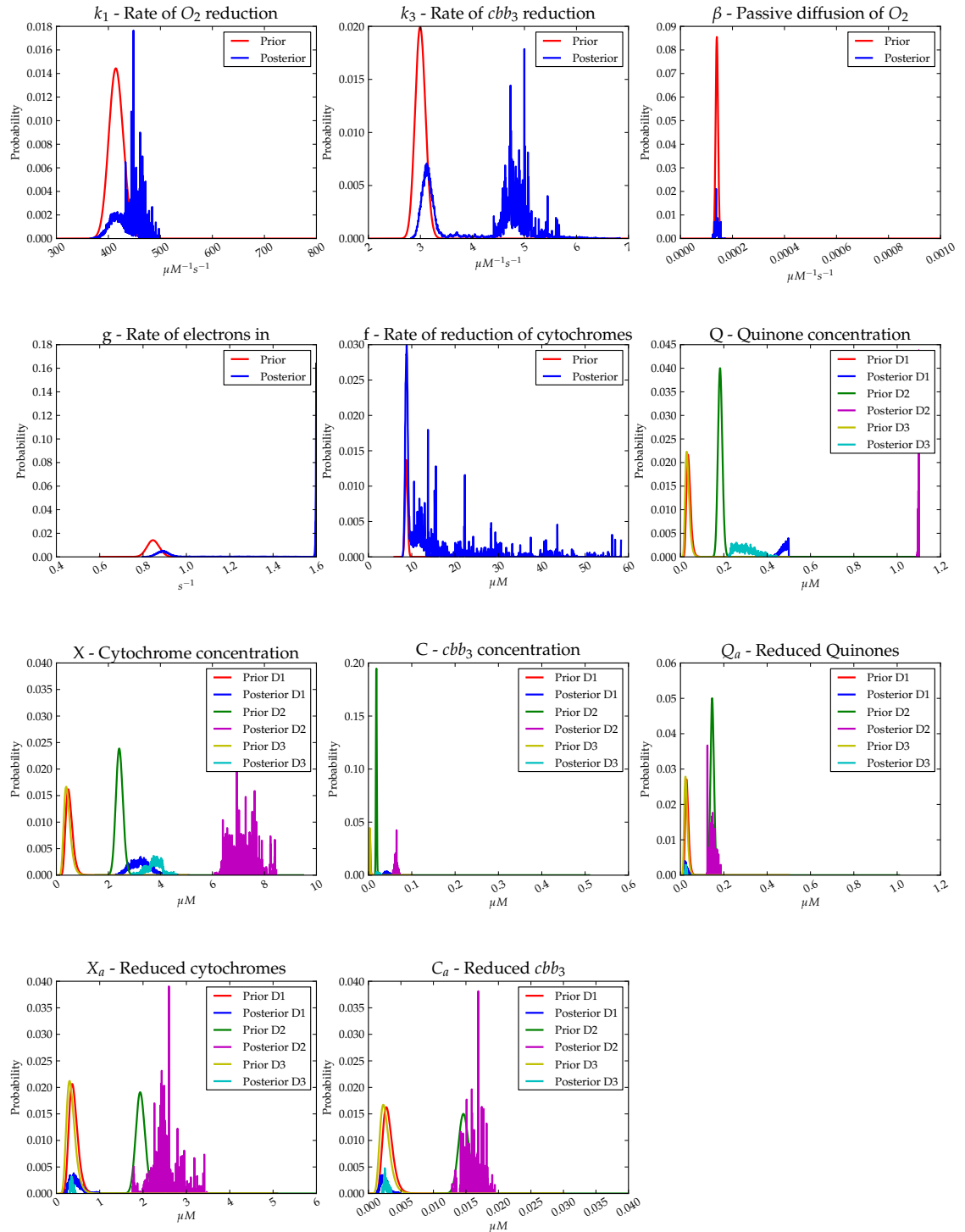


Figure 5.9: **Posterior probability distributions for oxygen reduction.** These are the probability distributions generated by parameter estimation on 3 oxygen reduction datasets. These have been overlaid onto the prior probability distributions used by the parameter estimation algorithm, also shown in Figure 5.5.

experimental data. This is especially true of the concentration of Q , where the Markov-chain has tended towards the upper limit of the input prior distribution. This suggests that the prior distribution for Q is incorrect, with a mean that is possibly as much as $10\times$ too low, and with a variance that is too small, as the parameter estimation algorithm has attempted to increase the value of Q right up to the upper limit of the input distribution. This incorrect value for Q is probably the cause of several of the other distributions being flatter and outside of the main body of their prior distributions. Another interesting observation is that the distribution for k_3 shows a distinct bi-modality, however this is quite likely to be an artefact of the parameter estimation algorithm. The left-most region of the bimodal distribution could be caused by the natural bias of the algorithm for values within more likely regions of the prior probability distribution. If this is the case, the right-most region is the “true” probability distribution where the increase in likelihood of fitting outweighs the fact that the values selected have a low probability of being selected from the prior distribution. Assuming this is the case, the prior distribution may also be incorrect for k_3 , but the shape of the posterior distribution may also be directly caused by the more obviously incorrect prior distribution of Q .

Since the posterior probability distributions generated at this stage cannot be used as priors for the reasons described above, the prior distributions were altered to try and correct them. These alterations are described in the next section.

5.1.2.3 Secondary Prior Probability Distributions

To improve the prior probability distribution to counteract the behaviour seen in the section above, a number of changes were made to the distribution parameters. All of the rate constant and total concentration parameters were flattened out, that is to say the variance was increased. In addition the mean value for Q was increased tenfold since the previously described results showed this value was far too low. The parameters for reduced enzyme concentration were not altered,

as the ODE solver is accurate enough to correct these immediately. The values required to create the updated prior probability distributions are shown in Table 5.2.

Parameter	\bar{x}	σ	Parameter	\bar{x}	σ
k_1	415	30.93	X	3.97	0.424
k_3	3	0.316	C	0.03	0.003
β	0.00014	4.67×10^{-6}	Q_a	0.24	0.008
g	0.847	0.089	X_a	3.176	0.105
f	8.749	1.732	C_a	0.024	0.0008
Q	3	0.1			

Table 5.2: **Prior Probability Table** This table shows the prior means and variances used to create lognormal distributions to be used as the prior probability distributions.

A graphical representation of the data in Table 5.2, the initial probability distributions used to start the Monte-Carlo run are shown in Figure 5.10.

5.1.2.4 Secondary Parameter Estimation Results

The posterior probability distributions for this second attempt were generated in the same way as described previously for the first attempt.

The second attempt at parameter estimation, revealed an issue with the input datasets that were being used. The first dataset contains no information about what happens to the rate of oxygen reduction once oxygen concentration approaches zero, as the experimental data does not extend this far. The second and third datasets do contain this information as they show complete oxygen reduction to zero, in addition to several seconds of data after that point. This can be seen in Figure 5.4.

The result of dataset 1 lacking this additional feature is that the parameter estimation algorithm was able to over-sample from the prior distributions as there was no significant difference in goodness-of-fit between “in prior” and “out of

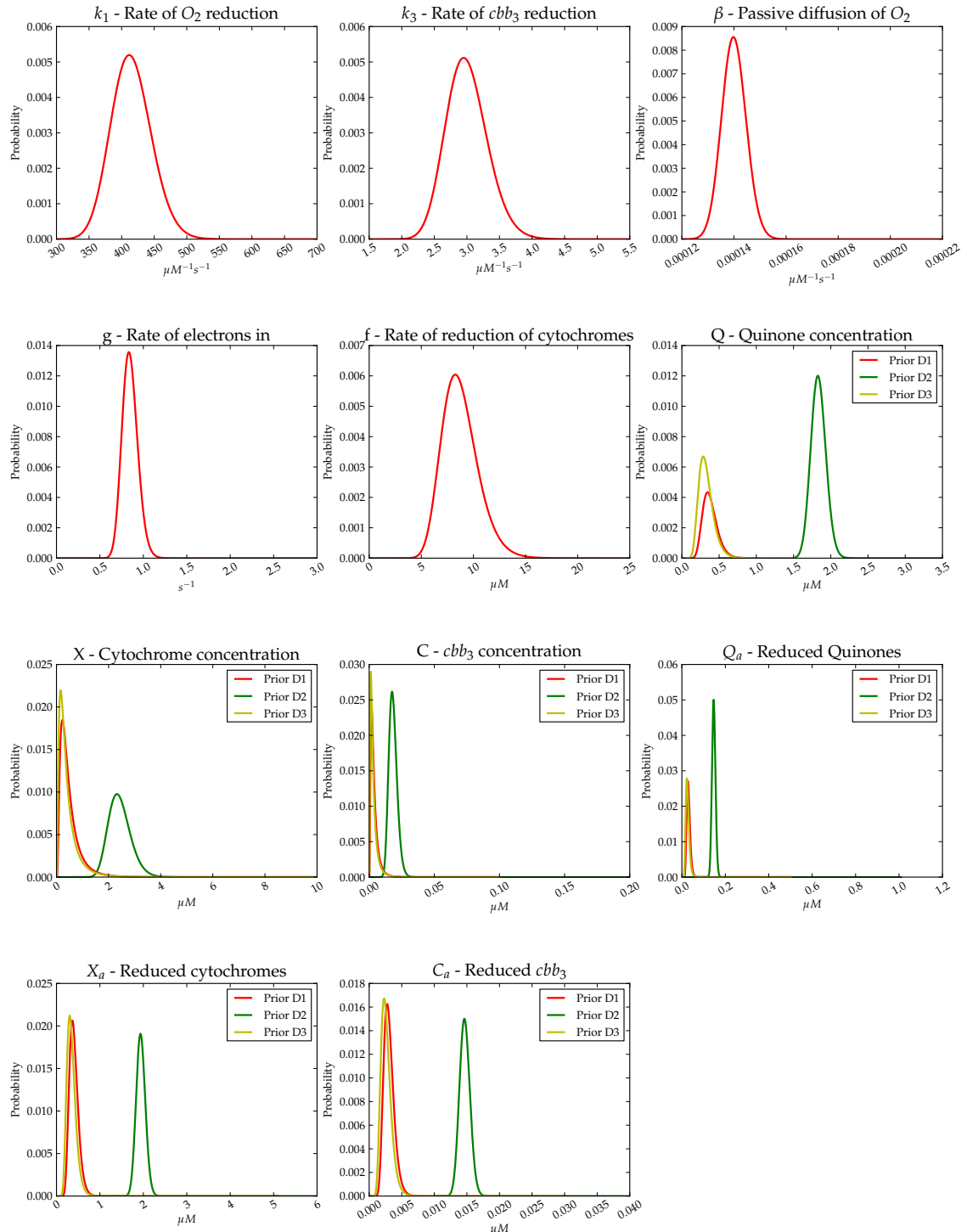
Prior probability distributions used for parameter estimation


Figure 5.10: **Prior probability distributions for oxygen reduction.** These are the probability distributions used as priors by the parameter estimation algorithm.

prior" parameter values. If these distributions were to have been included in the overall posterior probability distributions for oxygen reduction they would have skewed the distributions towards the priors rather than their true values. The posterior distributions for dataset 1 are shown in Figure 5.11.

The usable posterior probability distributions were therefore generated from the experimental datasets 2 & 3, each started with 20 runs and are shown in Figure 5.12. In the case of parameters which represent concentrations, such as X and C , the concentrations of cytochromes and cbb_3 respectively, the individual dataset probability distributions are shown, as they cannot be sensibly combined, and it emphasises the fact that the datasets were different.

In the posterior distributions there still appears to be a degree of bimodality in the distribution of the k_1 , but this distribution is still contained within the prior bounds, and for the purposes of generating a prior probability distribution for the datasets in the next chapter was altered to produce a lognormal distribution that encompasses the entire posterior distribution. The distribution of k_3 is perhaps the most interesting as it shows that the estimates used as priors are most likely incorrect as the posterior distribution has shifted significantly to the right, increasing the mean value of the parameter by a factor of $\approx 1.5\times$. The other rates are largely similar to their prior distributions suggesting that the priors were good estimates for the actual values. The prior distribution for Q had already been altered as described previously and the new value chosen seems to be a great deal better based on the closeness of the posterior distribution to the altered prior distribution. The concentrations of X and C appear to be under-estimated in the prior distributions, as the posteriors show a significant shift to the right as with k_3 . A comparison between the prior probability distributions and the posterior probability distributions can be seen in Table 5.3. In this table the obtained distributions have been fitted to lognormal distribution which can be described by 2 parameters, which makes comparing the distributions much easier.

Posterior probability distributions created by parameter estimation

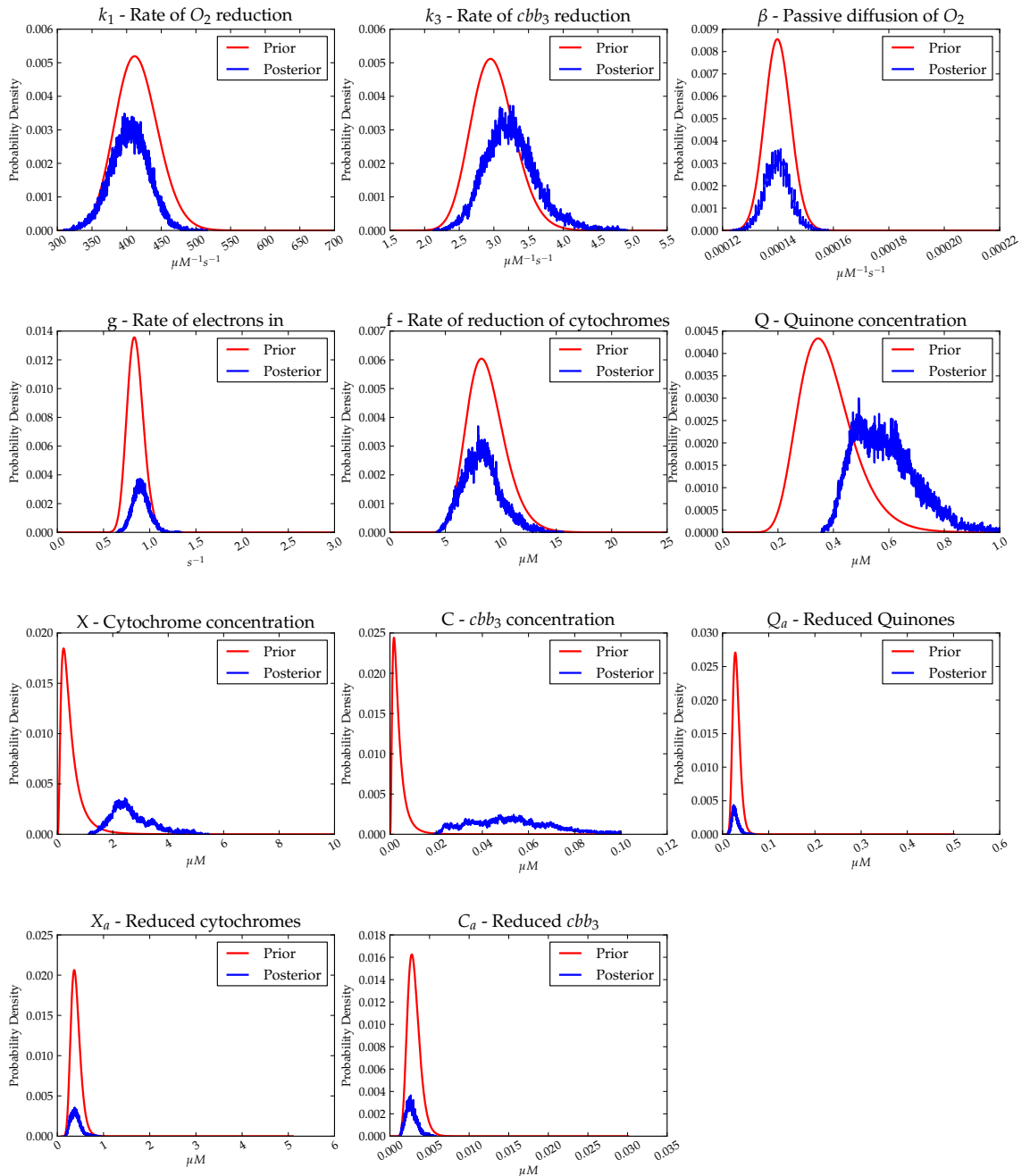


Figure 5.11: Oversampled Posterior Distributions. The posterior probability distributions for dataset 1 of oxygen reduction are oversampled from the prior probability distributions. This is not directly obvious by the probability distributions alone, but in conjunction with the input dataset which lacks features present in datasets 1 and 2. In this case both k_1 and k_3 are skewed towards the prior probability distributions, and this causes the distribution of C to be very wide as it can take a very broad range of values without affecting the goodness of fit of the solved data to the experimental data.

Posterior probability distributions created by parameter estimation

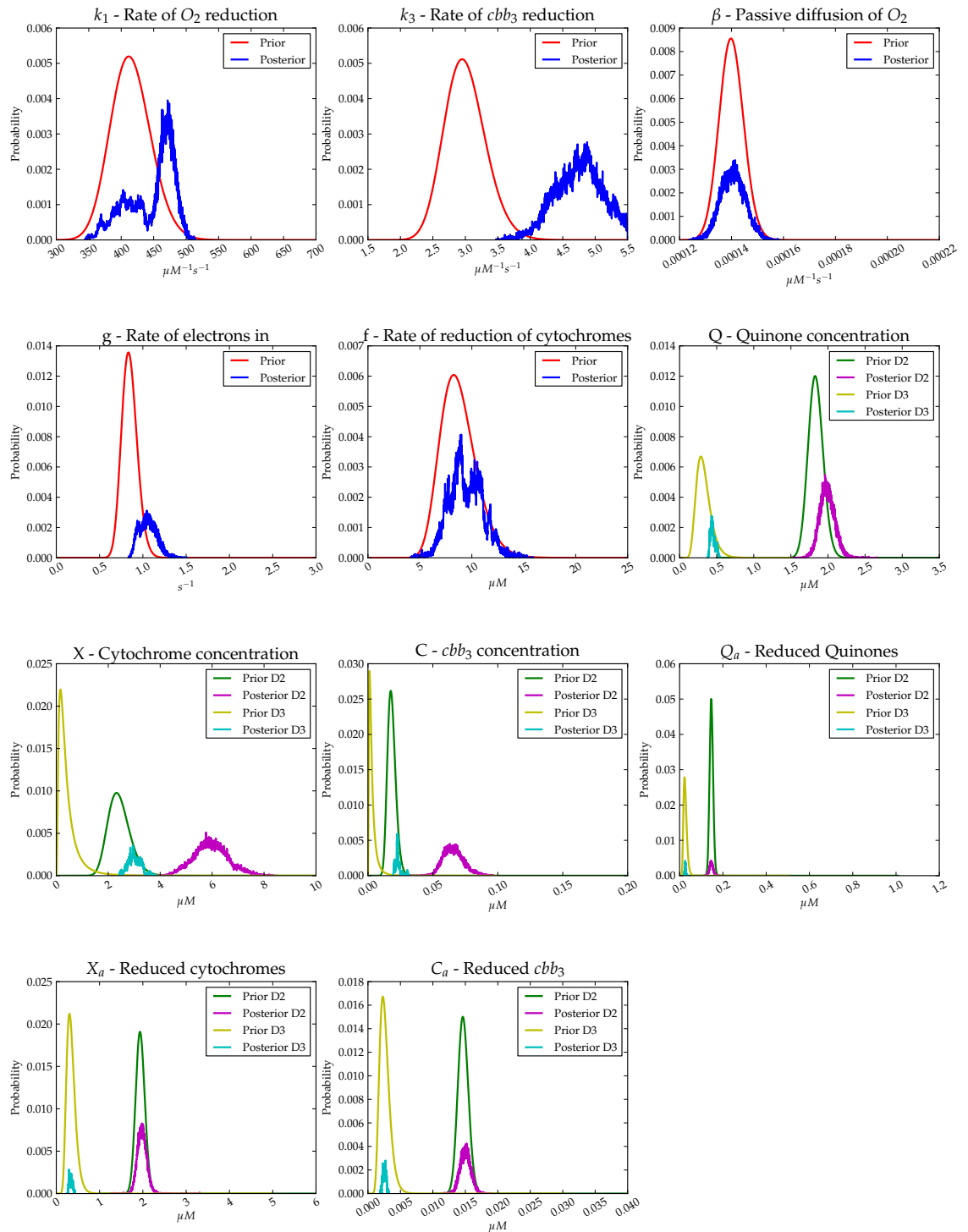


Figure 5.12: **Posterior probability distributions for oxygen reduction.** These are the probability distributions generated by parameter estimation on 2 oxygen reduction datasets. These have been overlaid onto the prior probability distributions used by the parameter estimation algorithm, also shown in Figure 5.10.

Parameter	Priors		Posteriors	
	\bar{x}	σ	\bar{x}	σ
k_1	415	30.93	450 ↑	35 ↑
k_3	3	0.316	4.748 ↑	0.404 ↑
β	0.00014	4.67×10^{-6}	0.00014	4.72×10^{-6}
g	0.847	0.089	1.053 ↑	0.099
f	8.749	1.732	9.10 ↑	1.18 ↓
Q	3	0.1	3.59 ↑	0.132
X	3.97	0.424	15.177 ↑	0.247 ↓
C	0.03	0.003	0.143 ↑	0.159
Q_a	0.24	0.008	0.24	0.034 ↑
X_a	3.176	0.105	3.158	0.039 ↓
C_a	0.024	0.0008	0.024	0.036 ↑

Table 5.3: **Posterior Probability Statistics.** This table shows the parameters required to create lognormal distributions that describe the prior and posterior probability distributions. The values for the priors are as in Table 5.2. The posterior distributions were generated from datasets 2 & 3, and where they relate to concentrations, these have been normalised. The lognormal distributions represent best-fits to the actual posterior distributions. Where there are significant differences between the prior and posterior values for either the mean or standard deviation, these are indicated by ↑ and ↓.

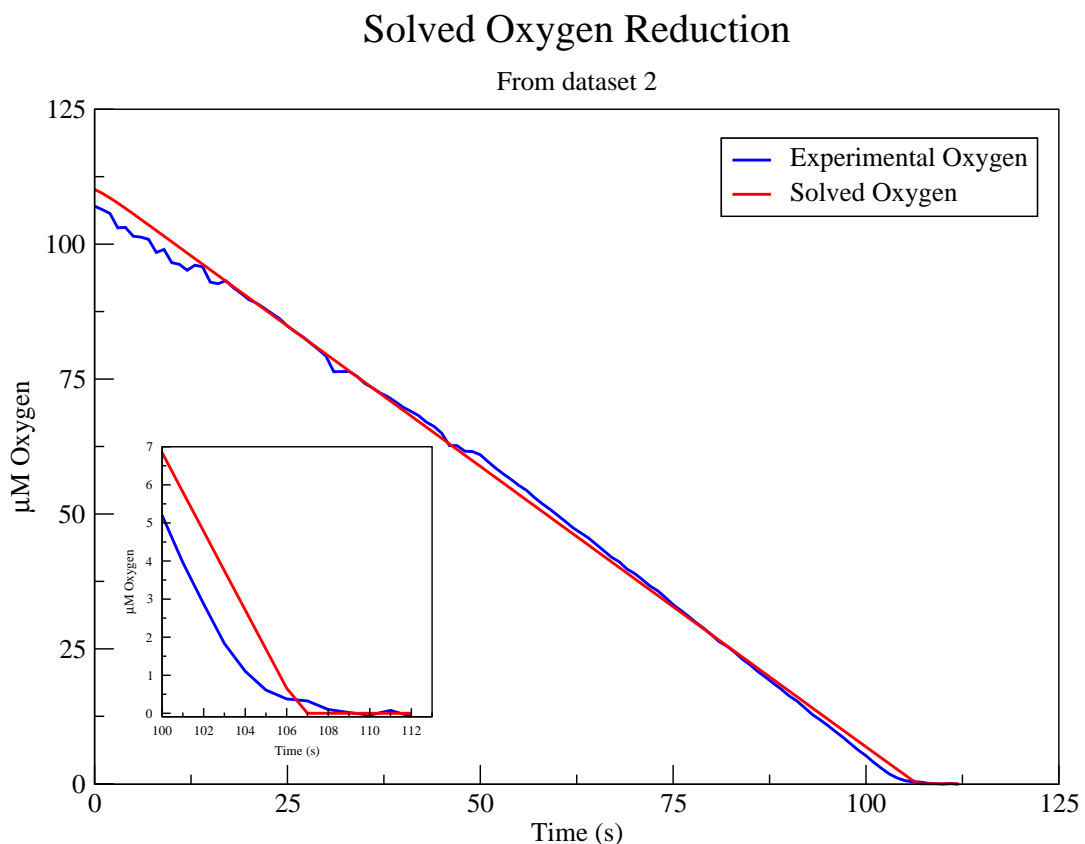


Figure 5.13: **Oxygen Reduction in *Neisseria meningitidis*.** This figure shows how well the best solved data fits against the experimental data from dataset 2. The inset shows again, that the solved output is achieving much higher affinity than the experimental data.

A graph showing how well the solved output fits the experimental data during the parameter estimation stage is shown in Figure 5.13. This shows the solved output which achieved the best goodness of fit against the experimental data.

5.1.2.5 Analysis of Convergence

It is possible to calculate the degree of convergence of the parameters from the Monte Carlo trajectories using the R statistic introduced by Gelman and Rubin¹¹² and Brooks and Gelman¹¹³. This statistic is a single value that represents how close the trajectories for each individual parameter have come to convergence. The R statistic was calculated using the *Bolstad2*¹¹⁴ library for R¹¹⁵.

Table 5.4 shows the R statistics obtained from the trajectories run for oxygen reduction parameter estimation. The R statistic is a measure of scale-reduction, and fully converged trajectories will have a value of 1.0 whereas trajectories which have not converged will have values greater than 1 with the magnitude depending on how far away from converging they are. The R statistic shows that all of the rate constants appeared to have converged to a reasonably high degree which could also be seen from the distribution plots. The concentration parameters had converged to a much lesser degree however this was not completely unexpected, as there were a larger number of parameters in the model than were required to fit the experimental data and thus the potential range of parameter values was broad at this stage. The apparent lack of convergence of some parameters at this point was not a problem as with subsequent, more complex datasets, the range of potential parameter values should decrease, allowing the trajectories to converge more easily.

5.1.2.6 Analysis of Correlation

Given the large number of parameters, and the simple form of the experimental data it is quite likely that a number of the parameters will be correlated with one another. This effect should also have been exacerbated at this stage due to the

Parameter	R value	Parameter	R value
k_1	3.77	X	14.96
k_3	1.56	C	8.72
β	1.15	Q_a	2.39
g	1.98	X_a	2.34
f	2.48	C_a	2.30
Q	4.16		

Table 5.4: **Gelman-Rubin Convergence Statistic.** This table shows the Gelman-Rubin Convergence statistic for all the Markov chains from datasets 2 & 3. For parameters which are concentrations, the statistic relates to the values after normalisation (data is normalised based on initial oxygen reduction rate). Concentration parameters exhibit greater inter-dataset differences even after normalisation thus giving high R statistic values. The intra-dataset values are lower.

limited constraints (by virtue of wide prior probabilities) on the ranges of values that parameters can take. In order to investigate this a set of correlation matrices were constructed by calculating the Pearson's Product-Moment Correlation Coefficient for each of the parameters. This value provides the direction of correlation as indicated by the sign, and the degree of linearity as indicated by the magnitude. A positive correlation indicates that as the value of one parameter increases, the other increases also. A negative correlation indicates that as the value of one parameter increases, the other decreases.

The upper-triangle correlation matrices are shown in Figures 5.5 & 5.6 and were constructed by concatenating all the trajectories created by the parameter estimation system (discarding the burn-in) together and the Pearson's Product-Moment Correlation Coefficient calculated for each combination for each dataset. The datasets were analysed separately to allow examination of intra dataset correlation. The matrices are upper-triangle only as the lower triangle is a duplicate of the same data. The diagonals are shown in grey as they are not useful data since the correlation of X against X is always 1.

The correlation matrices show that most of the model parameters are not

	k_1	k_3	β	g	f	Q	X	C
k_1	1	0.009239	0.017156	0.049769	-0.011922	0.020906	0.022824	0.033631
k_3		1	-0.027037	-0.083623	0.052659	-0.040318	-0.202936	-0.411031
β			1	-0.002919	0.000809	-0.013785	0.007012	0.022641
g				1	-0.038259	-0.332178	0.199383	-0.152613
f					1	-0.03624	-0.087711	-0.034303
Q						1	0.083179	-0.043061
X							1	-0.577183
C								1

Table 5.5: **Regression Analysis of Oxygen Reduction Parameters for Dataset 2.** This table shows the R values from linear regression analysis on the combined parameter trajectories for Oxygen reduction. Parameters with high correlation have been coloured green ($R > 0.8$) and those with moderation correlation have been coloured orange ($0.8 > R > 0.3$).

	k_1	k_3	β	g	f	Q	X	C
k_1	1	0.06739	0.005008	0.222959	-0.077916	-0.243691	0.056941	-0.036059
k_3		1	0.249	-0.173314	0.304448	0.018672	-0.487193	-0.313064
β			1	0.065203	-0.033434	0.053464	-0.026229	-0.174494
g				1	-0.276682	-0.104876	0.250671	-0.210795
f					1	-0.146998	-0.496387	0.243878
Q						1	0.158161	-0.397437
X							1	-0.624574
C								1

Table 5.6: **Regression Analysis of Oxygen Reduction Parameters for Dataset 3.** This table shows the R values from linear regression analysis on the combined parameter trajectories for Oxygen reduction. Parameters with high correlation have been coloured green ($R > 0.8$) and those with moderation correlation have been coloured orange ($0.8 > R > 0.3$).

correlated with each other, giving low to very low R values. Between the two datasets the only parameters that appear to be correlated are C and X and k_3 and X , and these are both negative correlations. The negative correlation between k_3 and X can be explained by the fact that as the concentration of X decreases, an increase in k_3 is required to maintain the same rate of electron flow out of the cytochrome pool. The correlation between C and X can be explained by factoring in the fact that the rate of oxidation of C is very high. This should lead to any reduced cbb_3 being oxidised almost straight away. Therefore if the concentration of X increased, it would lead to an increase in the reduction state of C (as there will be more electrons to move from X to C), so to maintain the same eventual rate of oxygen reduction (by oxidation of C), the concentration of C must decrease. The converse is also true. The fact that there are intra-dataset correlations that don't appear in both datasets suggests that the rates and concentrations in the two datasets haven't been completely decoupled from the optical density (or in this case the reduction rate proxy for OD).

5.1.3 Discussion

The experimental datasets showed that oxygen reduction in *N. meningitidis* is a simple almost completely linear system with the reductase having a high affinity for oxygen demonstrated by the almost complete lack of non-linearity as oxygen concentration approaches zero. This simple linearity could be very easily have been modelled to a high degree of accuracy with just 2 parameters in a simple $y = -mx + c$ system. Admittedly this would not include the behaviour when the oxygen concentration reaches zero, where there is some non-linearity. However this essentially meant that there were a much larger number of parameters available to fit than were necessary, which lead to over-fitting of the data. The size of the parameter set meant that there were a very large set of potential combinations that would have lead to a similar result, however this was mitigated somewhat by the prior probability distributions given to the algorithm. Even so, this meant

that the posterior distributions generated were very wide and therefore allowed much greater freedom for the next dataset to explore the parameter space.

With the knowledge of the underlying transport chain and the affinity of *cbb₃* for oxygen, a linear reduction of oxygen with high affinity over nearly two orders of magnitude was expected. This was evidenced in the experimental data. It is however remarkable that this behaviour can be modelled with so few components in the model, as it requires significant changes in the reduction states of the enzymes to achieve this.

Chapter 6

Nitric Oxide Reduction in *N. meningitidis*

6.1 Aerobic Nitric Oxide Reduction

6.1.1 Introduction

The next dataset I used in my iterative approach to parameter estimation was of one of aerobic oxygen reduction interrupted by the addition of Nitric Oxide. This dataset is the next most complicated after aerobic oxygen reduction as it introduces the nitric oxide reduction pathway. The portions of the ETC relating to Nitric Oxide reduction are shown graphically in Figure 6.1. However this pathway cannot be isolated *in vivo* as *N. meningitidis* is incapable of completely anaerobic respiration therefore the required parts of the model are actually those from Chapter 5 and those in Figure 6.1. The equations that describe this portion



Figure 6.1: **Nitric oxide reducing electron transport chain of *N. meningitidis*.** This shows the complete electron transport chain of *Neisseria meningitidis* with the components irrelevant to nitric oxide reduction greyed out.

of the ETC are:

$$\begin{aligned}
 \frac{d[O_2]}{dt} &= \beta(1 - [O_2]/K_O) - k_1[C_a][O_2] \\
 \frac{d[Q_a]}{dt} &= g([Q] - [Q_a]) - l_3[Q_a]([B] - [B_a]) - f[Q_a]([X] - [X_a]) \\
 \frac{d[X_a]}{dt} &= -k_3([C] - [C_a] - [C_X])[X_a] - m_3([A] - [A_a])[X_a] + f[Q_a]([X] - [X_a]) \\
 \frac{d[C_a]}{dt} &= k_3([C] - [C_a] - [C_X])[X_a] - k_1[C_a][O_2] - k_5[C_a][NO] \\
 \frac{d[NO]}{dt} &= m_1[NO_2^-][A_a] - l_1[NO][B_a] - k_5[C_a][NO] + k_6[C_X] - \gamma[NO] \\
 \frac{d[C_X]}{dt} &= k_5[C_a][NO] - k_6[C_X] \\
 \frac{d[B_a]}{dt} &= l_3[Q_a]([B] - [B_a]) - l_1[NO][B_a]
 \end{aligned}$$

These equations describe the change in concentration of Nitric Oxide over time, which is the experimentally observable value (in addition to the afore modelled oxygen). Also being modelled was the change in concentration of inhibited *cbb3* and the reduction state of NorB. This portion of the model involved 24 parameters

and variables which I needed to estimate. This number includes the 13 values already estimated in Chapter 5.

6.1.2 Experimental Results

Generation of nitric oxygen reduction datasets required the growth of MC58 (wild type *Neisseria meningitidis*) in aerobic conditions until mid log-phase growth had been achieved. This corresponds to an OD_{600} of 0.3-0.9 and usually required an incubation period of roughly 3 hours. Once the required cell density had been obtained, I transferred the culture to the oxygen electrode chamber and recorded the oxygen and nitric oxide concentrations as the culture respiration. To model nitric oxide reduction required that I add nitric oxide solution to the culture while it is respiring aerobically. Part-way through aerobic respiration I added nitric oxide solution to various final concentrations at $\approx 5 \mu\text{M}$ and the culture then left to respire nitric oxide. An example dataset showing the effect of addition of nitric oxide to an aerobically respiring culture is shown in Figures 6.4, 6.2 & 6.3.

The dataset in Figure 6.2 shows very little change in the rate of oxygen reduction (it is in fact somewhere around a 3% reduction in rate) when a small amount of nitric oxide is added. The observed removal of nitric oxide is due primarily to diffusion although there may also be some preliminary (as the culture has not been primed with nitric oxide) nitric oxide reductase activity.

The dataset in Figure 6.3 shows a larger change in the rate of oxygen reduction than that of Figure 6.2 when a larger amount of nitric oxide is introduced. Again the removal of nitric oxide will primarily be due to diffusion, although now at higher concentrations more nitric oxide will interact with cbb_3 temporarily inhibiting it. This inhibition causes the reduction in oxidase activity, and the sequestering of NO by cbb_3 also causes some of the visible reduction in nitric oxide concentration. The time-scale over which the nitric oxide disappears strongly suggests that it is not due to nitric oxide reductase activity. It may also be possible that at this concentration of nitric oxide some cbb_3 may have been permanently

Nitric Oxide Reduction in *Neisseria meningitidis*



Figure 6.2: **Nitric Oxide Reduction in *Neisseria meningitidis*.** This dataset shows the effect on rate of oxygen reduction as a small amount of nitric oxide is introduced to the system.

Nitric Oxide Reduction in *Neisseria meningitidis*



Figure 6.3: **Nitric Oxide Reduction in *Neisseria meningitidis*.** This dataset shows the effect on rate of oxygen reduction as a larger amount of nitric oxide is introduced to the system.

Nitric Oxide Reduction in *Neisseria meningitidis*

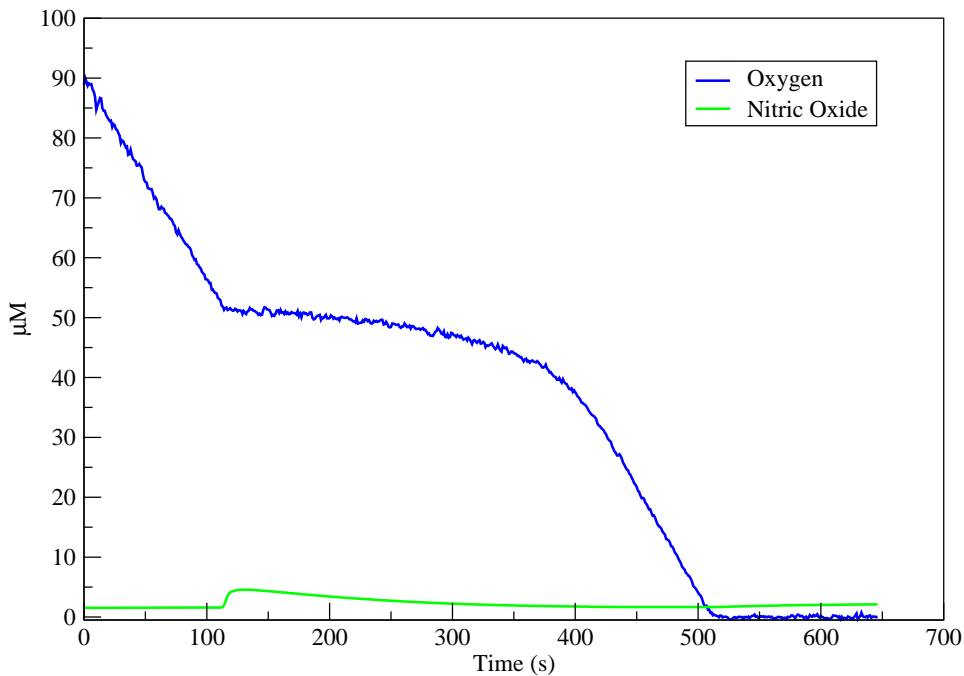


Figure 6.4: **Nitric Oxide Reduction in *Neisseria meningitidis*.** This dataset shows the effect on rate of oxygen reduction as nitric oxide is introduced to the system which appears to have been primed for nitric oxide reduction.

inhibited as mentioned in Chapters 1 & 3.

The dataset in Figure 6.4 appears to show a system that is partially primed for microaerobic respiration. In this case there is a small amount of NorB (nitric oxide reductase) present. Initially the oxygen reduction is carried out in exactly the same manner as in Chapter 5. Upon addition of nitric oxide, oxygen respiration slows and almost stops as a result of competition for electrons between *cbb*₃ and NorB, and the direct chemical inhibition of *cbb*₃ by NO. Nitric oxide starts being removed as a combination of diffusion (although this rate will be low as shown in the previous two datasets) and reduction via NorB. Once the NO has been removed from the system oxygen reduction resumes at almost the same rate as before and still has the same high affinity feature as the oxygen reduction datasets in Chapter 5.

6.1.2.1 Prior Probability Distributions

The prior probability distributions used for parameter estimation of these datasets were a combination of the posterior distributions generated in Chapter 5 and those from the literature as described in Chapter 3. Where the probability distributions were not generated from the oxygen reduction datasets they were created using them same scheme as described in Chapter 5. The initial probability distributions used to start the Monte-Carlo runs are shown in Figure 6.5. As can be seen, much more information is now available than was present for oxygen reduction.

6.1.2.2 Parameter Estimation Results

The parameter estimation process was run in the same fashion as that described in Chapter 5. The 3 experimental datasets were run 20 times (each) for 20,000 iterations using the prior probability distributions shown in Figure 6.5. A representative example of the solved output from one of the trajectories from the experimental dataset shown in Figure 6.4 is shown in Figure 6.6. This figure was generated from the set of parameters that produced the most fit output compared to the input dataset. The model was able to generate a parameter set from the prior probability distributions that could accommodate all the new features of the dataset as evidenced by the closeness of fit of the solved output to the experimental data. This parameter set will also still be able to model simple oxygen reduction.

Prior probability distributions used for parameter estimation

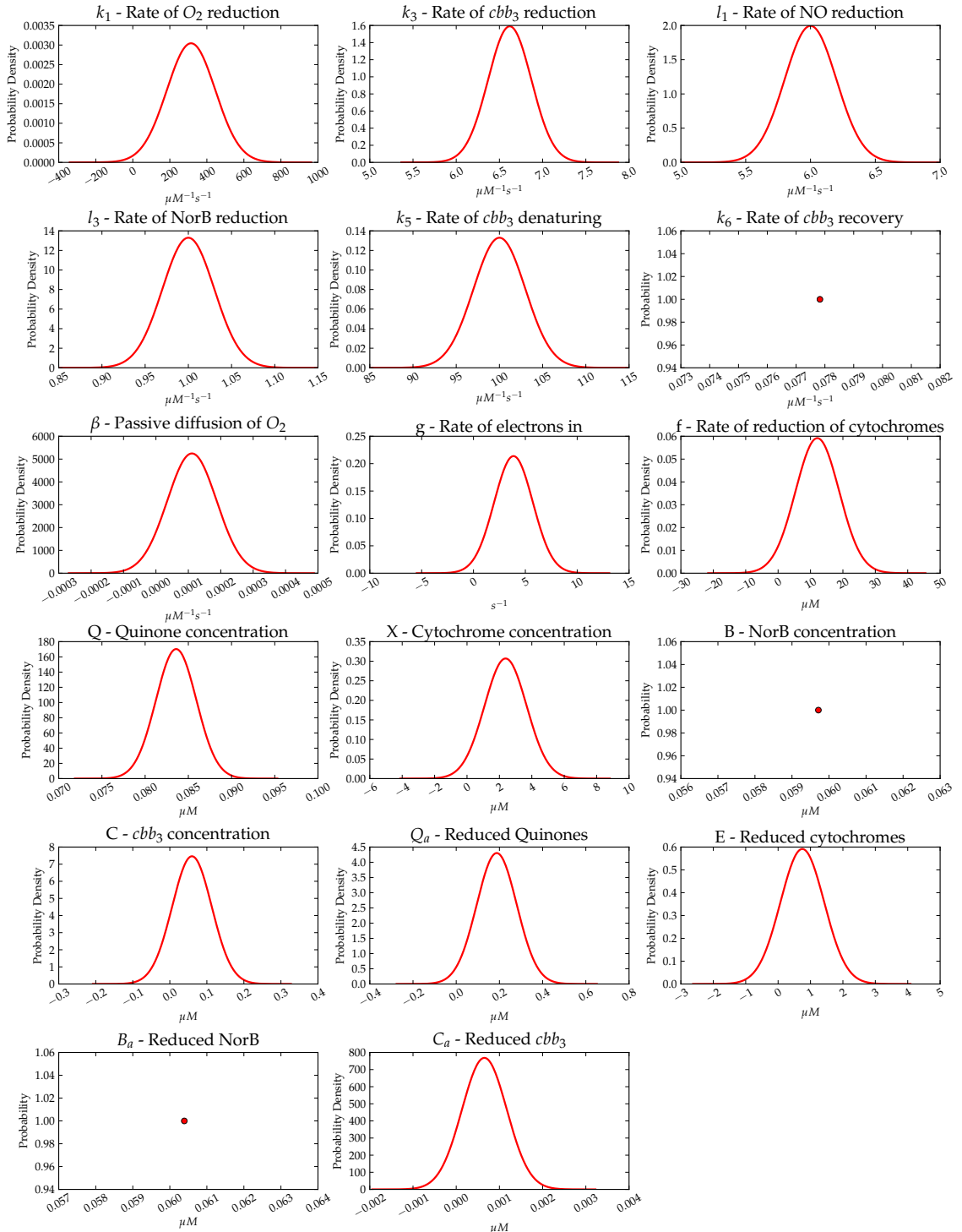


Figure 6.5: **Prior probability distributions for aerobic nitric oxide reduction.** These are the probability distributions used as priors by the parameter estimation algorithm. Where no values were available in the literature, the probability distribution represents a flat prior from 0 to ∞ with the initial value being determined by preliminary experiment.

Nitric Oxide Reduction in *Neisseria meningitidis*

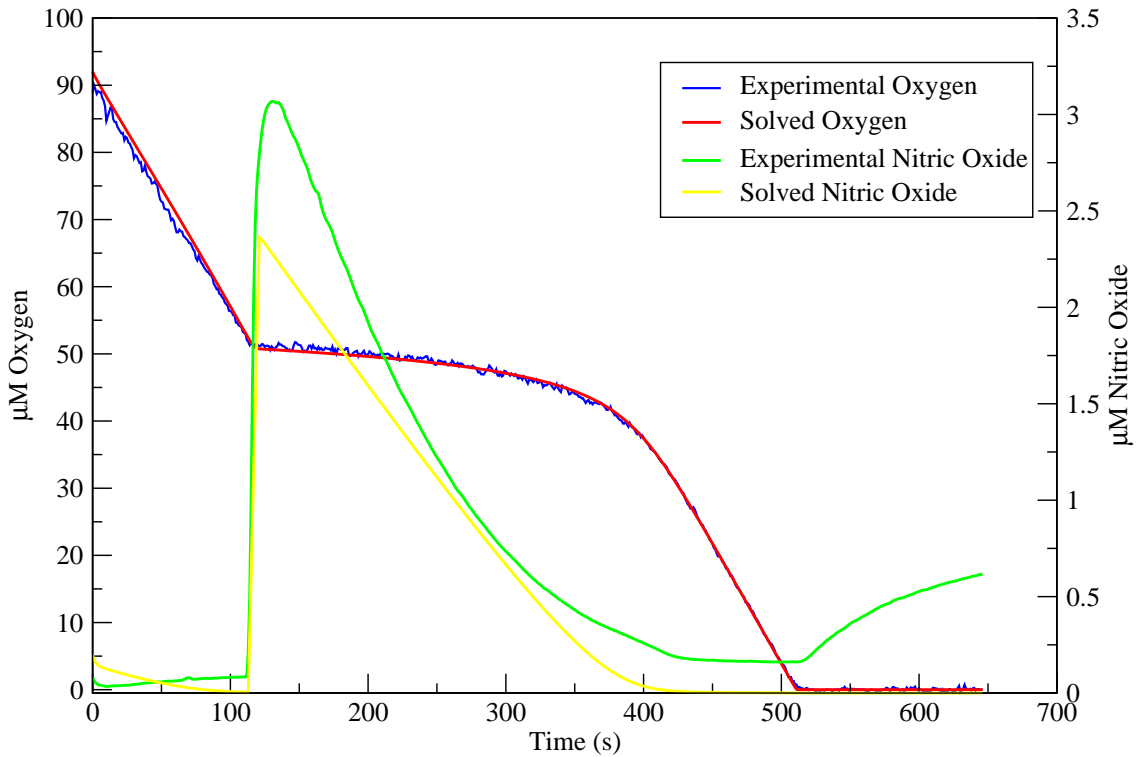


Figure 6.6: **Nitric Oxide Reduction in *Neisseria meningitidis*.** This dataset shows the effect on rate of oxygen reduction as nitric oxide is introduced to the system. The solved output, using prior probabilities from the oxygen reduction dataset show an almost perfect match to the features of the experimental dataset. The solved oxygen concentrations match the experimental dataset so closely as to be almost invisible.

6.1.2.3 Analysis of Convergence

6.1.2.4 Analysis of Correlation

6.1.3 Discussion

6.2 Microaerobic Nitric Oxide Reduction

6.2.1 Introduction

6.2.2 Results

6.2.3 Discussion

6.3 Aerobic Nitric Oxide Reduction in *nsrR*⁻ mutant

6.3.1 Introduction

The *nsrR*⁻ mutant, which expresses NorB in an essentially constitutive manner was not effective in generating a usable dataset as it removed any NO almost instantaneously resulting in an almost featureless dataset (data not shown).

6.3.2 Results

6.3.3 Discussion

Chapter 7

Nitrite Reduction in *N. meningitidis*

7.1 Microerobic Nitrite Reduction

7.1.1 Introduction

7.1.2 Results

7.1.3 Discussion

7.2 Microaerobic Nitrite Reduction in *norB*⁻ mutant

7.2.1 Introduction

7.2.2 Results

7.2.3 Discussion

7.3 Aerobic Nitrite Reduction in *nsrR*⁻ mutant

7.3.1 Introduction

Modelling nitrite reduction involves growing NsrR deficient cultures in aerobic conditions. This mutant expresses AniA and NorB in a constitutive manner, removing the necessity for growing the cultures in microaerobic conditions. The cultures are grown for 3-4 hours after which the culture is added to the electrode chamber and Sodium Nitrite added to a concentration of 1 mM.

In the model, Equations (3.3 & 3.8) are now also involved, allowing parametri-

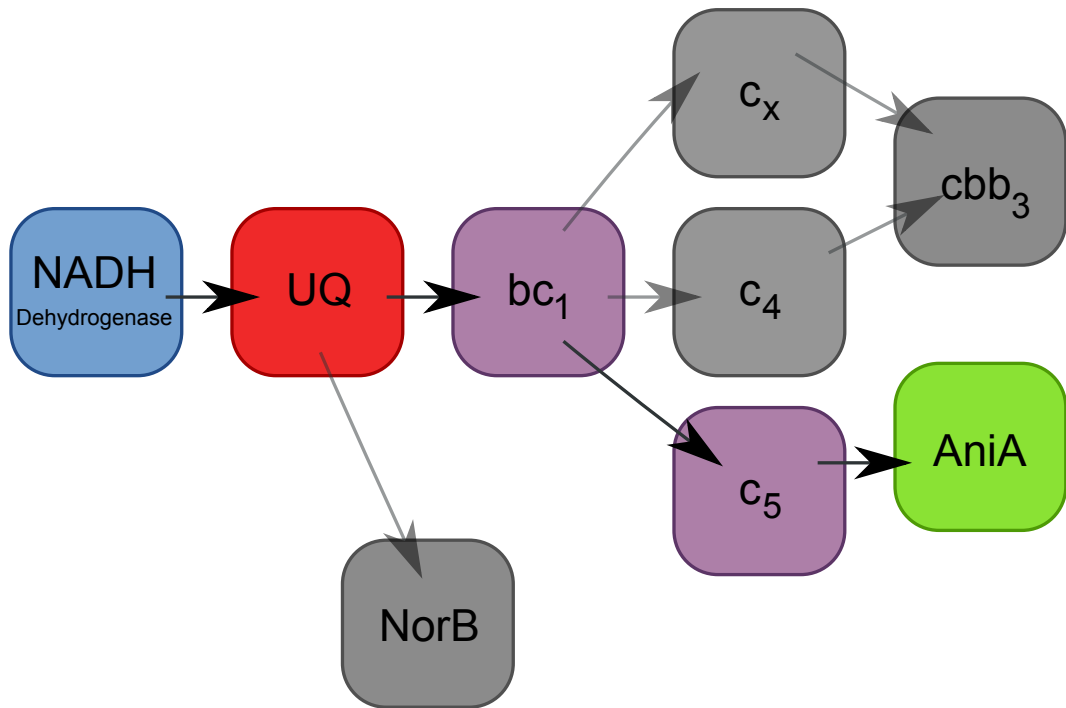


Figure 7.1: **Nitrite reducing electron transport chain of *N. meningitidis*.** This shows the complete electron transport chain of *Neisseria meningitidis* with the components irrelevant to nitrite reduction greyed out. In the mathematical model all of the purple elements (cytochromes) are amalgamated into one entity.

sation of kinetic rates of AniA. This experimental dataset does not unfortunately describe how the concentration of NO changes while Nitrite is being reduced. The prior probability distributions used for this dataset were the posteriors generated from the Nitric Oxide Reduction dataset described above, in accordance with Bayesian inference. The unknown parameters were given non-zero values with flat priors, allowed to burn-in and were then used to generate posterior probability distributions.

A representative dataset and solved output is shown in Figure 7.2.

This is a simpler dataset than for Nitric oxide reduction as it only describes nitrite reduction, along with a small change in oxygen concentration. In combination with prior probability distributions from the afore mentioned dataset it means that the possible values for the kinetic rates involved are automatically going to be limited to those that work alongside the given priors. Without the prior probability distributions the posterior distributions would have a similar outcome to that of the first dataset used, where simple oxygen reduction was

Nitrite Reduction in *Neisseria meningitidis*

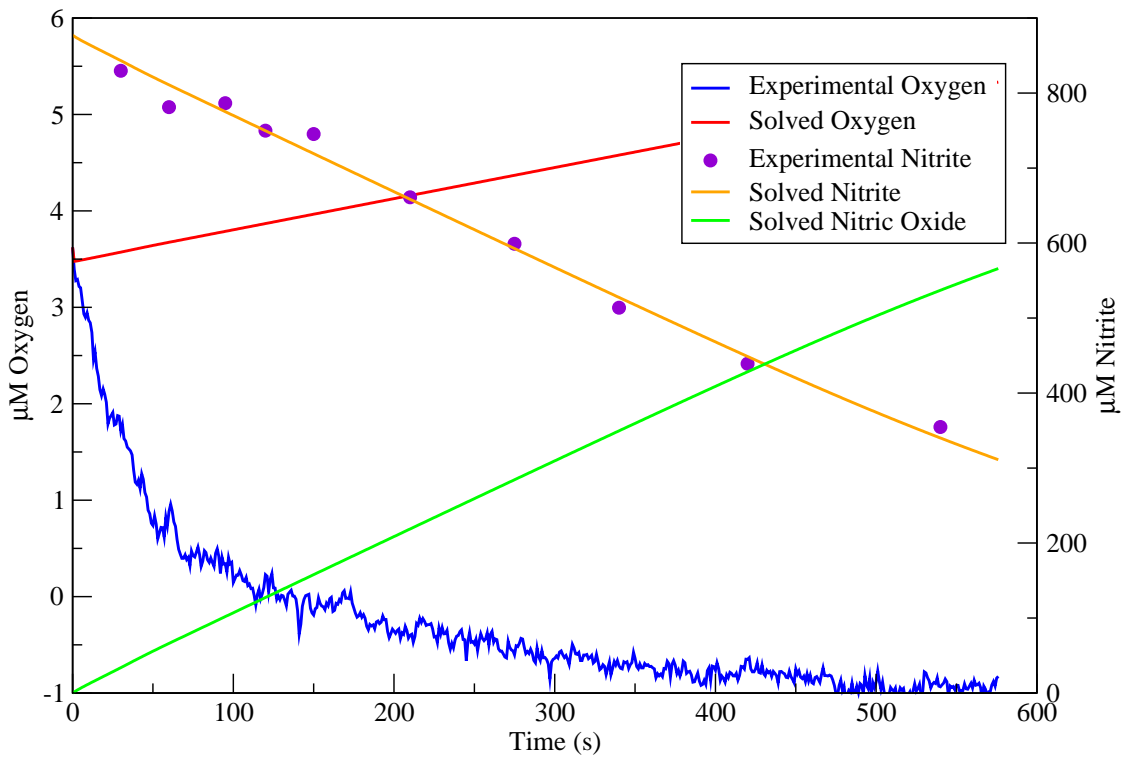


Figure 7.2: **Nitrite Reduction in *Neisseria meningitidis*.** This dataset shows the rate of nitrite reduction when cultures have been grown in microaerobic conditions. The concentrations of nitrite were measured off-line leading to discontinuous data, however the solved output closely matches the experimental data for nitrite.

modelled, i.e. very wide distributions.

7.3.2 Results

7.3.3 Discussion

7.4 Aerobic Nitrite Reduction in *nsrR*⁻-*norB*⁻ mutant

7.4.1 Introduction

7.4.2 Results

7.4.3 Discussion

Chapter 8

AniA and NorB Expression in *N. meningitidis*

8.1 Aerobic and Microaerobic Expression

8.1.1 Introduction

8.1.2 Results

8.1.3 Discussion

Chapter 9

The Completed Model

9.1 Amalgamation of cytochromes

Appendix A

Appendix

A.1 Adaptive step sizes and numerical instability

A.2 Affinity of cbb_3 for Oxygen

Unfortunately the degree of affinity could not be explored further as it was limited by the sampling rate of the oxygen electrode.

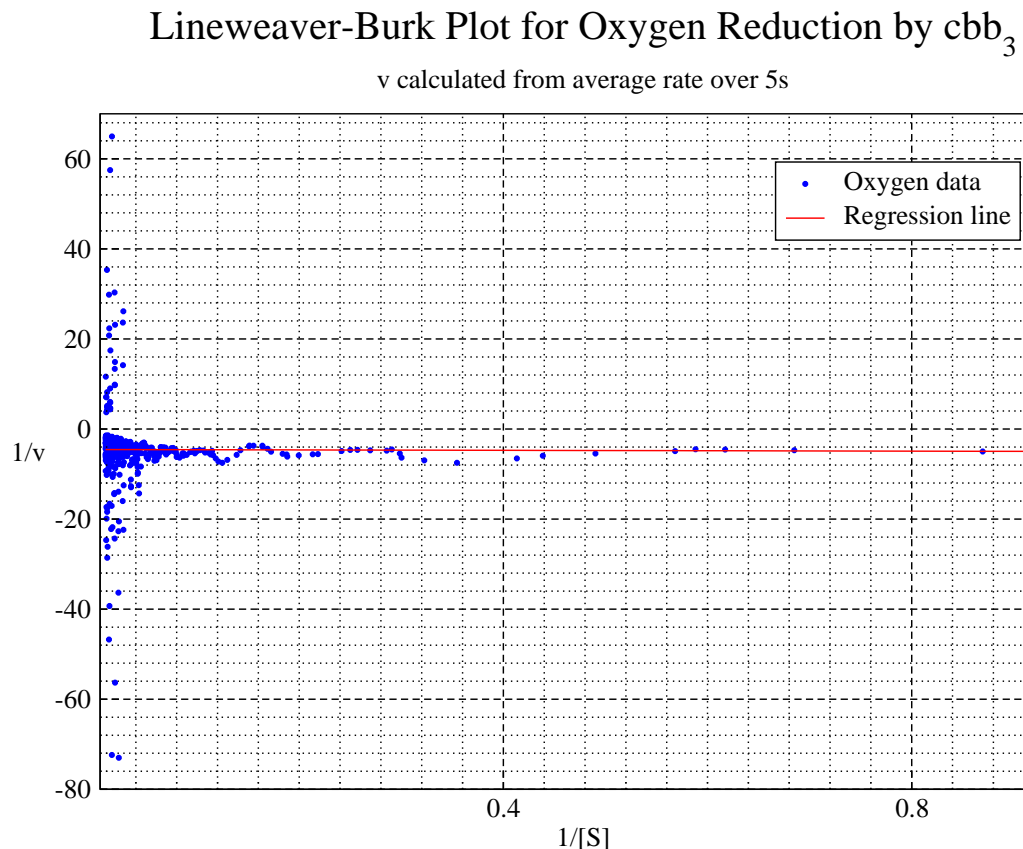


Figure A.1: Lineweaver-Burk Plot for Oxygen Reduction in *Neisseria meningitidis*.

$$\begin{aligned}
\frac{d[O_2]}{dt} &= \beta \left(1 - \frac{[O_2]}{K_O} \right) - k_1[C_a][O_2] \\
\frac{d[NO]}{dt} &= m_1[NO_2^-][A_a] - l_1[NO][B_a] - k_5[C_a][NO] + k_6[C_X] - \gamma[NO] \\
\frac{d[NO_2^-]}{dt} &= -m_1[NO_2^-][A_a] \\
\frac{d[Q_a]}{dt} &= g([Q] - [Q_a]) - l_3[Q_a]([B] - [B_a]) - f[Q_a]([X] - [X_a]) \\
\frac{d[X_a]}{dt} &= -k_3([C] - [C_a] - [C_X])[X_a] - m_3([A] - [A_a])[X_a] + f[Q_a]([X] - [X_a]) \\
\frac{d[A_a]}{dt} &= m_3([A] - [A_a])[X_a] - m_1[NO_2^-][A_a] \\
\frac{d[B_a]}{dt} &= l_3[Q_a]([B] - [B_a]) - l_1[NO][B_a] \\
\frac{d[C_a]}{dt} &= k_3([C] - [C_a] - [C_X])[X_a] - k_1[C_a][O_2] - k_5[C_a][NO] \\
\frac{d[C_X]}{dt} &= k_5[C_a][NO] - k_6[C_X] \\
\frac{d[A]}{dt} &= \left(R \left(1 - \frac{[O_2] + k_{10}[NO]}{[O_2] + k_{10}[NO] + k_{11}} \right) - S \left(1 - \frac{[NO]}{[NO] + k_{13}} \right) \right) - k_8[A] \\
\frac{d[B]}{dt} &= T \left(\frac{[NO]}{[NO] + k_{15}} \right) - k_{16}[B]
\end{aligned} \tag{A.1}$$

Symbol	Description
O_2	Oxygen concentration
NO	Nitric oxide concentration
NO_2^-	Nitrite concentration
X_a	Reduced cytochrome concentration
A_a	Reduced AniA
B_a	Reduced NorB
C_a	Reduced cbb_3
C_X	Reversibly inhibited cbb_3
Q_a	Reduced Quinones

Table A.1: Model Variables

Symbol	Description
k_1	Rate constant for O_2 reduction by reduced cbb_3
k_3	Rate constant for cbb_3 reduction by cytochrome pool
l_1	Rate constant for NO reduction by reduced NorB
l_3	Rate constant for NorB reduction by quinone pool
m_1	Rate constant for NO_2^- reduction by reduced AniA
m_3	Rate constant for AniA reduction by cytochrome pool
k_5	Rate constant for cbb_3 inhibition by NO
k_6	Rate constant for recovery of NO inhibited cbb_3
β	Rate constant for passive diffusion in of O_2
K_O	Saturation O_2 level
g	Rate of electrons in from NADH
f	Rate constant for reduction of cytochromes by quinones
γ	Spontaneous loss of NO
Q	Concentration of quinones
X	Concentration of cytochromes
A	Concentration of AniA
B	Concentration of NorB
C	Concentration of cbb_3

Table A.2: Model Parameters

List of Abbreviations

ABC	Approximate Bayesian computation
ABCSMC	Approximate Bayesian Computation by Sequential Monte Carlo
AniA	Anaerobically inducible protein A from <i>Neisseria</i> sp.
ATP	Adenosine triphosphate
BOF	Badness of Fit
CAB	Columbia Agar Base
CFU	Colony Forming Units
CSF	Cerebrospinal Fluid
DNA	Deoxyribonucleic Acid
ETC	Electron Transport Chain
FNR	Fumarate and Nitrite reduction Regulator
HCO	Haem Copper Oxidase
LSD	Least-Squares Difference
LSODA	Livermore Solver for Ordinary Differential Equations
MHB	Müller-Hinton Broth
MHMC	Metropolis-Hastings Monte Carlo
NADH	Nicotinamide adenine dinucleotide
NarP	Nitrate/Nitrite Response Regulator
NarQ	Nitrate/Nitrite Response Sensor
NED	N-1-naphthylethylenediamine dihydrochloride
NOR	Nitric Oxide Reductase
NorB	Nitric Oxide Reductase B from <i>Neisseria</i> sp.
NsrR	Nitrite sensing repressor protein
OD	Optical Density

ODE	Ordinary Differential Equation
PDE	Partial Differential Equation
rpm	Revolutions Per Minute
SMC	Sequential Monte Carlo
spc^r	Spectinomycin resistance
tet^r	tetracycline resistance

References

1. van Deuren M, Brandtzaeg P, van der Meer JWM (2000) Update on Meningococcal Disease with Emphasis on Pathogenesis and Clinical Management. *Clin Microbiol Rev* 13: 144–166.
2. Stephens DS (2009) Biology and Pathogenesis of the Evolutionarily Successful, Obligate Human Bacterium *Neisseria meningitidis*. *Vaccine* 27: B71–B77.
3. Rosenstein NE, Perkins BA, Stephens DS, Popovic T, Hughes JM (2001) Meningococcal Disease. *N Engl J Med* 344: 1378–1388.
4. DeVoe IW (1982) The Meningococcus and Mechanisms of Pathogenicity. *Microbiol Mol Biol Rev* 46: 162–190.
5. Aas JA, Paster BJ, Stokes LN, Olsen I, Dewhirst FE (2005) Defining the Normal Bacterial Flora of the Oral Cavity. *J Clin Microbiol* 43: 5721–5732.
6. Madigan M, Martinko J, editors (2005) Brock Biology of Microorganisms. 11th ed., Prentice Hall.
7. Carbonnelle E, Hill DJ, Morand P, Griffiths NJ, Bourdoulous S, et al. (2009) Meningococcal Interactions with the Host. *Vaccine* 27: B78–B89.
8. Stephens DS, Greenwood B, Brandtzaeg P (2007) Epidemic meningitis, meningococcaemia, and *Neisseria meningitidis*. *Lancet* 369: 2196–2210.

9. Larson JA, Higashi DL, Stojilkovic I, So M (2002) Replication of *Neisseria meningitidis* Within Epithelial Cells Requires TonB-Dependent Acquisition of Host Cell Iron. *Infect Immun* 70: 1461–1467.
10. Archibald FS, DeVoe IW (1978) Iron in *Neisseria meningitidis*: Minimum Requirements, Effects of Limitation, and Characteristics of Uptake. *J Bacteriol* 136: 35–48.
11. Perkins-Balding D, Ratliff-Griffin M, Stojilkovic I (2004) Iron Transport Systems in *Neisseria meningitidis*. *Microbiol Mol Biol Rev* 68: 154–171.
12. Yazdankhah SP, Caugant DA (2004) *Neisseria meningitidis*: An Overview of the Carriage State. *J Med Microbiol* 53: 821–832.
13. Beddek AJ, Li MS, Kroll JS, Jordan TW, Martin DR (2009) Evidence for Capsule Switching between Carried and Disease-Causing *Neisseria meningitidis* Strains. *Infect Immun* 77: 2989–2994.
14. Moxon ER, Rainey PB, Nowak MA, Lenski RE (1994) Adaptive Evolution of Highly Mutable Loci in Pathogenic Bacteria. *Current Biology* 4: 24–33.
15. Pathan N, Faust SN, Levin M (2003) Pathophysiology of Meningococcal Meningitis and Septicaemia. *Arch Dis Child* 88: 601–607.
16. Exley RM, Shaw J, Mowe E, Sun YH, West NP, et al. (2005) Available Carbon Source Influences the Resistance of *Neisseria meningitidis* Against Complement. *J Exp Med* 201: 1637–1645.
17. Beno DW, Devine LF, Larson GL (1968) Identification of *Neisseria meningitidis* Carbohydrate Fermentation Patterns in Mueller-Hinton Broth. *J Bacteriol* 96: 563.
18. Rock JD, Mahnane MR, Anjum MF, Shaw JG, Read RC, et al. (2005) The Pathogen *Neisseria meningitidis* Requires Oxygen, but Supplements

- Growth by Denitrification. Nitrite, Nitric Oxide and Oxygen Control Respiratory Flux at Genetic and Metabolic Levels. *Mol Microbiol* 58: 800–9.
19. Rock JD, Moir JWB (2005) Microaerobic Denitrification in *Neisseria meningitidis*. *Biochem Soc Trans* 33: 134–6.
 20. Tuttle DM, Scherp HW (1952) Studies On The Carbon Dioxide Requirement Of *Neisseria meningitidis*. *J Bacteriol* 64: 171–182.
 21. Lundberg JO, Weitzberg E, Cole JA, Benjamin N (2004) Nitrate, Bacteria and Human Health. *Nat Rev Micro* 2: 593–602.
 22. Deeudom M, Rock J, Moir J (2006) Organization of the Respiratory Chain of *Neisseria meningitidis*. *Biochem Soc Trans* 34: 139–42.
 23. Deeudom M (2007) The Electron Transport Chains of *Neisseria meningitidis*. Ph.D. thesis, University of York.
 24. Preisig O, Zufferey R, Thony-Meyer L, Appleby C, Hennecke H (1996) A High-affinity cbb3-Type Cytochrome Oxidase Terminates the Symbiosis-Specific Respiratory Chain of *Bradyrhizobium japonicum*. *J Bacteriol* 178: 1532–1538.
 25. Brown GC, Cooper C (1994) Nanomolar Concentrations of Nitric Oxide Reversibly Inhibit Synaptosomal Respiration by Competing with Oxygen at Cytochrome Oxidase. *FEBS Letters* 356: 295–298.
 26. Sharpe MA, Cooper CE (1998) Interaction of Peroxynitrite with Mitochondrial Cytochrome Oxidase. *J Biol Chem* 273: 30961–30972.
 27. Anjum MF, Stevanin TM, Read RC, Moir JWB (2002) Nitric Oxide Metabolism in *Neisseria meningitidis*. *J Bacteriol* 184: 2987–2993.
 28. Heurlier K, Thomson MJ, Aziz N, Moir JWB (2008) The Nitric Oxide (NO)-Sensing Repressor NsrR of *Neisseria meningitidis* has a Compact Regulon

- of Genes Involved in NO Synthesis and Detoxification. *J Bacteriol* 190: 2488–95.
29. Deedom M, Koomey M, Moir JWB (2008) Roles of C-type Cytochromes in Respiration in *Neisseria meningitidis*. *Microbiology* 154: 2857–64.
30. Rock JD, Thomson MJ, Read RC, Moir JWB (2007) Regulation of Denitrification Genes in *Neisseria meningitidis* by Nitric Oxide and the Repressor NsrR. *J Bacteriol* 189: 1138–44.
31. Isabella V, Wright LF, Barth K, Spence JM, Grogan S, et al. (2008) Cis- and Trans-Acting Elements Involved in Regulation if NorB (NorZ), The Gene Encoding Nitric Oxide Reductase in *Neisseria gonorrhoeae*. *Microbiology* 154: 226–239.
32. Pitcher RS, Watmough NJ (2004) The Bacterial Cytochrome cbb3 Oxidases. *Biochimica et Biophysica Acta (BBA) - Bioenergetics* 1655: 388 – 399.
33. Puustinen A, Verkhovsky MI, Morgan JE, Belevich NP, Wikstrom M (1996) Reaction of the *Escherichia coli* Quinol Oxidase Cytochrome bo3 with Dioxygen: The Role of a Bound Ubiquinone Molecule. *Proc Natl Acad Sci U S A* 93: 1545–1548.
34. van der Oost J, de Boer AP, de Gier JW, Zumft WG, Stouthamer AH, et al. (1994) The Heme-Copper Oxidase Family Consists of Three Distinct Types of Terminal Oxidases and is Related to Nitric Oxide Reductase. *FEMS Microbiol Lett* 121: 1–9.
35. García-Horsman JA, Barquera B, Rumbley J, Ma J, Gennis RB (1994) The Superfamily of Heme-Copper Respiratory Oxidases. *J Bacteriol* 176: 5587–5600.
36. Keilin D, Hartree EF (1939) Cytochrome and Cytochrome Oxidase. *Proceedings of the Royal Society of London Series B, Biological Sciences* 127: pp. 167–191.

37. Huang Y, Reimann J, Singh LMR, Adelroth P (2010) Substrate Binding and the Catalytic Reactions in Cbb3-type Oxidases: The Lipid Membrane Modulates Ligand Binding. *Biochim Biophys Acta* 1797: 724–731.
38. Buschmann S, Warkentin E, Xie H, Langer JD, Ermler U, et al. (2010) The structure of cbb3 cytochrome oxidase provides insights into proton pumping. *Science* 329: 327–330.
39. Zufferey R, Preisig O, Hennecke H, ThĂűny-Meyer L (1996) Assembly and Function of the Cytochrome cbb3 Oxidase Subunits in *Bradyrhizobium japonicum*. *J Biol Chem* 271: 9114–9119.
40. Preisig O, Zufferey R, Hennecke H (1996) The *Bradyrhizobium japonicum* fixGHIS Genes are Required for the Formation of the High-Affinity cbb3-type Cytochrome Oxidase. *Arch Microbiol* 165: 297–305.
41. Householder TC, Fozo EM, Cardinale JA, Clark VL (2000) Gonococcal Nitric Oxide Reductase is Encoded by a Single Gene, NorB, Which is Required for Anaerobic Growth and is Induced by Nitric Oxide. *Infect Immun* 68: 5241–5246.
42. Barth KR, Isabella VM, Clark VL (2009) Biochemical and Genomic Analysis of the Denitrification Pathway within the Genus *Neisseria*. *Microbiology* 155: 4093–4103.
43. Clark VL, Campbell LA, Palermo DA, Evans TM, Klimpel KW (1987) Induction and Repression of Outer Membrane Proteins by Anaerobic Growth of *Neisseria gonorrhoeae*. *Infect Immun* 55: 1359–1364.
44. Moir JW (2011) A Snapshot of a Pathogenic Bacterium Mid-evolution: *Neisseria meningitidis* is Becoming a Nitric Oxide-Tolerant Aerobe. *Biochem Soc Trans* 39: 1890–1894.

45. Weiss H, Friedrich T, Hofhaus G, Preis D (1991) The Respiratory-Chain NADH Dehydrogenase (Complex I) of Mitochondria. *Eur J Biochem* 197: 563–576.
46. Carroll J, Fearnley IM, Shannon RJ, Hirst J, Walker JE (2003) Analysis of the Subunit Composition of Complex I from Bovine Heart Mitochondria. *Mol Cell Proteomics* 2: 117–126.
47. Friedrich T, Böttcher B (2004) The Gross Structure of the Respiratory Complex I: a Lego System. *Biochim Biophys Acta* 1608: 1–9.
48. Yagi T (1991) Bacterial NADH-Quinone Oxidoreductases. *J Bioenerg Biomembr* 23: 211–225.
49. Gemperli AC, Dimroth P, Steuber J (2002) The Respiratory Complex I (NDH I) from *Klebsiella pneumoniae*, a Sodium Pump. *J Biol Chem* 277: 33811–33817.
50. Thöny-Meyer L (1997) Biogenesis of Respiratory Cytochromes in Bacteria. *Microbiology and Molecular Biology Reviews* 61: 337–76.
51. Darrouzet E, Valkova-Valchanova M, Ohnishi T, Daldal F (1999) Structure and Function of the Bacterial bc1 Complex: Domain Movement, Subunit Interactions, and Emerging Rationale Engineering Attempts. *J Bioenerg Biomembr* 31: 275–288.
52. Snyder CH, Gutierrez-Cirlos EB, Trumper BL (2000) Evidence for a Concerted Mechanism of Ubiquinol Oxidation by the Cytochrome bc 1 Complex. *Journal of Biological Chemistry* 275: 13535–13541.
53. Berry EA, Huang LS (2011) Conformationally Linked Interaction in the Cytochrome bc(1) Complex Between Inhibitors of the Q(o) Site and the Rieske Iron-Sulfur Protein. *Biochim Biophys Acta* 1807: 1349–1363.

54. Crofts AR, Shinkarev VP, Kolling DRJ, Hong S (2003) The Modified Q-Cycle Explains the Apparent Mismatch Between the Kinetics of Reduction of Cytochromes c1 and bh in the bc1 Complex. *J Biol Chem* 278: 36191–36201.
55. Wood PM (1983) Why do c-type Cytochromes Exist? *FEBS Lett* 164: 223–226.
56. Ambler RP (1991) Sequence Variability in Bacterial Cytochromes c. *Biochim Biophys Acta* 1058: 42–47.
57. Chang HY, Ahn Y, Pace LA, Lin MT, Lin YH, et al. (2010) The Diheme Cytochrome C(4) from *Vibrio cholerae* is a Natural Electron Donor to the Respiratory cbb(3) Oxygen Reductase. *Biochemistry* 49: 7494–7503.
58. Clark VI, Isabella VM, Barth K, Overton TW (2010) Regulation and Function of the Neisserial Denitrification Pathway: Life with Limited Oxygen. In: Genco CA, Wetzler L, editors, *Neisseria: Molecular Mechanisms of Pathogenesis*, chap. 2, pp. 19–39, Caister Academic Press.
59. Edwards J, Cole LJ, Green JB, Thomson MJ, Wood AJ, et al. (2010) Binding to DNA Protects *Neisseria meningitidis* Fumarate and Nitrate Reductase Regulator (FNR) from Oxygen. *Journal of Biological Chemistry* 285: 1105–1112.
60. Overton TW, Whitehead R, Li Y, Snyder LAS, Saunders NJ, et al. (2006) Coordinated Regulation of the *Neisseria gonorrhoeae*-Truncated Denitrification Pathway by the Nitric Oxide-Sensitive Repressor, NsrR, and Nitrite-Insensitive NarQ-NarP. *J Biol Chem* 281: 33115–33126.
61. Baker SC, Ferguson SJ, Ludwig B, Page MD, Richter OM, et al. (1998) Molecular Genetics of the Genus Paracoccus: Metabolically Versatile Bacteria with Bioenergetic Flexibility. *Microbiol Mol Biol Rev* 62: 1046–1078.

62. Nicholls DG, Ferguson SJ (1992) Bioenergetics 3. 2nd ed., Academic Press.
63. Kahlem P, Birney E (2006) Dry Work in a Wet World: Computation in Systems Biology. *Mol Syst Biol* 2: 40.
64. Doyle FJr, Stelling J (2006) Systems Interface Biology. *J R Soc Interface* 3: 603–16.
65. Kitano H (2002) Computational Systems Biology. *Nature* 420: 206–10.
66. Kitano H (2002) Systems Biology: A Brief Overview. *Science* 295: 1662–4.
67. Valencia A, Pazos F (2002) Computational Methods for the Prediction of Protein Interactions. *Curr Opin Struct Biol* 12: 368–73.
68. Mündermann L, Erasmus Y, Lane B, Coen E, Prusinkiewicz P (2005) Quantitative Modeling of Arabidopsis Development. *Plant Physiol* 139: 960–8.
69. Prusinkiewicz P (2004) Modeling Plant Growth And Development. *Curr Opin Plant Biol* 7: 79–83.
70. Prusinkiewicz P, Rolland-Lagan AG (2006) Modeling Plant Morphogenesis. *Curr Opin Plant Biol* 9: 83–8.
71. Crampin EJ, Halstead M, Hunter P, Nielsen P, Noble D, et al. (2004) Computational Physiology and the Physiome Project. *Exp Physiol* 89: 1–26.
72. Barabási AL, Oltvai ZN (2004) Network Biology: Understanding the Cell's Functional Organization. *Nat Rev Genet* 5: 101–13.
73. Peercy BE, Cox SJ, Shalel-Levanon S, San KY, Bennett G (2006) A Kinetic Model of Oxygen Regulation of Cytochrome Production in *Escherichia coli*. *J Theor Biol* 242: 547–563.
74. Almeida JS, Reis MAM, Carrondo MJT (1997) A Unifying Kinetic Model of Denitrification. *Journal of Theoretical Biology* 186: 241–249.

75. Cavaliere M, Ardelean II (2006) Applications of Membrane Computing, chap. Modeling Respiration in Bacteria and Respiration/Photosynthesis Interaction in Cyanobacteria Using a P System Simulator, pp. 129–158. Springer.
76. Klipp E, Herwig R, Kowald A, Wierling C, Lehrach H (2005) Systems Biology in Practice. Concepts, Implementation and Application. WILEY-VCH Verlag GmbH & Co. KGaA, Weinheim.
77. Gillespie DT (1977) Exact Stochastic Simulation of Coupled Chemical Reactions. *The Journal of Physical Chemistry* 81: 2340–2361.
78. Sauro HM, Hucka M, Finney A, Wellock C, Bolouri H, et al. (2003) Next Generation Simulation Tools: The Systems Biology Workbench and BioSPICE Integration. *OMICS: A Journal of Integrative Biology* 7: 355–372.
79. Hoops S, Sahle S, Gauges R, Lee C, Pahle J, et al. (2006) COPASI—a COmplex PAthway SImlator. *Bioinformatics* 22: 3067–3074.
80. Radhakrishnan K, Hindmarsh AC (1993) Description and Use of LSODE, the Livermore Solver for Ordinary Differential Equations. Tech. rep., NASA.
81. Gibson MA, Bruck J (2000) Efficient Exact Stochastic Simulation of Chemical Systems with Many Species and Many Channels. *The Journal of Physical Chemistry A* 104: 1876–1889.
82. McGuinness B, Barlow AK, Clarke IN, Farley JE, Anilionis A, et al. (1990) Deduced Amino Acid Sequences of Class 1 Protein (Pora) from Three Strains of *Neisseria meningitidis*. Synthetic Peptides Define the Epitopes Responsible for Serosubtype Specificity. *J Exp Med* 171: 1871–1882.

83. Clark LC, Wolf R, Granger D, Taylor Z (1953) Continuous Recording of Blood Oxygen Tensions by Polarography. *Journal of Applied Physiology* 6: 189–193.
84. Rank Brothers Ltd (2012) Oxygen Electrode Exploded Views. <http://www.rankbrothers.co.uk/prod1exp.htm>.
85. YSI Incorporated (2012) Oxygen Solubility Table. <http://www.ysi.com/media/pdfs/DO-Oxygen-Solubility-Table.pdf>.
86. Liu X, Liu Q, Gupta E, Zorko N, Brownlee E, et al. (2005) Quantitative Measurements of No Reaction Kinetics with a Clark-Type Electrode. *Nitric Oxide* 13: 68 – 77.
87. Bedioui F, Villeneuve N (2003) Electrochemical Nitric Oxide Sensors for Biological Samples: Principle, Selected Examples and Applications. *Electroanalysis* 15: 5–18.
88. Serpe MJ, Zhang X (2007) The Principles, Development and Application of Microelectrodes for the In Vivo Determination of Nitric Oxide. In: Michael AC, Borland LM, editors, *Electrochemical Methods for Neuroscience*, chap. 21, CRC Press.
89. Nicholas DJ, Nason A (1957) Determination of Nitrate and Nitrite. In: *Methods in Enzymology*, vol. 3, pp. 981–984, Academic Press.
90. Aga RG, Hughes MN (2008) The Preparation and Purification of NO Gas and the Use of NO Releasers: The Application of NO Donors and Other Agents of Nitrosative Stress in Biological Systems. In: Poole RK, editor, *Globins and Other Nitric Oxide-Reactive Proteins, Part A*, vol. 436 of *Methods in Enzymology*, pp. 35 – 48, Academic Press.
91. Cole LJ, Huston WM, Moir JWB (2008) Delivery of Nitric Oxide for Analysis of the Function of Cytochrome C'. In: Poole RK, editor, *Globins and*

- Other Nitric Oxide-Reactive Proteins, Part A, vol. 436 of Methods in Enzymology, pp. 21 – 33, Academic Press.
92. Giuffre A, Barone MC, Mastronicola D, D'Itri E, Sarti P, et al. (2000) Reaction of Nitric Oxide with the Turnover Intermediates of Cytochrome c Oxidase: Reaction Pathway and Functional Effects. *Biochemistry* 39: 15446–15453.
 93. Forte E, Urbani A, Saraste M, Sarti P, Brunori M, et al. (2001) The Cytochrome *cbb3* from *Pseudomonas stutzeri* Displays Nitric Oxide Reductase Activity. *Eur J Biochem* 268: 6486–6491.
 94. Hunter H (2007) Characterisation of the Oxidase Activity in *Neisseria lactamica*, University of York BSc Honours Project Report.
 95. Nojiri M, Koteishi H, Nakagami T, Kobayashi K, Inoue T, et al. (2009) Structural Basis of Inter-Protein Electron Transfer for Nitrite Reduction in Denitrification. *Nature* 462: 117–120.
 96. Blackmore RS, Greenwood C, Gibson QH (1991) Studies of the Primary Oxygen Intermediate in the Reaction of Fully Reduced Cytochrome Oxidase. *Journal of Biological Chemistry* 266: 19245–9.
 97. Hedrick DB, White DC (1986) Microbial Respiratory Quinones in the Environment: I. A Sensitive Liquid Chromatographic Method. *Journal of Microbiological Methods* 5: 243 – 254.
 98. Butcher JC (2003) Numerical Methods for Ordinary Differential Equations. John Wiley and Sons.
 99. Cash JR, Karp AH (1990) A Variable Order Runge-Kutta Method for Initial Value Problems with Rapidly Varying Right-hand Sides. *ACM Trans Math Softw* 16: 201–222.

100. Press WH, Teukolsky SA, Vetterling WT, Flannery BP (1992) Numerical Recipes in C. 2nd ed., Cambridge University Press.
101. Nakamura (Particle Data Group) K (2010) Review of Particle Physics. *Journal of Physics G: Nuclear and Particle Physics* 37: 075021 and 2011 partial update for the 2012 edition.
102. Kirkpatrick S, Gelatt CD, Vecchi MP (1983) Optimization by Simulated Annealing. *Science* 220: pp. 671–680.
103. Černý V (1985) Thermodynamical Approach to the Traveling Salesman Problem: An Efficient Simulation Algorithm. *Journal of Optimization Theory and Applications* 45: 41–51.
104. Bertsimas D, Tsitsiklis J (1993) Simulated Annealing. *Statistical Science* 8: pp. 10–15.
105. Toni T, Welch D, Strelkowa N, Ipsen A, Stumpf MPH (2009) Approximate Bayesian Computation Scheme for Parameter Inference and Model Selection in Dynamical Systems. *Journal of The Royal Society Interface* 6: 187.
106. Ronquist F, Teslenko M, van der Mark P, Ayres D, Darling A, et al. (2011) MrBayes 3.2: Efficient Bayesian Phylogenetic Inference and Model Choice Across a Large Model Space. *Systematic Biology* in press: 0–0.
107. Beaumont MA, Zhang W, Balding DJ (2002) Approximate Bayesian computation in population genetics. *Genetics* 162: 2025–2035.
108. Sisson SA, Fan Y, Tanaka MM (2007) Sequential Monte Carlo without likelihoods. *Proc Natl Acad Sci U S A* 104: 1760–1765.
109. Beaumont MA (2010) Approximate Bayesian Computation in Evolution and Ecology. *Annual Review of Ecology, Evolution, and Systematics* 41: pp. 379–406.

110. Metropolis N, Rosenbluth AW, Rosenbluth MN, Teller AH, Teller E (1953) Equation of State Calculations by Fast Computing Machines. *The Journal of Chemical Physics* 21: 1087–1092.
111. Hastings WK (1970) Monte Carlo Sampling Methods Using Markov Chains and Their Applications. *Biometrika* 57: 97–109.
112. Gelman A, Rubin DB (1992) Inference from Iterative Simulation Using Multiple Sequences. *Statistical Science* 7: pp. 457–472.
113. Brooks SP, Gelman A (1998) General Methods for Monitoring Convergence of Iterative Simulations. *Journal of Computational and Graphical Statistics* 7: 434–455.
114. Curran J (2011) Bolstad2: Bolstad functions.
115. R Development Core Team (2010) R: A Language and Environment for Statistical Computing. R Foundation for Statistical Computing, Vienna, Austria.